

**OPTICALLY CONTROLLING DARK STATE LIFETIMES OF  
PHOTOSWITCHABLE FLUORESCENT PROTEINS AND ITS  
APPLICATION TO BIOLOGICAL SYSTEMS**

A Thesis  
Presented to  
The Academic Faculty

by

Yen-Cheng Chen

In Partial Fulfillment  
of the Requirements for the Degree  
Doctor of Philosophy in the  
School of Chemistry and Biochemistry

Georgia Institute of Technology  
May 2018

**Copyright © Yen-Cheng Chen 2018**

**OPTICALLY CONTROLLING DARK STATE LIFETIMES OF  
PHOTOSWITCHABLE FLUORESCENT PROTEINS AND ITS  
APPLICATION TO BIOLOGICAL SYSTEMS**

Approved by:

Dr. Robert M. Dickson, Advisor  
School of Chemistry and Biochemistry  
Georgia Institute of Technology

Dr. Joseph W. Perry  
School of Chemistry and Biochemistry  
Georgia Institute of Technology

Dr. Christoph Fahrni  
School of Chemistry and Biochemistry  
Georgia Institute of Technology

Dr. Cheng Zhu  
School of Biomedical Engineering  
Georgia Institute of Technology

Dr. Harold Kim  
School of Physics  
Georgia Institute of Technology

Date Approved: November 27, 2017

## ACKNOWLEDGEMENTS

I would like to thank all the support and encouragement from people around me. First, Dr. Robert Dickson, as an advisor and a mentor, teaches me not only the scientific logic and critical thinking on multiple projects but also allows me to spend time on finding my next step after graduation, including internship. I really enjoy working with Rob by getting honest opinions when it comes to projects and presentations as well as having great amount of freedom to fail or explore science and personal career goal. In addition to my advisor, my group members help me a lot. Especially past member Amy Jablonski and Jung-Cheng Hsiang taught me fluorescence techniques and simulations for the projects. All the helps from Tzu-Hsueh, Dan, Aida, Joe, Baijie, Yi-Han, and Alex assist me during the entire research, especially Tzu-Hsueh helped me a lot when I first started school. This lab is really encouraging and willing to help each other.

In addition to my lab, I would like to thank all the critical input from my collaborators. Daisy and Irina from Fahrni Lab provides the purified fluorescent proteins and NIH-3T3 cells with targeted fluorescent proteins for me to measure the photophysical dark states and perform imaging experiments. Chetan from Melikyan Lab provides me the virus-like-particles with rsFastLime for performing SAFIRE experiments on commercial microscopes. Also, Chenghao from Zhu Lab provides lipid bilayers, pMHC, and T cells for studying weak protein-protein interactions. I get the cells/virus/proteins from the collaborators as well as valuable discussions about design of experiment to improve fluorescence methods, especially discussion with Chenghao really assisting me for experimental design or job search in general. All the supports from my friends and

family have been driving me forward and helping me motivated. Elias, Yi, Amy, Robert, Hao-Lin, Otis, Jui-Yun, Helen, Tzu-Hsueh, and so many others constantly listen to me and are bothered by my questions or complaints. My family always trusts me and helps me no matter what. I cannot finish this thesis without ALL OF YOU. THANK YOU!

# TABLE OF CONTENTS

<b>ACKNOWLEDGEMENTS .....</b>	<b>III</b>
<b>LIST OF TABLES .....</b>	<b>IX</b>
<b>LIST OF FIGURES .....</b>	<b>X</b>
<b>LIST OF SYMBOLS AND ABBREVIATIONS .....</b>	<b>XVII</b>
<b>SUMMARY .....</b>	<b>XXI</b>
<b>CHAPTER 1 INTRODUCTION.....</b>	<b>- 1 -</b>
<b>1.1 Motivation .....</b>	<b>- 1 -</b>
<b>1.2 Introduction of Fluorescence .....</b>	<b>- 3 -</b>
1.2.1 History of Fluorescence .....	- 3 -
1.2.2 Jablonski Diagram .....	- 3 -
1.2.2.1 Reversible Dark States .....	- 5 -
1.2.2 Fluorescence Microscopy .....	- 5 -
1.2.3 Common Fluorescence Microscopes.....	- 6 -
1.2.3.1 Wide-Field & Confocal Microscopy .....	- 7 -
1.2.3.2 Spinning Disk Confocal Microscopy (SDCM).....	- 7 -
1.2.3.3 Total Internal Reflection Fluorescence Microscopy (TIRFM) .....	- 8 -
1.2.3.4 Super Resolution Microscopy (SRM) .....	- 9 -
<b>1.3 Choice of Fluorescent Dyes .....</b>	<b>- 10 -</b>
1.3.1 Intrinsic or Natural Fluorophores .....	- 10 -
1.3.2 Extrinsic Fluorophores .....	- 11 -
1.3.3 Fluorescent Proteins .....	- 11 -
<b>1.4 Fluorescent Proteins .....</b>	<b>- 12 -</b>
1.4.1 Introduction of Fluorescent Proteins.....	- 13 -
1.4.2 Photoswitchable Fluorescent Proteins (PS-FPs) .....	- 14 -
1.4.3 Protein Structure .....	- 16 -
1.4.4 Protein Photophysics .....	- 16 -
1.4.4.1 Excited-state proton transfer.....	- 16 -
1.4.4.2 Cis-trans isomerization .....	- 17 -
1.4.4.3 Dark states of FPs.....	- 19 -
1.4.5 Applications.....	- 21 -

<b>1.5 Fluorescence Techniques for Protein Dynamics .....</b>	<b>- 22 -</b>
1.5.1 Fluorescence Recovery after Photobleaching (FRAP).....	- 22 -
1.5.2 Fluorescence Correlation and Cross-Correlation Spectroscopy (FCS, FCCS) ...	- 23 -
1.5.3 Förster Resonance Energy Transfer (FRET) and Fluorescence Lifetime Imaging Microscopy (FLIM) .....	- 25 -
<b>1.6 Limitations of Current Fluorescence Techniques.....</b>	<b>- 27 -</b>
1.6.1 Autofluorescent Background .....	- 27 -
1.6.2 Detection of Weak Protein-Protein Interactions (PPIs).....	- 28 -
<b>1.7 Optical Modulation.....</b>	<b>- 30 -</b>
 <b>CHAPTER 2   EXPERIMENTAL METHODS .....</b>	<b>- 34 -</b>
 <b>2.1 Sample Preparation .....</b>	<b>- 34 -</b>
2.1.1 Organic Dyes .....	- 34 -
2.1.2 Fluorescent Proteins & Biological Samples.....	- 34 -
<b>2.2 Fluorescence Microscopy: Single-Point Detection.....</b>	<b>- 35 -</b>
2.2.1 Light Source.....	- 36 -
2.2.2 Optics .....	- 37 -
2.2.3 Microscopes & Objectives .....	- 37 -
2.2.4 Detectors & Photon Counting Boards .....	- 38 -
<b>2.3 Fluorescence Microscopy: Wide-Field Detection.....</b>	<b>- 39 -</b>
2.3.1 EMCCD .....	- 39 -
<b>2.4 Optical Alignments for Each Microscope .....</b>	<b>- 40 -</b>
2.4.1 Single-Modulation & Dual-Modulation SAFiRe (SM- & DM-SAFiRe).....	- 40 -
2.4.1.1 Measurement of Dark State Lifetimes.....	- 40 -
2.4.2 Epi-Fluorescence Microscope .....	- 41 -
2.4.3 Spinning-Disk Confocal Microscope.....	- 42 -
2.4.4 Total Internal Reflection Fluorescence Microscope (TIRFM) .....	- 43 -
2.4.5 Live Cell Imaging .....	- 44 -
2.4.6 Fluorescence Correlation Spectroscopy & Fluorescence Cross-Correlation Spectroscopy (FCS, FCCS).....	- 45 -
2.4.7 Image-Based Fluorescence Correlation Spectroscopy & Fluorescence Cross-Correlation Spectroscopy.....	- 47 -
2.4.8 OPIOM-SAFiRe .....	- 50 -
<b>2.5 Commercial Microscopes .....</b>	<b>- 51 -</b>
 <b>CHAPTER 3   AUTOFLUORESCENCE SUPPRESSION AND SELECTIVE IMAGING .....</b>	<b>- 52 -</b>

<b>3.1 Introduction .....</b>	<b>- 52 -</b>
3.1.1 Optical Lock-in Detection (OLID).....	- 53 -
<b>3.2 Autofluorescence Suppression .....</b>	<b>- 54 -</b>
3.2.1 Single-Modulation SAFIRE (SM-SAFIRE).....	- 54 -
3.2.2 Dual-Modulation SAFIRE (DM-SAFIRE) .....	- 55 -
<b>3.3 Selective Imaging.....</b>	<b>- 62 -</b>
3.3.1 Characterizing the Dark State Lifetime of rsFastLime .....	- 63 -
3.3.2 Diffusing vs. Immobilized rsFastLime.....	- 64 -
3.3.3 Spectral Unmixing .....	- 67 -
<b>3.4 Conclusion .....</b>	<b>- 69 -</b>
<b>Supporting Information: Photophysical Response of FPs and PS-FPs with SM-SAFIRE and DM-SAFIRE .....</b>	<b>- 70 -</b>
<b>CHAPTER 4 SAFIRE ON COMMERCIAL MICROSCOPES.....</b>	<b>- 75 -</b>
<b>4.1 Introduction .....</b>	<b>- 76 -</b>
<b>4.2 SAFIRE on Currently Available Commercial Microscopes .....</b>	<b>- 79 -</b>
4.2.1 Demonstration of SAFIRE with Modulatable FPs on Commercial Microscopes - 79	-
4.2.2 Demonstration of SAFIRE with PS-FPs on Commercial Microscopes .....	- 81 -
<b>4.3 Visualization of Virus Particles on Commercial Microscopes .....</b>	<b>- 83 -</b>
<b>4.4 Conclusion .....</b>	<b>- 87 -</b>
<b>CHAPTER 5 OPIOM-SAFIRE.....</b>	<b>- 89 -</b>
<b>5.1 Introduction .....</b>	<b>- 89 -</b>
<b>5.2 Improved OPIOM by Optically Controllable Dark States .....</b>	<b>- 93 -</b>
<b>5.3 Three-State Model for SAFIRE-OPIOM.....</b>	<b>- 96 -</b>
<b>5.4 Super-Resolution Application.....</b>	<b>- 98 -</b>
<b>5.5 Conclusion .....</b>	<b>- 100 -</b>
<b>CHAPTER 6 CONCLUSION AND OUTLOOK.....</b>	<b>- 102 -</b>

<b>APPENDIX A STUDYING PROTEIN-PROTEIN INTERACTIONS IN THE IMMUNE SYSTEM WITH FLUORESCENCE CORRELATION SPECTROSCOPY .....</b>	<b>- 106 -</b>
<b>A.1 Introduction .....</b>	<b>- 106 -</b>
<b>A.2 Results &amp; Discussions .....</b>	<b>- 108 -</b>
A.2.1 Weak PPIs: Low Binding Ratio .....	- 111 -
A.2.2 Sample Photobleaching .....	- 112 -
<b>A.3 Conclusion &amp; Outlook .....</b>	<b>- 112 -</b>
<b>REFERENCES.....</b>	<b>- 114 -</b>

## LIST OF TABLES

- Table 2.1 Differences between intensity modulation methods. a: The modulation waveform of EOM depends on drivers. A digital driver only allows square wave; an analog one can do square or sine wave. b: The max/min ratio depends on the laser beam size and collimation. A collimated laser with around 1 mm diameter shows higher ratio. c: The ratio of diode controller depends on the current (mA) range for each diode laser and the intensity needed in each experiment.....- 40 -
- Table 4.1 Summary of optically modulatable FPs and PS-FPs. Characteristic frequency ( $\nu_c$ ) means the frequency when enhancement drops to 50% of its maximum value. The primary (1<sup>st</sup>) and secondary (2<sup>nd</sup>) laser intensity for enhancement and characteristic frequency is: modBFP/H148K (1<sup>st</sup>: 560 W/cm<sup>2</sup>; 2<sup>nd</sup>: 36 kW/cm<sup>2</sup>), greens and yellows (1<sup>st</sup>: 1.9 kW/cm<sup>2</sup>; 2<sup>nd</sup>: 25 kW/cm<sup>2</sup>), red (1<sup>st</sup>: 13 kW/cm<sup>2</sup>; 2<sup>nd</sup>: 100 kW/cm<sup>2</sup>), PS-FPs (1<sup>st</sup>: 50 W/cm<sup>2</sup>; 2<sup>nd</sup>: 4 W/cm<sup>2</sup>).<sup>48-50, 112</sup> - 80 -
- Table 5.1 Photophysical parameters for rsFastLime.....- 97 -

## LIST OF FIGURES

- Figure 1.1 Jablonski diagram for fluorescence and phosphorescence. Adapted from Lakowicz.<sup>59</sup> ..... - 4 -
- Figure 1.2 Total internal reflection. (Left) The demonstration of Snell's Law. (Right) For biological samples, when the incident light from immersion oil reaches to critical angle ( $\theta_c$ ), no light will be transmitted into water medium thereby creating total internal reflection with evanescent wave. .... - 9 -
- Figure 1.3 The mechanism of GFP chromophore (Ser65-Tyr66-Gly67) maturation. The whole process does not require additional enzymatic catalysis, just the oxidation from oxygen. Adapted from Tsien.<sup>32</sup> ..... - 14 -
- Figure 1.4 Images of Dronpa crystal in bright state (top) and dark state (down). Dronpa is switched on by 405 nm laser and switched off by 488 nm laser while fluorescing. Adapted from Andresen.<sup>103</sup> ..... - 15 -
- Figure 1.5 The of excited-state proton transfer pathway from the chromophore to E222. Adapted from Shu.<sup>106</sup> ..... - 17 -
- Figure 1.6 The structure of cis- (green) and trans-chromophore (blue) of Dronpa under photo-isomerization. CYG is the chromophore of Dronpa, and R66, V157, S142, H193 are the surrounded residues close to the chromophore. On-state carbon, green; off-state carbon, light blue; oxygen, red; nitrogen, blue; sulfur, yellow. Water molecules are blue spheres. Adapted from Andresen.<sup>103</sup> .... - 18 -
- Figure 1.7 Fluorescence correlation spectroscopy (FCS). (A) FCS schematic plot. (B) A typical autocorrelation curve with the triplet and diffusive components.... - 24 -
- Figure 1.8 Range of PPIs and tools of study. Adapted from Fahrni.<sup>154</sup> ..... - 30 -
- Figure 1.9 Synchronously amplified fluorescence image recovery (SAFIRE). (A) Basic overview of SAFIRE. After the illumination of primary laser ( $h\nu_1$ ), some fluorophores fluoresce, while some others cross into the intermediate dark states. The molecules in the dark states will slowly thermally recover back to the ground state, while SAFIRE facilitates ground state recovery with secondary illumination ( $h\nu_2$ ) and then increases fluorophore brightness. Modulating the secondary laser intensity at a specific frequency, the fluorescence time trace will respond at the same modulation frequency, and can be selectively recovered. (B) Since the secondary laser is longer wavelength than fluorescence, the Fourier transform of fluorescence time trace from modulated secondary laser (1Hz) excludes modulatable signals from non-modulatable signals. After the fast Fourier transform (FFT), the modulated fluorescence is separated from non-modulatable autofluorescence, greatly improving signal-to-background ratio of the image. .... - 31 -

Figure 1.10 Frequency response from 2 <sup>nd</sup> laser modulation. (A) Definition of the phase difference ( $\phi$ ) and enhancement. (B) Fluorescence response (green) of ~1-ms dark state lifetime in response to 2 <sup>nd</sup> laser modulation (yellow). .....	32 -
Figure 2.1 Basic experimental setup for two-laser illumination and single-point detection. ....	36 -
Figure 2.2 Photophysics of rsFastLime. (A) Schematic of rsFastLime photophysical states. (B) Fluorescence data for continuous-wave 488 nm laser and square-wave 405 nm laser. The fitting of growth and decay concludes the photophysical parameters $k_{on}$ , $k_{off}$ , and $k_{off}^{0.50}$ . .....	41 -
Figure 2.3 Setup for an epi-fluorescence microscope.....	42 -
Figure 2.4 Spinning disk confocal unit, CSU 10, YOKOGAWA. ....	42 -
Figure 2.5 TIRFM setup. <sup>160</sup> Most of the back focal plane is inside an objective. Since the excitation laser is focused inside the objective, laser power should not exceed several mW. Adapted from Axelrod. <sup>160</sup> .....	44 -
Figure 2.6 Setup for FCCS experiment. (Top) Alignment for FCCS single-point detection. (Bottom) Image of HRT-41 and how to connect two APDs and SPC-630. ....	46 -
Figure 2.7 Setup for image-FCCS. (A) Optics alignment for image FCCS. The yellow circle is shown in photo (B). ....	49 -
Figure 2.8 ImFCS <sup>149, 161</sup> in ImageJ/FIJI for image-FCS and FCCS experiments. ....	50 -
Figure 3.1 OLID image of Dronpa in <i>Xenopus</i> embryo. (A) Fluorescence image of Dronpa-actin within a motor neuron in a live <i>Xenopus</i> embryo. The inset shows the internal reference waveform from optically switching of Dronpa-actin. (B) Correlation image of Dronpa-actin from fluorescence image (A) with largely suppressed background. Adapted from Marriott. <sup>38</sup> .....	54 -
Figure 3.2 Demodulation of modBFP/H148K-mito in live cells. Demodulation at 2 Hz directly yields images with an average (left) 7-fold and (right) 3-fold improvement of signal to autofluorescent background. Intensity modulated, secondary laser (514 nm) illumination is performed only within the white circle. Scale bar is 20 $\mu$ m. ....	55 -
Figure 3.3 Bright and dark states of PS-FPs with dual modulation SAFIRE (DM-SAFIRE). (Left) Optical control of PS-FPs. Both 488 nm laser and 405 nm laser excite the bright and dark states of rsFastLime (Dronpa/V157G), respectively. (Right) Dual modulation enables background-free detection of rsFastLime. rsFastLime interacts dependently with both 405 and 488 nm lasers, while the autofluorescence is excited independently by each laser. The fast Fourier transform (FFT) shows that only rsFastLime presents side-band	

signals (9-2 and 9+2 Hz) when 488 nm is modulated at 9 Hz and 405 nm at 2 Hz.....- 57 -

Figure 3.4 Comparison of single- and dual-modulation SAFIRE (SM, DM) vs. OLID in live NIH-3T3 cells co-expressing untargeted EGFP and mitochondria-targeted rsFastLime on a spinning disk confocal microscope. (A) (From left to right) Raw Image, Signal/Background~1.4; OLID, S/B~6; Demodulated image at 405nm frequency (SM-SAFIRE), S/B~5; Demodulation at the side-band frequencies (DM-SAFIRE), S/B~9. (B) Signal/background (S/B) comparison in the presence of bright EGFP background. (From left to right) Raw live cell image as in (A), S/B~1; OLID with automatic selection of brightest feature for reference waveform, S/B~1.6; OLID with manual selection of reference point, S/N~5; Demodulation image upon DM-SAFIRE, S/B~9. OLID with correct reference point and SM-SAFIRE give similar contrast improvements, while DM-SAFIRE show a further 2-fold improvement. Scale bars: 10  $\mu$ m.....- 60 -

Figure 3.5 DM-SAFIRE improves the imaging contrast of NIH-3T3 cells co-expressing untargeted EGFP and mitochondria-targeted rsFastLime on a widefield microscope. (Left) Raw fluorescence image. (Middle) OLID. (Right) Demodulation image at the sum and difference of primary and secondary modulation frequencies (DM-SAFIRE). Scale bars: 10  $\mu$ m.....- 60 -

Figure 3.6 Comparison between SAFIRE and OLID in live NIH-3T3 cells co-transfected with untargeted EGFP and mitochondria-targeted rsFastLime. (From left to right) SM-SAFIRE Fourier analysis (SAFIRE setup), DM-SAFIRE Fourier analysis (SAFIRE setup), OLID analysis (OLID setup), and SM-SAFIRE Fourier analysis (OLID setup). SAFIRE modulation utilizes 50% duty cycle, while OLID utilizes 50 ms per 1 s of 405nm laser exposure (5% duty cycle). Thus, both OLID and SM-SAFIRE (SAFIRE) contain auto-fluorescence background from high-energy laser excitation, while OLID data acquisition generates less auto-fluorescence than does SM-SAFIRE because of shorter bursts of 405nm laser exposure. In contrast, DM-SAFIRE is background free. In general, Fourier analysis of the OLID data, however, shows better image contrast than possible with OLID analysis, and approaches similar imaging contrast generated by DM-SAFIRE, just without the further applications to selective image multiple proteins based on dark state lifetimes or diffusional transit rate, mentioned in following sections. Scale bars: 10  $\mu$ m. ....- 62 -

Figure 3.7 Photophysics of rsFastLime (Dronpa-V157G). (A) Schematic of transitions between the bright and the dark states with ~518 nm fluorescence from 488nm excitation. Excitation at 405 nm depopulates the dark state and regenerates the bright manifold. (B) Continuous 488 nm and modulated 405 nm excitations yield fluorescence time traces showing exponential growth and decay. The growth is a function of 488 nm induced  $k_{on}$  ( $I_{488}\sigma_{488}\Phi_{dark}h^{-1}v_{488}^{-1}$ ), the thermal relaxation rate ( $k_{off}^0$ ), and the 405 nm induced dark state depopulation rate ( $I_{405}\sigma_{405}\Phi_{bright}h^{-1}v_{405}^{-1}$ ), while the decay is a similar function without the 405 nm induced rate. (C) Plotting the growth and decay rates vs the intensity at

488 nm yield the corresponding rate constants into (slope) and out of (intercept) the dark state. The 405 nm intensity is 14.4 W/cm<sup>2</sup>. (D) The intercepts of (C) from various 405 nm laser intensities are linear in both growth and decay plots. ....- 64 -

Figure 3.8 Contrast between immobilized mito-rsFastLime vs. diffusing untargeted-rsFastLime with varying excitation area. (A) Increasing laser spot size increases the diffusion time of untargeted-rsFastLime, allowing diffusing rsFastLime to be modulated (488 nm at 7 W/cm<sup>2</sup> and 405 nm at 3 W/cm<sup>2</sup>). Thus, the ratio of immobilized to diffusing molecules approaches unity in dual-modulation (DM) and single-modulation (SM). Because of autofluorescent background, the ratio in SM (~5) is much smaller than that achieved with DM (~25) in small excitation area. The major change is when the diffusional transit time of untargeted-rsFastLime increases beyond the 33 ms photophysical timescale. (B) Left: The DM-SAFIRE enhancement of immobilized (blue) and diffusing (purple) rsFastLime within the 1.4- $\mu$ m<sup>2</sup> excitation area. Right: The same DM-SAFIRE enhancement within a 140- $\mu$ m<sup>2</sup> excitation area. All FT signals were normalized by the amplitude at the 488 nm modulation frequency (13 Hz) for concentration-independent comparison.- 66 -

Figure 3.9 Diffusing vs. immobilized rsFastLime in cells co-expressing mito-rsFastLime and untargeted-rsFastLime. The ratio of sideband enhancement between the immobilized and diffusing molecules is ~10. 488 nm is 8.8 W/cm<sup>2</sup> modulated at 13 Hz, and 405 nm is 2.4 W/cm<sup>2</sup> modulated at 2 Hz. Scale bar: 10  $\mu$ m. - 67 -

Figure 3.10 Spectral unmixing based on modulation spectra. (A) Same-color Dronpa2 and rsFastLime show significant different enhancement vs. modulation frequency based on different dark state lifetimes. (B) Monte Carlo simulation of modulation spectral unmixing to separate identically emitting fluorophores by different frequency responses. a) Total image of two sets of spatially overlap fluorescent signals. Entire image is modulated by secondary laser at 10Hz and 100Hz. b) Modulation spectra of molecules with fast ( $\tau_{on}$  ~8 ms, green) and slow ( $\tau_{on}$  ~24 ms, red) photophysical parameters (both  $\tau_{off}$  ~8 ms). c) Slow and d) Fast molecule positions recovered from spectral unmixing by utilizing Fourier amplitudes from 10Hz and 100Hz at each pixel and the modulation spectra in b. e) composite image showing recovered fast (green) and slow (red) molecule positions. ....- 69 -

Figure 4.1 SAFIRE on fixed cells expressing untargeted-mVenus with CLSM (Zeiss). (A) Dwell time of laser scanning for one pixel is 8.44  $\mu$ s showing no demodulated signals. Left: Fluorescence. Right: Demodulation image. (B) Dwell time of laser scanning for one pixel is 270  $\mu$ s showing demodulated signals. Left: Fluorescence. Right: Demodulation image. Scale bar: 10  $\mu$ m. ....- 81 -

Figure 4.2 SAFIRE imaging with fixed cells expressing mitochondria-rsFastLime with confocal microscopes. (A) Within 1 frame, three channels of illumination are

applied. Channel 1: 488 nm (primary); Channel 2: 405 nm (secondary); Channel 3: 488 nm (primary). After the pre-illumination of 488 nm laser, the rsFastLime (rsFL) fluorescence of ch3 after the 405 nm recovery is much larger than ch1, while autofluorescence (autoFL) in ch3 is similar to that in ch1. (B) The fluorescence image (FL) and demodulation image (Demod) from CLSM. The Demod image was from the differences between fluorescence in ch3 and ch1, while FL image is the average of all fluorescence. (C) The fluorescence image (FL) and demodulation image (Demod) from SDCM. The Demod image was from the differences between fluorescence in ch3 and ch1, while FL image is the average of all fluorescence. Scale bar: 20  $\mu\text{m}$ ..... - 82 -

Figure 4.3 Demodulation of rsFastLime-VLPs from abundant autofluorescence in CV-1 cell line with a SDCM. (A) Fluorescence image. (B) Demodulation image. Scale bar: 20  $\mu\text{m}$ . ..... - 84 -

Figure 4.4 Nonlinear demodulation of rsFastLime-VLPs from CV-1 cell line with SDCM. (A) Differences between linear (ch1: 488 nm, ch2: 405 nm, ch3: 488 nm), and nonlinear (ch1: 488 nm, ch2: 405 nm, ch3: 488 nm, ch4: 488 nm) demodulations. Differences between 488nm-excited signals before (ch1) and after (ch3) 405 nm recovery generates linear demodulation, while nonlinear demodulation utilizes additional ch4 for calculation. The nonlinear processing successfully narrows the population of background signals compared to linear processing. (B) One photoswitching cycle of rsFastLime successfully demodulates VLP signals out of autofluorescence. Left: Fluorescence image. Right: Demodulation image. Scale bar: 20  $\mu\text{m}$ ..... - 85 -

Figure 4.5 No demodulated signals from EGFP-VLPs with nonlinear demodulation calculation with SDCM. (A) Fluorescence image. (B) Demodulation image. The only bright spot on the demodulated image is from the fluctuation of noise in the background, not from EGFP-VLPs. .... - 86 -

Figure 4.6 The combination of fluorescence (red) and demodulation (green) images on live cell imaging with a wide-field microscope. rsFastLime-VLPs can be observed in both central and peripheral area of CV-1 cell line even with abundant autofluorescence. Left: Video at frame 4. Right: Video at frame 35. The data acquisition time of each demodulation was around 500 ms, and each frame was taken at every 6 seconds. .... - 87 -

Figure 5.1 Modulation of laser excitation generates information of phase ( $\varphi$ ), from finite dark state lifetime, and enhancement, proportional to the population of optically modulatable dark state.<sup>59</sup> ..... - 90 -

Figure 5.2. Different ways for generating phase difference ( $\varphi$ ). (Left) Frequency-domain lifetime measurements. The modulated laser excites the ground state ( $S_0$ ), and then fluorescence (FL) emits from excited state ( $S_1$ ) with finite lifetime. (Middle) SM-SAFIRE. The modulated secondary ( $2^{\text{nd}}$ ) laser regenerates the ground state population from the dark state to enhance the fluorescence.

(Right) OPIOM. The modulated primary laser not only generates fluorescence but also creates dark state population. Since modulated lasers in frequency-domain lifetime measurements and SM-SAFIRE increase fluorescence signals, while the modulated laser in OPIOM not only generates fluorescence but also increases dark state population, the fluorescence waveform in OPIOM is different from frequency-domain lifetime measurements and SM-SAFIRE.....- 91 -

Figure 5.3 Fluorescence time trace of fluorescein and rsFastLime with sinusoidal primary laser modulation. Fluorescein with no obvious dark state follows the primary laser intensity, while rsFastLime shows and apparent “phase advance” from hysteresis of the dark state. ....- 92 -

Figure 5.4 PS-FP, rsFastLime, fluorescence time traces from sinusoidally intensity-modulated 488 nm excitation. Normalized curves are plotted relative to modulated fluorescein emission collected under identical conditions. Samples were co-illuminated at 405nm with intensities of (A) 0.25W/cm<sup>2</sup> and (B) 3W/cm<sup>2</sup>. Fluorescein emission tracks the excitation waveform, while rsFastLime fluorescence appears advanced in phase. The phase advance at a given modulation frequency changes with 405nm laser intensity. ....- 95 -

Figure 5.5 Experimental out-of-phase signals (FL<sub>out</sub>) upon varied 405nm laser intensity. (A) Out-of-phase (cosine) rsFastLime fluorescence amplitude resulting from sinusoidally modulated, 488nm (8 W/cm<sup>2</sup> average intensity) and continuous, homogeneous 405nm laser excitation for several 405nm intensities. At increasing 405nm intensities, the out of phase maxima shift from low to high frequency.....- 95 -

Figure 5.6 Heterogeneous 405 nm illumination creates different out-of-phase responses based on intensity profile. (Left) With weakly focused 405nm co-illumination in a much larger, spatially homogeneous wide field 488nm illumination, the out-of-phase (FL<sub>out</sub>) signal maximum increases in frequency at spatial positions exhibiting higher 405 nm secondary intensities. The raw fluorescence and out of phase maxima at each pixel are shown in the two images, with the color indicating the maximum of the out of phase signal at each pixel, while outside the 405 nm illumination spot, the fluorophores are unobservable (UnObs, black), as they are all switched into the dark state under 488 nm illumination alone. (Right) The plot shows the FL<sub>out</sub> amplitude vs. 488 nm modulation frequency for rsFastLime at low (square), medium (circle) and high (triangle) 405nm intensity. 488nm intensity, 40 W/cm<sup>2</sup>, is spatially invariant over the image. Scale bar: 1 μm. ....- 96 -

Figure 5.7 Three-state model. Left: The three-state model consists of a ground state (S<sub>0</sub>), an excited state (S<sub>1</sub>), and a dark state (D). After the laser excitation (k<sub>01</sub>), photons in S<sub>1</sub> fluoresce (k<sub>F</sub>) or turn (k<sub>D</sub>) into D, then thermally relaxation (k<sub>off</sub>) and laser-induced relaxation (k<sub>405,off</sub>) back to S<sub>0</sub>. Right: Rate matrix for the three-state model. ....- 97 -

Figure 5.8 Comparison between experimental data (red) and numerical simulation (black) using a three-state model of rsFastLime. rsFastLime is co-illuminated with 8 W/cm<sup>2</sup> at 488 nm and (Left) 0.25 W/cm<sup>2</sup>, (Center) 1 W/cm<sup>2</sup>, and (Right) 3 W/cm<sup>2</sup> at 405nm. (A) (B) (C) out-of-phase signals, FL<sub>out</sub>. (D) (E) (F) phase differences between excitation and rsFastLime emission.....- 98 -

Figure 5.9 Simulated resolution of two diffraction-limited molecular emission patterns, separated by 50 nm, and illuminated at 6-fold different 405nm intensities. (A) With the recovered FL<sub>out</sub> at two 405 nm intensities, we utilize spatially homogeneous 0.5Hz, 1Hz, 5Hz, and 10Hz modulated 488 nm excitation as reference values to spectrally unmix the overlap signals. (B) After point spread function convolution and FL<sub>out</sub> analysis, spectral unmixing of the modulation spectra enables recovery of the correct molecular positions, with a recovered distance of 49.2 nm. Scale bar: 250 nm. ....- 99 -

Figure A.1 T-cell response is triggered by a physical interaction with an APC (A) via pMHC binding to the TCR. (B) pMHC molecules are anchored on supported lipid bilayers to interact with TCR on T cells.....- 109 -

Figure A.2 Image FCS on supported lipid bilayers with pMHC-Cy5. (A) On a 21\*21 EMCCD pixel region, we acquire fluorescence time trace and calculate auto-correlation functions (ACF) with ImFCS (software developed by Wohland Laboratory, mentioned in Chapter 2),<sup>149-150, 161, 186</sup> which generates all 441 ACF curves and a histogram and map of fitted diffusion coefficients. (B) Either pMHC-Cy5 interacting with T cells or not shows similar average ACF curves. (C) Either pMHC-Cy5 interacting with T cells or not shows some (~5-10%) individual ACF curves with two populations. The fast component is ~0.01-0.1 second, and the slow one is ~0.1-1 second. ....- 110 -

Figure A.3 Image FCCS between TCR-CD3-TFP on T cells and pMHC-Cy5 on supported lipid bilayers with total-internal-reflection 451 nm and wide-field 633 nm lasers illumination. (A) Bright-field T cell images overlap with TCR-CD3-TFP aggregation images. T cells with obvious TCR-CD3-TFP aggregation stay at the same position for over 5 minutes, while other T cells are more mobile. Scale bar: 10 μm. (B) FCCS signals at the pixel with (left) or at the pixel without obvious TCR aggregation (right) are similar. The negative FCCS values and the dip around 1 second region are possible from the photobleaching correction.....- 111 -

## LIST OF SYMBOLS AND ABBREVIATIONS

$\varepsilon$	Extinction coefficient
$h$	Planck constant
$\Phi_{\text{FL}}$	Fluorescence quantum yield
FL	Fluorescence
$\text{FL}_{\text{out}}$	Out-of-phase fluorescence signal
$\sigma$	Absorption cross section
$\tau_{\text{FL}}$	Fluorescence lifetime
$k_{\text{on}}, k_{\text{D}}$	Rate into dark state
$k_{\text{off}}$	Rate out of dark state
$k_{\text{off}}^0$	Thermal relaxation rate from dark state to emissive manifold
$I_{\text{F}}$	Fluorescence intensity
$k_{\text{exc}}$	Excitation rate
$k_{\text{fl}}$	Fluorescence rate
D	Dark state
$S_0$	Ground state
$S_1$	1 <sup>st</sup> Excited State
$S_2$	2 <sup>nd</sup> Excited State
$\Phi_{\text{FL}}$	Fluorescence quantum yield
$\Phi_{\text{dark}}$	Dark state quantum yield (from bright to dark states)
$\Phi_{\text{rev}}, \Phi_{\text{bright}}$	Reverse quantum yield (from dark to bright states)

T <sub>1</sub>	First triplet state
<i>n</i>	Refractive index
acGFP	<i>Aequorea coerulea</i> green fluorescent protein
avGFP	<i>Aequorea victoria</i> green fluorescent protein
APD	Avalanche photodiode
BAM	Binding amplified microscopy
BFP	Blue fluorescent protein
CaM	Calmodulin
CCD	Charge coupled device
CLSM	Confocal Laser Scanning Microscope
CW	Continuous wave
DMEM	Dulbecco's modified eagle medium
DM-SAFIRE	Dual-modulation SAFIRE
DNA	Deoxyribonucleic acid
DOPC	1,2-dioleoyl-sn-glycero-3-phosphocholine
DPPE	1,2-dioleoyl-sn-glycero-3-phosphoethanolamine
DsRed	<i>Discosoma sp.</i> red fluorescent protein
EMCCD	Electron-multiplying charge-coupled device
EOM	Electro-optical modulator
FAD	Flavin adenine dinucleotide
FBS	Fetal bovine serum
FCS	Fluorescence correlation spectroscopy
FCCS	Fluorescence cross-correlation spectroscopy

FLIM	Fluorescence lifetime imaging microscopy
FMN	Flavin mononucleotide
FP	Fluorescent protein
FRET	Förster resonance energy transfer
GFP	Green fluorescent protein
HIV	Human immunodeficiency virus
MHC	Major histocompatibility complex
NADH	Nicotinamide adenine dinucleotide hydride
ND	Neutral density
OLID	Optical lock-in detection
OPIOM	Out-of-phase imaging after optical modulation
PALM	Photoactivated localization microscopy
PCH	Photon counting histograms
PMT	Photomultiplier tube
PPIs	Protein-protein interactions
PS-FPs	Photoswitchable Fluorescent Proteins
PSF	Point spread function
RESOLFT	Reversible saturable optical fluorescence transitions
SAFIRe	Synchronously amplified fluorescence image recovery
SDCM	Spinning disk confocal microscopy
SM-SAFIRe	Single-modulation SAFIRe
SOFI	Stochastic optical fluctuation imaging
SRM	Super-resolution microscopy

STED	Stimulated emission depletion
STORM	Stochastic optical reconstruction microscopy
TCSPC	Time-correlated single photon counting
TCR	T cell receptor
TTL	Transistor–transistor logic
VLPs	Virus-like-particles
YFP	Yellow fluorescent protein

## SUMMARY

Advances in fluorescence microscopy have greatly expanded applications in biology for visualization of targeted molecules in research and detection methods in diagnostics. Fluorescent proteins (FPs), from blue to red, offer biocompatibility and labeling specificity, especially for imaging *in vivo*. However, autofluorescent background limits imaging contrast and could generate false-positive signals. Furthermore, multi-color imaging based on emission spectra suffers from the spectral overlap of FPs, and the emission window of detection is limited to that of the visible light wavelength region (400-700 nm). There is a need to suppress autofluorescent background and expand dimensionality of fluorescence imaging would greatly benefit fluorescence microscopy.

The Dickson Laboratory has developed synchronously amplified fluorescence image recovery (SAFIRE) for selectively imaging modulatable fluorophores and eliminating same-color, non-modulatable species by utilizing photophysical dark states of FPs. Following prior research on FPs, this thesis continues to characterize the photophysical dark state a photoswitchable fluorescent protein (PS-FPs), rsFastLime. Dual modulation SAFIRE (DM-SAFIRE) suppresses 5-fold autofluorescent background by optically controlling the dark states of rsFastLime.

I continue to adapt SAFIRE to commercial microscopes, after successful demonstration on customized microscopes, in collaboration with Melikyan Laboratory to visualize rsFastLime-HIV-1 entry into CD4 cells. With a combination between SAFIRE and commercial microscopes, one SAFIRE image is taken around 0.5 second, a time scale for tracking virus in live cells.

The discrimination between rsFastLime and Dronpa2, with different dark state lifetimes, is proposed. In addition, controlling dark state lifetimes enables for selective imaging between immobilized or mobile yet the same modulatable FPs. The dark state lifetime of rsFastLime is optically controlled to be slower than diffusion time, so the diffusing rsFastLime cannot accumulate enough dark state population for demodulation, while immobilized rsFastLime show 10-fold signal more than diffusing ones.

Laser intensity modulation generates amplitude of fluorescent response as well as phase differences between excitation and emission. Out-of-phase imaging after optical modulation (OPIOM) can be detected under moderate secondary laser intensity ( $\sim 1 \text{ W/cm}^2$ ) on camera a few seconds after the dark state is accelerated by SAFIRE. After accurate prediction from a simple three-state model, SAFIRE-OPIOM is able to discriminate the molecules with different dark state lifetimes changed by secondary laser illumination, which may be applied to resolve two molecules within diffraction limit.

Dark states of FPs can serve as an additional dimension for advancing fluorescence microscopy by optically controlling dark state lifetimes of PS-FPs. This thesis demonstrated autofluorescence removal, selective imaging, and possible super resolution applications.

# CHAPTER 1 INTRODUCTION

## 1.1 Motivation

Fluorescence allows scientists to observe specific biological events *in vivo* with high spatial and temporal resolutions from complex intracellular backgrounds.<sup>1-11</sup> Current advances in fluorescence include the creation of brighter fluorescence dyes,<sup>12-16</sup> better spatially and time resolved fluorescence microscopy<sup>1, 3-4, 17-21</sup> and applications to biological systems including protein-protein interactions,<sup>22-24</sup> particle tracking,<sup>25-28</sup> and monitoring intracellular events.<sup>29-31</sup>

Fluorescent proteins (FPs) are widely used because of their specificity and high biocompatibility, quantitative labeling, and genetic encodability.<sup>32-34</sup> After years of study and evolution, the colors of FPs from blue to red provide multiple choices and emission windows for scientists. Exhibiting a wide range of color selections and high biocompatibility, FPs are usually fused with cellular proteins to study their interactions and dynamics. However, major limitations of FPs include signal discrimination versus autofluorescence,<sup>35</sup> detection of low-abundance complexes,<sup>36</sup> and spectral overlap with other exogenous fluorescent labels. Autofluorescence can be avoided by using red-fluorescent proteins, but this limits the choice of colors to carry out multi-color imaging.<sup>37</sup>

More recently, optically controllable dark states of photoswitchable fluorescent proteins (PS-FPs) are utilized for autofluorescence suppression<sup>38-41</sup> and selective imaging.<sup>42</sup> Optically controlling the fluorescence intensity of PS-FPs with optical lock-in detection (OLID)<sup>38, 40</sup> enables autofluorescence suppression, but this approach is nonlinear with respect to fluorophore concentrations and requires a background-free

internal reference point for calculation. Another approach, out-of-phase imaging after optical modulation (OPIOM),<sup>42</sup> discriminates autofluorescence and various PS-FPs based on different dark state lifetimes. Since a specific dark state lifetime generates a unique phase signal, different emitting fluorophores, including autofluorescence and multiple PS-FPs, can be selectively imaged. However, the time resolution of OPIOM is limited by the photophysics of PS-FPs, requiring several minutes to acquire one image.<sup>42</sup>

We have developed synchronously amplified fluorescence image recovery (SAFIRE), optically controlling the dark state lifetime of fluorophores with a secondary laser.<sup>43-44</sup> SAFIRE was demonstrated on silver nanoclusters,<sup>43, 45</sup> organic dyes,<sup>46-47</sup> and fluorescent proteins (FPs)<sup>48</sup> for background removal. The optical control of SAFIRE with the modulation of laser intensity does not require an internal reference dye, and the introduction of secondary laser illumination in SAFIRE shortens dark state lifetimes and facilitates the process of OPIOM tremendously.

Starting from SAFIRE, this thesis focuses on measuring the photophysical parameters and utilizing photophysical dark states of PS-FPs for background suppression,<sup>49-50</sup> signal discrimination between diffusing PS-FPs and immobilized PS-FPs,<sup>50</sup> spectral unmixing, great time resolution improvement of OPIOM, and possible applications to super-resolution microscopy.<sup>51</sup> In addition to performing experiments on customized microscopes, this thesis demonstrates SAFIRE on commercial fluorescence microscopes, including laser scanning confocal (Zeiss), spinning disk confocal (PerkinElmer), and wide-field fluorescence (GE) microscopes.

## 1.2 Introduction of Fluorescence

### 1.2.1 History of Fluorescence

The existence of microscopic organisms was discovered in the 17<sup>th</sup> century by Robert Hooke and Antoni van Leeuwenhoek. Hooke observed the fungus *Mucor*, while van Leeuwenhoek observed bacterial cells.<sup>52</sup> After more than 150 years, several advances from Ernst Abbe<sup>53</sup> and August Köhler<sup>54</sup> facilitated the development of efficient optical microscopes. Followed by the development of fluorescent probes, fluorescence microscopy has become a powerful tool to observe biological events, often with excellent signal-to-noise ratio.<sup>55</sup>

The first reported observation of photoluminescence was in 1560 by Bernardino de Sahagún<sup>56</sup> from materials that glow in the dark after the exposure to light. The term “fluorescence” was coined by Sir George Gabriel Stokes in his famous paper entitled “On the Refrangibility of Light”<sup>57</sup> in 1852.<sup>58</sup> In this paper, Stokes identified that fluorescence, which he called *dispersive reflection*, is always longer wavelength than that of the excitation light. This “Stokes shift” was later explained based on quantum physics.

### 1.2.2 Jablonski Diagram

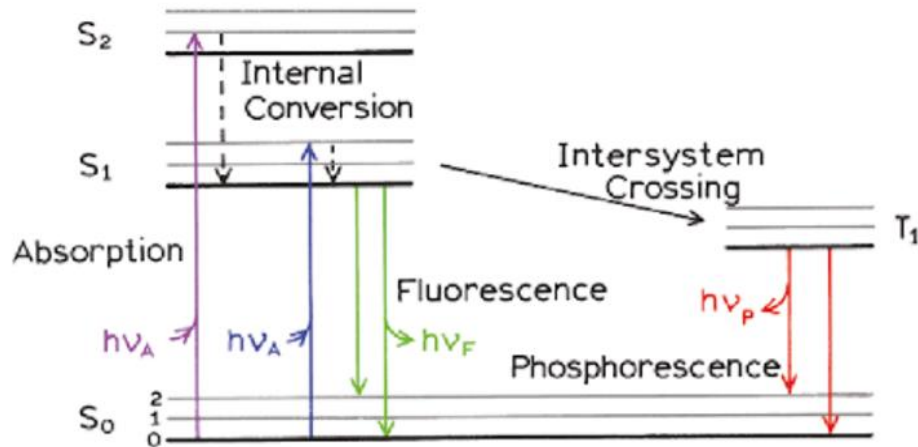


Figure 1.1 Jablonski diagram for fluorescence and phosphorescence. Adapted from Lakowicz.<sup>59</sup>

Fluorescence arises from transitions between different electronic states, as schematized in a Jablonski diagram (Figure 1.1).<sup>60</sup> After the fluorophore absorbs light of energy  $h\nu_A$  (violet or blue), the electrons are excited from electronic ground state ( $S_0$ ) to excited states ( $S_1$  or  $S_2$ ). The numbers 0, 1, 2 between the electronic levels are the vibrational states, with absorption and emission largely being initiated *from* the ground vibrational state of each electronic level. Excitation from  $S_0$  usually produces electronically and vibrationally-excited fluorophores, governed by the Franck–Condon principle. After rapid internal conversion, or vibrational relaxation to the ground vibrational state ( $\sim 10^{-12}$ s) of a given electronic level, fluorescence ( $10^{-9}$ s, time scale of fluorescence lifetime,  $\tau_{FL}$ ) occurs when the electrons undergo the  $S_1 \rightarrow S_0$  transition. Since vibrational relaxation occurs before the emission, fluorescence from the ground vibrational state of  $S_1$  to higher vibrational states of  $S_0$  is always longer wavelength (smaller energy) than the excitation wavelength ( $S_0 \rightarrow S_1$ ). This Stokes shift is crucial for fluorescence spectroscopy since scientists can shift the detection window to longer wavelength without scattering and reflection from excitation wavelength. Other pathways

from excited states such as intersystem crossing into triplet levels ( $T_1$ ) or photoisomerizational dark states can compete with emission ( $S_1 \rightarrow S_0$ ), resulting in fluorescence quantum yields which are always smaller than 1 ( $\Phi_{FL} < 1$ ). Emission from  $T_1$  is typically weak with longer lifetime ( $\sim 10^{-6}$ s), and this emission is longer wavelength than fluorescence, while the photoisomer typically does not result in emission as energy is used for internal motion, resulting in poor Franck-Condon overlap between ground and excited states.

#### 1.2.2.1 Reversible Dark States

Dark states (D) of fluorophores are defined as no signals at fluorescence emission window, including triplet states ( $T_1$ ) or nonemissive states. The pathways into dark states compete with emission to lower the quantum yield, and then the dark states would usually go back to the ground state by thermally relaxation ( $D \rightarrow S_0$ ). The temporal stay in dark states (D) was observed as blinking through single-molecule fluorescence imaging in 1997.<sup>61</sup> The temporary and reversible dark states serve as an additional parameter for the advancement of fluorescence techniques. In this thesis, I will introduce reversible dark states in fluorescent proteins, analyze the time scale of dark states as well as optically control them for solving current biological problems.

#### **1.2.2 Fluorescence Microscopy**

After the characterization of fluorescence from Stokes, fluorophores have stimulated the development of fluorescence microscopes since the 1930s.<sup>62</sup> In the 1960s, Ploem started to work with Schott on developing dichroic beam splitting plates (dichroic mirrors) and published the first paper on the epi-fluorescence microscope.<sup>63-64</sup> In addition to epi-fluorescence, the principle of confocal imaging developed by Marvin Minsky in 1957

led to confocal laser scanning microscopy (CLSM), gaining popularity in the 1980s by the introduction of commercially available laser scanning systems. The advantage of CLSM is optically sectioning on samples, rejecting out-of-focus signals. Typically, CLSM improves the imaging contrast and resolution in comparison with epi-fluorescence.<sup>65</sup>

Fluorescence microscopes with highly specific fluorescent staining dyes allow scientists to more directly observe intracellular events. Recent advancement of detectors, including photomultiplier tubes (PMT), avalanche photodiodes (APD), and charge-coupled devices (CCD), has improved the signal-to-noise ratio of imaging. Introduction of multiphoton (1931 publication of Maria Goppert-Mayer's doctoral dissertation) microscopy<sup>66</sup> improves additional optical sectioning, coupled with deeper penetration depths from long-wavelength excitation. Resulting from these advances, 3D multi-color imaging has become practical for scientists to understand complex biological systems. Recent developments including Bessel beam light-sheet microscopy<sup>67</sup> and adaptive optical correction of aberrations<sup>1-2</sup> continue to improve the time-resolution of 3D imaging and deepen penetration depth, approaching real-time non-invasive imaging in living creatures.

### **1.2.3 Common Fluorescence Microscopes**

The high contrast and specificity of fluorescence improve the observation of biological events. From nanoseconds to hours and nanometers to entire embryos, more fluorescence techniques have been developed to address myriad biological questions. Below, I will describe some general fluorescence imaging techniques related to this thesis.

### 1.2.3.1 Wide-Field & Confocal Microscopy

Illuminated by excitation light source, the fluorophores emit fluorescence as Stokes shift in longer wavelength than excitation as mentioned in section 1.2. By choosing proper excitation light source, excitation/emission filters, and a dichroic mirror, scientists can block the photons from scattering or reflection of excitation based on different wavelengths of excitation and emission. However, the emission of out-of-focus fluorophores will lower the imaging contrast. To avoid unfocused fluorescent signals, a pinhole is placed at the position of emission collection, corresponding to the excitation focal point. This pinhole filters out the unwanted signals from out-of-focus fluorescence signals to improve imaging contrast and quality. Main differences between wide-field and confocal fluorescence microscopes are broader imaging area for wide-field microscopy, while focused area with better imaging contrast is observed by a pinhole filtration in confocal microscopy.<sup>65</sup>

### 1.2.3.2 Spinning Disk Confocal Microscopy (SDCM)

Confocal laser scanning microscopy provides greater imaging contrast and resolution of optical imaging compared to epi-fluorescence microscopy since a pinhole at the detection side rejects out-of-focus emission. However, single point-scanning limits the frame rate for larger-view imaging or even 3D video. For example, even if one laser focused point takes only 1  $\mu$ s, 512\*512-pixel image requires several hundred milliseconds to seconds, possibly missing millisecond events in biological systems.

In order to achieve faster imaging rates, scientists began to develop imaging with multiple pinholes simultaneously for time resolution improvement without losing the imaging quality of confocal microscopy. The multiple-pinhole imaging began from

Nipkow disk, first implemented by David Egger and Mojmír Petráň in 1967.<sup>68</sup> After several generations of improvement,<sup>4, 69</sup> current spinning disk units can reach 2000 full frames per second (Yokogawa, CSU-X1), which is 0.5 ms per frame. The much improved time-resolution of SDCM enables biology groups to observe millisecond events in living cells<sup>70-71</sup> or even perform fluorescence correlation spectroscopy (FCS) experiments,<sup>72</sup> which will be introduced in the following section.

### 1.2.3.3 Total Internal Reflection Fluorescence Microscopy (TIRFM)

While wide-field imaging suffers from out-of-focus fluorescence along the z-axis, total internal reflection fluorescence microscopy (TIRFM) constrains the illumination within ~200 nm depth. Based on Snell's Law, the product of sinusoidal value of incident/transmitted angle ( $\theta_i$ ,  $\theta_t$ ) and refractive index ( $n_i$ ,  $n_t$ ) keeps constant (Figure 1.2). Since refractive index relates to dielectric property of medium, light in the medium with smaller refractive index travels faster and generates larger angle. For example, biological samples are usually observed in water solution on a glass slide or coverslip. The excitation light is from oil objective through immersion oil (1.42,  $n_{oil}$ ) into water (1.33,  $n_{water}$ ). Larger transmitted angle of water would have an angle larger than  $90^\circ$ , for no transmission (total internal reflection), while the angle of incident light from immersion oil is called critical angle ( $\theta_c$ ). No light is transmitted through the medium in total internal reflection, but it forms an evanescent electromagnetic field typically within 200 nm from the glass surface because of the exponential decay of the field.

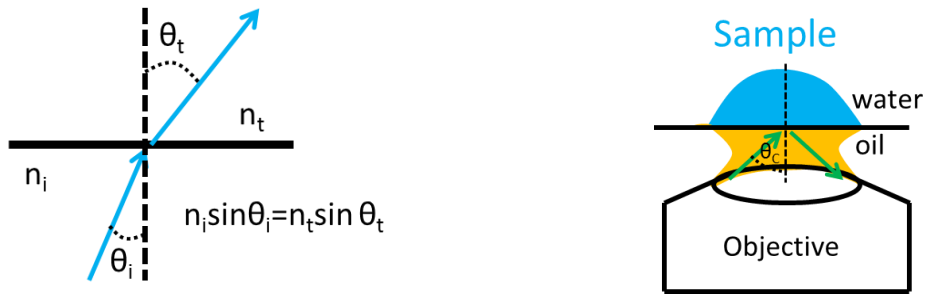


Figure 1.2 Total internal reflection. (Left) The demonstration of Snell's Law. (Right) For biological samples, when the incident light from immersion oil reaches to critical angle ( $\theta_c$ ), no light will be transmitted into water medium thereby creating total internal reflection with evanescent wave.

TIRFM greatly improves the imaging contrast of wide-field imaging without exciting fluorophores above evanescent field and still illuminates a larger area than confocal microscopy. With the advancement of charge-coupled device (CCD) cameras, TIRFM monitors a larger area faster. However, the limitation of TIRFM is that the evanescent wave only excites fluorophores close to the surface. If scientists need to observe the biological structures beyond a few hundred nanometers, TIRFM is not well-suited to the application.

#### 1.2.3.4 Super Resolution Microscopy (SRM)

The diffraction of light limits spatial resolution to  $\sim 200\text{nm}$ – the Abbe diffraction limit, identified in 1873. Since most molecules (proteins and DNA) are smaller than the diffraction limit, scientists have been working on super-resolution microscopy (SRM). The idea began in early 90s and has become practical since the mid-2000s.<sup>73-74</sup> Big breakthroughs include stimulated emission depletion (STED)<sup>19, 75</sup> and single-molecule localization microscopy, including stochastic optical reconstruction microscopy (STORM)<sup>18</sup> and photoactivated localization microscopy (PALM).<sup>17</sup> STED alters the point spread function of fluorescence by the illumination of a donut-shaped second laser to

stimulate the emission from the excited states to achieve resolution smaller 100nm,<sup>19, 75</sup> while the high precision of fluorophore localization in STORM and PALM reconstructs the super-resolved images.<sup>17-18</sup>

### **1.3 Choice of Fluorescent Dyes**

The choice of fluorescent dyes is made from how bright and how long the fluorescent signal lasts as well as the biocompatibility and specificity of dyes in the biological environment. Here are some principles for the choice of fluorescent dyes for biological applications:

- 1) Brightness (fluorescence quantum yield and absorption coefficient)
- 2) Chemical and photochemical stability
- 3) Biocompatibility (little toxicity without interference to biological systems)
- 4) High specificity and affinity to target (without nonspecific binding)
- 5) Easy and fast to target
- 6) Insensitive to the environment (temperature, pH, chemicals)

Each fluorophore has advantages and disadvantages. Based on projects, individual fluorophore is chosen for different applications.

#### **1.3.1 Intrinsic or Natural Fluorophores**

Intrinsic fluorescence often comes from amino acids with extended  $\pi$ -conjugate. Tryptophan, tyrosine, and phenylalanine are three amino acids emitting blue fluorescence (280-350 nm) by absorbing ultra-violet light (~280 nm).<sup>59, 76</sup> Other than common amino acids, enzyme cofactors are often fluorescent. Nicotinamide adenine dinucleotide (phosphate) (NAD(P)H), one of enzyme cofactors, is highly fluorescent with absorption and emission maxima at 340 and 460 nm. Another cofactor Flavins, including flavin

mononucleotide (FMN) and Flavin adenine dinucleotide (FAD), absorb ~450 nm and emit green fluorescence, ~525 nm. Other fluorescence source can be protoporphyrin IX emitting red fluorescence, ~635 nm.<sup>35, 59</sup> Since intrinsic fluorophores are not bright enough and easily to be quenched, they are rarely utilized for fluorescence detection. However, fluorescence detection without additional labeling process still draws attention for intrinsic fluorescence, or called autofluorescence, imaging.<sup>77</sup>

### 1.3.2 Extrinsic Fluorophores

Most common extrinsic fluorophores are organic dyes. Based on the idea of extended  $\pi$ -conjugate, scientists have engineered various fluorophores with bright emission from blue to near infrared. Common organic dyes include fluorescein, rhodamine, and cyanine family.<sup>78-79</sup> Dyes are often linked with a functional group for labeling reactions, and organic dyes are relatively small (<1 nm) compared to targeted proteins thereby minimizing perturbation for targeted proteins. Chemical reactions for protein labeling include succinimidyl-ester functional group reacting with primary amines ( $-\text{NH}_2$ ) or maleimide with a thiol group ( $-\text{SH}$ ). However, labeling specific proteins *in vivo* or delivery of labeled proteins is challenging.

Comparing to organic dyes, recent development of quantum dots greatly improves the brightness and photostability as well as narrows emission window for multiplexed imaging. However, *in vivo* labeling remains a great challenge, and one large quantum dot (6-60 nm) may attach several proteins.<sup>80</sup>

### 1.3.3 Fluorescent Proteins

Since the discovery of green fluorescence protein (GFP) from *Aequorea victoria* in the 1960s,<sup>81</sup> GFP and its derivatives have generated various fluorescent proteins (FPs)

from blue to red. FPs have been developed and widely utilized for fluorescence techniques because of the excellent biocompatibility and high specificity to the biological targets. Labeling a FP with a protein only requires introduction and expression of the engineered gene combining the FP and the protein (FP-protein) without additional chemical reactions. Expression of the FP-protein gene would generate the protein attached to the FP at 1-to-1 ratio *in vivo*. Since the saturation of FPs does not need help from additional enzymes, FPs can be applied to universal biological systems. Also, protected by 11-stranded  $\beta$ -barrel, chromophores of FPs is insensitive to collision quenching and robust to environmental changes. Though moderate brightness of FPs limits the imaging quality in high autofluorescence environment, several benefits for fluorescence imaging *in vivo* has greatly impacted biology research. Therefore, this thesis analyzes as well as applies the photophysical dark states of FPs for improving imaging quality.

#### **1.4 Fluorescent Proteins**

Within the past 20 years, fluorescent proteins (FPs) have become the preferred fluorescent labels in biological imaging. They show great utility in visualizing cellular compartments,<sup>3, 17-18, 42, 70, 82</sup> tracking biological events<sup>6, 25, 28, 83-84</sup> and measuring intracellular interactions.<sup>23, 85-92</sup> Compared to common extrinsic dyes, FPs are easily labeled with target proteins through gene expression *in vivo*. Therefore, the imaging data presented in this thesis are from FPs, and the advancement of fluorescence microscopy is based on the photophysical dark states of FPs.

### 1.4.1 Introduction of Fluorescent Proteins

Collecting jellyfish *Aequorea victoria*, Osamu Shimomura first isolated green fluorescent protein (GFP)<sup>93</sup> in the 1960s and characterized its excitation and emission spectra. Wild-type GFP contains 238 residues, 11-stranded  $\beta$ -barrel surrounding the center chromophore (Ser65-Tyr66-Gly67). Excited by blue light, GFP emits green fluorescence at about 510nm. Without understanding the maturation mechanism of GFP, scientists once believed the fluorescent form of GFP requires further assistance of other enzymes in *Aequorea victoria* after translation. However, the successful expression of GFP in *E. coli* and *C. elegans*<sup>94</sup> demonstrated the wide biocompatibility among various biological systems without other enzymatic assistance. It demonstrated GFP as a universal genetic marker. The fusion between GFP and a target protein without obvious perturbation of the systems greatly broadens the fluorescence applications to cell biology.

After the research of GFP expression within *E. coli* in an anaerobic environment,<sup>95</sup> Tsien proposed a maturation mechanism of GFP chromophore, which included the introduction of oxygen to form the p-hydroxybenzylidene-imidazolidinone chromophore (Figure 1.3) (GFP maturation). After understanding the chromophore and crystal structure<sup>96-97</sup> of GFP, scientists began to create multiple mutants with different colors, brighter chromophores, and tailor photophysics. Precisely targeting FPs to desired proteins, scientists widely apply FPs to fluorescence imaging *in vivo* for understanding biological processes. Also, multi-color GFP mutants allow scientists to label multiple targets and visualize complex interactions, moving from molecular biology to systems biology.

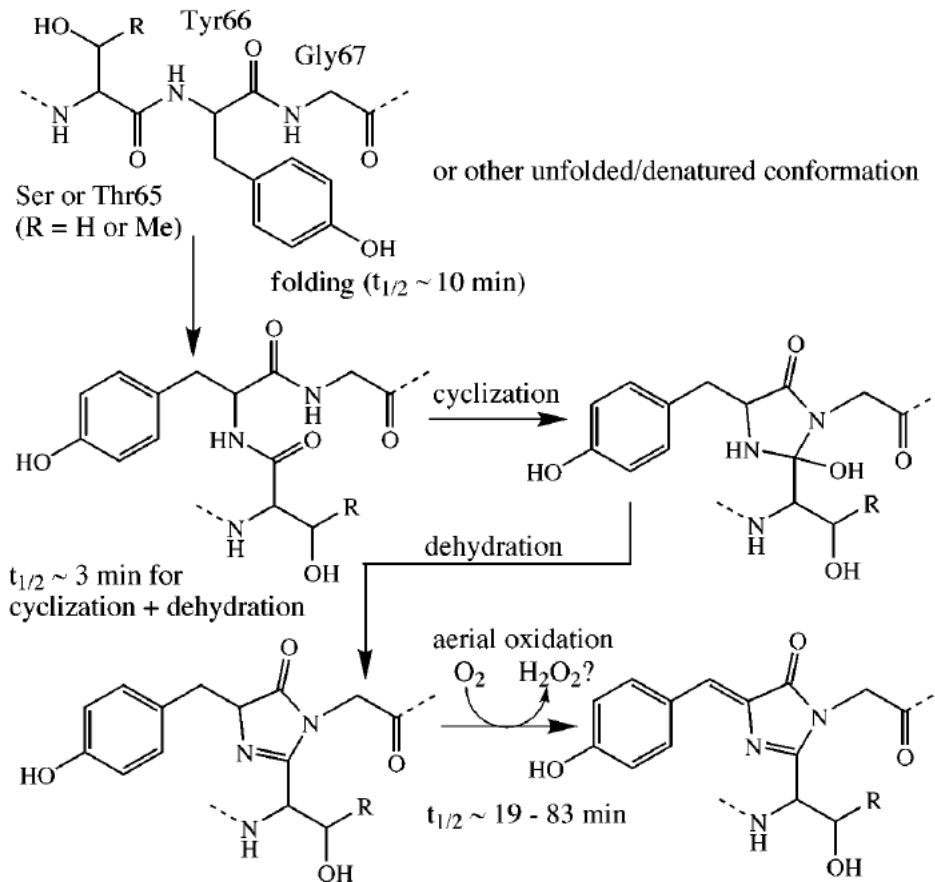


Figure 1.3 The mechanism of GFP chromophore (Ser65-Tyr66-Gly67) maturation. The whole process does not require additional enzymatic catalysis, just the oxidation from oxygen. Adapted from Tsien.<sup>32</sup>

Since 1992, the impact of GFP has influenced more than 20,000 publications.<sup>81</sup>

#### 1.4.2 Photoswitchable Fluorescent Proteins (PS-FPs)

Since the discovery of blinking events in GFP mutants,<sup>61</sup> scientists have been pursuing reversible optical control of the blinking events. The first reported reversible photoswitchable fluorescent protein (PS-FP) in 2000 is asFP595,<sup>98</sup> a GFP homolog from sea anemone *Anemonia sulcata*. This protein is not ideal as it exhibits low contrast between bright and dark states and exists as a tetramer. After several years, a monomeric PS-FP with higher contrast named Dronpa, “dron” from a ninja term for vanishing and “pa” from photoactivation. It was mutated from Pectiniidae, a species of coral emitting weak

fluorescence upon irradiation with ultraviolet light.<sup>99</sup> Illuminated by 488 nm excitation, some Dronpa proteins fluoresce green, while some Dronpa molecules nonradiatively decay from the excited states into a long-lived dark state (840 minutes).<sup>100</sup> Since the dark state is long-lived, all bright Dronpa proteins become dark after continuous 488 nm illumination. This dark state is optically accessible. Excitation with another light source, around 400nm, quickly recovers the non-emissive form of Dronpa to the emissive form (Figure 1.4). Extremely efficient recovery by a secondary light source allows scientists to optically control the dark state population as an additional parameter to improve fluorescence microscopy. For example, one form of super-resolution spectroscopy, stochastic optical fluctuation imaging (SOFI),<sup>3, 101</sup> correlates the blinking of Dronpa to improve spatial resolution of the emission point spread function (PSF), or an improved STED, reversible saturable optical fluorescence transitions (RESOLFT),<sup>102</sup> utilizes the dark state of asFP595 to lessen the extremely high intensity needed in STED microscopy.

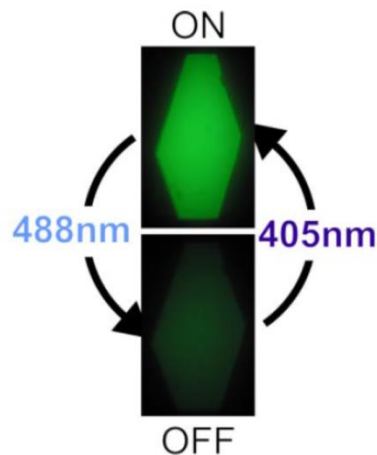


Figure 1.4 Images of Dronpa crystal in bright state (top) and dark state (down). Dronpa is switched on by 405 nm laser and switched off by 488 nm laser while fluorescing. Adapted from Andresen.<sup>103</sup>

### 1.4.3 Protein Structure

In addition to the mechanism of chromophore maturation,<sup>95</sup> two independent papers detailing the GFP structure<sup>96-97</sup> in 1996 enabled modification of the chromophore environment to create multi-color FPs and enhance its emission. Wild-type GFP contains 11-stranded  $\beta$ -barrel surrounding the center chromophore (Ser65-Tyr66-Gly67). Since the  $\beta$ -barrel protects the chromophore from the environment, other enzymes cannot approach the chromophore to catalyze its maturation. The rigid protein structure also contributes to the high fluorescence quantum yield and small Stokes shift, while the surrounding residues interact with the chromophore to affect the photophysics. Because of these characteristics, enhanced green fluorescent protein (EGFP)<sup>104</sup> interrupts the excited state proton transfer by mutating Ser65 to Thr65, and most yellow fluorescent proteins (YFP)<sup>32</sup> include the mutation (Thr203 to Tyr203) for  $\pi$ - $\pi$  interactions with the chromophore. Aside from the effects of a few specific mutations, the relationship between the structure and optical property of FPs is still unclear especially for photophysical dark states.

### 1.4.4 Protein Photophysics

Since the elucidation of the GFP crystal structure, the photophysics of many FP mutants have been studied. The surrounding amino acids of the tight  $\beta$ -barrel affect the chromophore tremendously with polar-polar interactions, H-bonding, or steric interference. Below are some widely studied mechanisms explaining the photophysics of FPs.

#### 1.4.4.1 Excited-state proton transfer

Excited-state proton transfer has been proposed to explain the large Stokes shift between violet absorption (398nm) and green fluorescence (504nm) in wild-type GFP

(wtGFP). Mutation studies suggest that the neutral form of the electronically excited chromophore undergoes a proton transfer from the chromophore through Ser205 to Glu222 (Figure 1.5).<sup>105</sup> Blocking this pathway, scientists were able to generate blue FPs (BFPs, wtGFP-S205V/T203V) with only blue absorption (390 nm) and blue emission (459 nm), or the EGFP (wtGFP-S65T) with only blue-green absorption (488 nm) and green emission (508 nm) by maintaining the anionic chromophore. Similarly, different absorption spectra of PS-FPs result from preferential stabilization of either the neutral or anionic states of the chromophore. Therefore, photophysical properties are related to the protonation state of the FP chromophore.

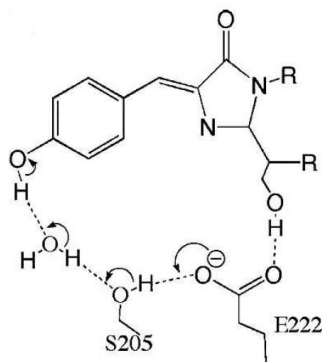


Figure 1.5 The of excited-state proton transfer pathway from the chromophore to E222. Adapted from Shu.<sup>106</sup>

#### 1.4.4.2 Cis-trans isomerization

In order to optically control FP emission, scientists developed reversible photoswitchable fluorescent proteins (PS-FPs) with controllable dark states (section 1.4.2). Among the various proposed mechanisms for photo-accessible states, photo-induced cis-trans isomerization has been confirmed by x-ray crystallography as an active pathway that is involved in the transition between bright (on) and dark (off) states of Dronpa as well as other kindling proteins and PS-FPs.<sup>100, 107-110</sup> The Dronpa crystal structure demonstrated that bright state is the cis-chromophore, while the dark Dronpa is

the trans-chromophore (Figure 1.6).<sup>103</sup> Since the Dronpa crystal structures of bright and dark states were solved, point mutations have been made to change the rate of cis-trans isomerization. For example, the mutation, rsFastLime (Dronpa-V157G),<sup>100</sup> removes the steric hindrance for cis-trans isomerization to create a photoswitchable Dronpa mutant with a shorter dark state lifetime (8 minutes).<sup>100</sup>

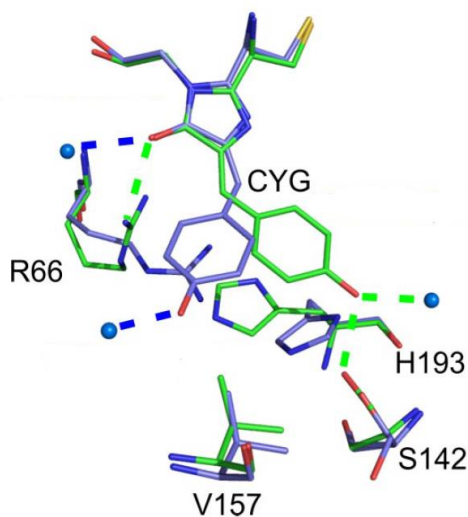


Figure 1.6 The structure of cis- (green) and trans-chromophore (blue) of Dronpa under photo-isomerization. CYG is the chromophore of Dronpa, and R66, V157, S142, H193 are the surrounded residues close to the chromophore. On-state carbon, green; off-state carbon, light blue; oxygen, red; nitrogen, blue; sulfur, yellow. Water molecules are blue spheres. Adapted from Andresen.<sup>103</sup>

Since the first demonstration of optical control of FP dark states,<sup>61</sup> engineering of FP dark states has been widely explored for advancing fluorescence microscopy. For example, by autocorrelating the time trace of blinking PS-FPs, super-resolution optical fluctuation imaging (SOFI)<sup>3, 101</sup> post-processes images with narrower point spread function (PSF). Since the blinking of each PS-FPs is unique, autocorrelation of fluorescence fluctuation from different PS-FPs would vanish, while only fluctuation from a same blinking

fluorophore can generate autocorrelation signals. Therefore, PSF engineering comes from the stochastic blinking of PS-FPs. This post-processing super-resolution is applicable for CCD camera imaging, easy to be adapted to general imaging platforms (confocal, spinning disk, and TIRF microscopes). Also, stochastic processes of blinking PS-FPs do not require synchronization of PS-FPs photoactivation, and the autocorrelation is not limited to PS-FPs concentration.

Reversible photophysical dark states in PS-FPs create additional parameters for not only SOFI but also optical lock-in detection (OLID)<sup>38, 40</sup> and out-of-phase signal detection (OPIOM), both utilizing dark states of PS-FPs to suppress autofluorescent background. Details of OLID and OPIOM will be in chapter 3 and 5, respectively. Thus, I will further utilize dark states of PS-FPs to improve fluorescence microscopes and solve biological problems.

#### 1.4.4.3 Dark states of FPs

In addition to designed dark states of PS-FPs, some widely used FPs have optically controllable dark states.<sup>48-49, 111-112</sup> The Dickson laboratory has developed optical modulation (mentioned in 1.5) for better imaging contrast by modulating the dark state residence time. Coincidentally, dark states of different FPs, originating from *Aequorea victoria* to *Discosoma sp.*,<sup>33, 113-114</sup> all have similar transient absorption spectra in the near infrared region (700-900 nm) with ~millisecond lifetime. The mechanisms of dark states may be cis-trans isomerization or dianionic chromophore.

The ~millisecond dark state lifetime suggests the modulatable dark states likely involve cis-trans isomerization, though excited-state protonation/deprotonation is also likely to be involved. Trans-chromophore from cis-trans isomerization can be torsional

and flexible, disrupting the  $\pi$ -conjugate.<sup>103</sup> The study of Dronpa shows trans-chromophore state (dark state) is more flexible than cis-chromophore state (bright state) since the hydrogen bonds are fewer in trans-state.<sup>115</sup> Also, isomerization of Padron, one of PS-FPs, from cis to trans breaks the planar structure and increases the flexibility of trans-chromophore according to crystal structure.<sup>110, 116</sup> Cis-trans isomerization requires not only the conformation change of chromophore but also the rearrangement of surrounding peptides. This conformational change requires much longer time (~ms-s) than protonation/deprotonation (~ps) thereby a possible explanation for the dark states of some FPs. However, current discovered cis-trans isomerization is excited in visible region (400-600 nm), so the transient absorption in near infrared region (700-900 nm) may be other cis-trans isomerization mechanisms.

In addition to the conformational change, the study of red fluorescent proteins (KillerRed, mRFP, and mDsRed) reported long time-scale transient absorption ( $\mu$ s-s) with a peak between 720-740 nm.<sup>117</sup> Combined with molecular dynamics simulations, this research indicated the dianion chromophore is a likely candidate for the long-wavelength absorbing dark state and is stabilized by Arg95, a conserved peptide in *Aequorea victoria* jellyfish green fluorescent protein (avGFP, origin of EGFP, EYFP, mVenus),<sup>33</sup> *Aequorea coerulea* colorless fluorescent protein (acGFPL, origin of AcGFP),<sup>113</sup> and *Discosoma sp.* red fluorescent protein (DsRed, origin of mDsRed and mCherry).<sup>114</sup> Other proposed photoinduced transformations in FPs such as charge transfer, oxidation/reduction, photoconversions, and hydration/dehydration might explain similar near-infrared spectra of dark states in various FPs.<sup>116, 118-119</sup>

### 1.4.5 Applications

The great biocompatibility and high specificity of FPs enable fluorescence imaging in all biological systems. Multi-color imaging also helps scientists understand interactions within intracellular compartments. In addition, thanks to photophysical dark states, super-resolution optical fluctuation imaging (SOFI) post-processes images and narrows the point-square-function (PSF) by stochastic blinking of PS-FPs.

Besides to visualization of cells, FPs can also be utilized with all fluorescence techniques, especially the study *in vivo*. Investigation of intracellular protein dynamics will be described in section 1.5, including fluorescence recovery after photobleaching (FRAP), fluorescence correlation spectroscopy (FCS), Förster resonance energy transfer (FRET), and fluorescence lifetime imaging microscopy (FLIM).

Other than being fused with targets, some FPs can sense  $\text{Ca}^{2+}$ ,  $\text{Zn}^{2+}$ <sup>120-123</sup> or pH, pressure, redox indicators<sup>124</sup> in living cells.<sup>125</sup> For example, Cameleon is a FRET pair of CFP and YFP conjugated with  $\text{Ca}^{2+}$  binding sites, including calmodulin (CaM) and a CaM-binding peptide of myosin light chain kinase (M13), developed for detecting free  $\text{Ca}^{2+}$  in the range  $10^{-8}$  to  $10^{-2}$  M.<sup>120</sup> In absence of  $\text{Ca}^{2+}$ , CaM is unbound to M13, so CFP and YFP are far apart without Förster resonance energy transfer, which fluorescence signals only come from CFP (480 nm). In presence of  $\text{Ca}^{2+}$ , CaM and M13 form a complex by binding to  $\text{Ca}^{2+}$ , so CFP transfers energy efficiently to YFP within closer distance thereby emitting yellow fluorescence (535 nm). Therefore, the 535-to-480 nm fluorescence ratio indicates the  $\text{Ca}^{2+}$  concentration. Cameleon and other  $\text{Ca}^{2+}$  indicators<sup>121</sup> greatly benefit research in neuronal transmission, muscle contractions and other signal transduction pathways *in vivo*. Similarly,  $\text{Zn}^{2+}$  sensors developed as FRET pair for monitoring

intracellular  $Zn^{2+}$  concentration.<sup>122-123</sup> Engineered FPs are also available for detecting intracellular redox-ratio (roGFP)<sup>124</sup> and voltage differences across cell membrane (FlaSh).<sup>126-127</sup> These genetic-encoded indicators monitor intracellular molecules or physical conditions for scientists to understand neuroscience, metabolism, signal transduction, and cell proliferation.

## **1.5 Fluorescence Techniques for Protein Dynamics**

Fluorescence microscopes allow scientists for visualizing labeled proteins in biological samples, benefiting from high biocompatibility and specificity of FPs. Protein dynamics can also be monitored by tracking the location and time of fluorescence labeled proteins, so diffusion coefficients can be calculated. Protein dynamics can be observed not only by single-particle tracking. Here are some common fluorescence techniques for understanding the protein dynamics *in vivo*.

### **1.5.1 Fluorescence Recovery after Photobleaching (FRAP)**

Fluorescence recovery after photobleaching (FRAP) is to monitor the actions of fluorophores in biological systems, including diffusion and interactions. First, a small region (two-dimensional area or three-dimensional volume) of diffusing molecules is irreversibly photobleached from exposure of an intense pulse of excitation light. Then, fluorescence recovery of the dark region is from moving out of the bleached fluorophores within the region and moving in from the surrounding unbleached fluorophores. The fluorescence recovery curve relates to the geometry of photobleaching pulse, the diffusion rate of fluorophores, existence of diffusional hindrance, and additional parameters from protein-protein interactions. Careful control experiments and detailed mathematical models are necessary for FRAP to fully understand the biological actions.

Beginning from 1970s, FRAP was introduced to understand the diffusion within membranes.<sup>128-129</sup> Since the protein-protein interactions affect the fluorescence recovery time trace, FRAP is often utilized for understanding the intracellular interactions *in vivo*.<sup>23, 87, 130-131</sup> Although the observation of fluorescence recovery time trace is straightforward, scientists demonstrated the choice of fitting models and photobleach profile should be carefully calibrated, or the fitting results would become problematic.<sup>88</sup> In addition to the necessity of proper calibration, phototoxicity is another concern because of the high intensity illumination for photobleaching.

### **1.5.2 Fluorescence Correlation and Cross-Correlation Spectroscopy (FCS, FCCS)**

Instead of the fitting fluorescence recovery vs. time as in FRAP, scientists can collect the stream of emitted photons and correlate fluorescence fluctuations to characterize dye photophysics, translational diffusion, and even protein-protein interactions.<sup>132-141</sup> The fluorescence detection from less than 100 molecules in a laser-focused region can track the brightness change of each fluorophore in a fluorescence time trace, either from photophysical blinking or leaving the focus region (Figure 1.7A). From autocorrelation of the fluorescence time trace, the characteristic time scale of change in the whole fluorophore population is shown in a fluorescence correlation spectroscopy (FCS) curve (Figure 1.7B).

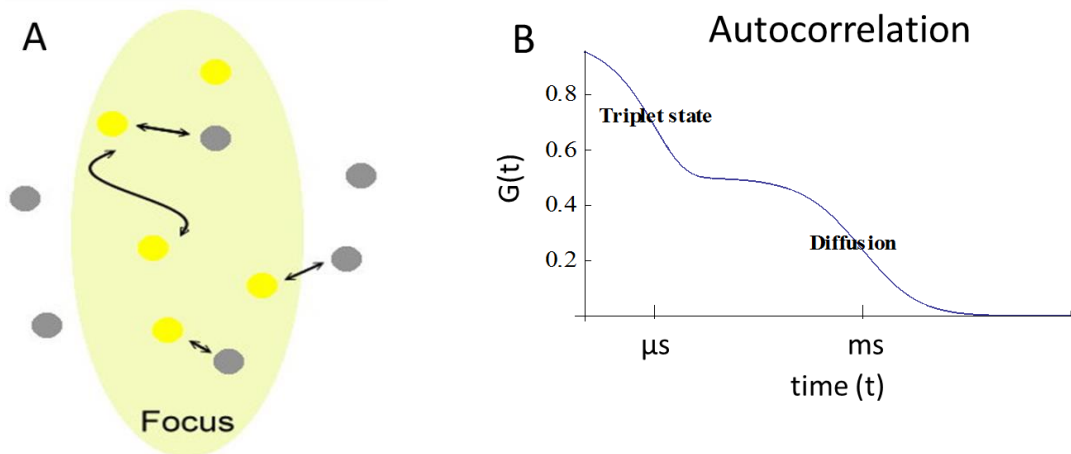


Figure 1.7 Fluorescence correlation spectroscopy (FCS). (A) FCS schematic plot. (B) A typical autocorrelation curve with the triplet and diffusive components

For example, if a fluorophore blinks inside the laser focus, the bright and dark transition will be captured in the fluorescence time trace and demonstrated in a FCS curve. Similarly, if fluorophores diffuse in and out or the bound molecules stay longer in the laser focal spot, the correlation of fluorescence time trace will demonstrate the time scales of diffusion and binding. Fluctuation of fluorescence time trace monitors all the above events simply based on bright or dark state of a fluorophore, either from photophysical blinking or diffusion. Autocorrelation of the fluorescence time trace reveals the time scale of each event population. Since FCS monitors the fluctuation from fluorophore signals, too many fluctuation events would lower the contrast of correlation signal to be unobservable. In addition, each molecule should be bright enough for FCS to capture individual events, so the signal-to-noise ratio depends on the brightness of each molecule.<sup>135</sup> Typical illumination intensity for FCS is around  $0.1\text{-}1 \text{ kW/cm}^2$  to produce  $\sim 100\text{-}1000$  photons per second for each fluorophore,<sup>46, 142-143</sup> which may induce photobleaching during experiment. Therefore, a low concentration of bright fluorophores, coupled with extremely low background is critical for FCS data acquisition.

Following the same idea, cross-correlation of fluctuating signals from two different color fluorophores demonstrates how strong these two fluorophores move together, called fluorescence cross-correlation spectroscopy (FCCS).<sup>144-145</sup> Similar to FCS, if a green and a red fluorophores correlate with each other at the same bright/dark time scale, they move together through binding. The stronger two molecules bind together, the longer the two fluorescence time traces are correlated thereby generating larger contrast in cross-correlation signals. By calculating autocorrelation (FCS) and cross-correlation (FCCS) curves, scientists can monitor the total population in each color as well as the population of binding complex. This technique shows the equilibrium of binding/unbinding molecules at the focus area in biological samples. FCCS has been utilized widely for investigating protein-protein interactions or binding events in living cells and on cell membranes.<sup>8, 86, 91, 142, 146</sup>

Based on the same experimental methods in FCS and FCCS, fluorescence time trace can be analyzed for photon counting histograms (PCH). Brightness of each moving species is summarized in a histogram to understand protein aggregation<sup>24, 147-148</sup> since dimers or oligomers are brighter than monomer. Wide-field FCS<sup>5, 141, 149-152</sup> monitors much wider region for understanding diffusional or population map. These have been developed and applied to understand many biological systems.

### **1.5.3 Förster Resonance Energy Transfer (FRET) and Fluorescence Lifetime Imaging Microscopy (FLIM)**

If one fluorophore's (donor) emission window overlaps with another (acceptor) excitation window, the efficiency of dipole-dipole energy transfer ( $E_{\text{FRET}}$ ) between these two depends on Equation 1.1.

$$E_{\text{FRET}} = (1 + (r/R_0)^6)^{-1} \quad \text{Equation 1.1}$$

The energy transfer efficiency ( $E_{\text{FRET}}$ ) depends on the distance ( $r$ ) between a donor and an acceptor with inverse 6th-power law based on the mechanism of dipole-dipole interaction. The Förster distance,  $R_0$ , relates to spectral overlap between donor emission and acceptor absorbance, refractive index of environment, and dipole orientation. The efficiency is 50% when the distance ( $r$ ) equals to the Förster distance ( $R_0$ ), and typically  $R_0$  is around 4-5 nm. Förster resonance energy transfer (FRET) is a fast process, quenching donor's emission. Since the energy transfer only happens when a donor and acceptor are close, acceptor emission only appears when two molecules are close enough. Since the high distance dependency and spectral shift from donor to acceptor emission, FRET is widely utilized for protein-protein interactions thanks to short distance between a donor and an acceptor when binding. By calculating the ratio of donor and acceptor fluorescence, scientists can monitor the bulk binding and unbinding population or observe real-time binding events by single-molecule fluorescence detection. The problems of FRET are from the collection of donor and acceptor fluorescence, including the noise from autofluorescence background, dye concentrations especially the uncertainty of FPs expression levels, and emission bleed-through from donor to the acceptor emission window.

Similar to FRET, the fluorescence lifetime of a donor changes when the donor energy transfers to a near acceptor. Fluorescence-lifetime imaging microscopy (FLIM) monitors the fluorescence lifetime of a donor. If a donor is close to an acceptor, additional relaxation pathway for excited states shortens the fluorescence lifetime. Compared to FRET, the lifetime monitoring in FLIM largely avoids concentration problems including expression level differences *in vivo* and fluorescence bleed-through.

However, the fitting of short donor fluorescence lifetime might be difficult from the time resolution of a detector or dim donors after Förster energy transfer.

## **1.6 Limitations of Current Fluorescence Techniques**

### **1.6.1 Autofluorescent Background**

Autofluorescence in biological samples can be found in common amino acids, including tryptophan, tyrosine, and phenylalanine absorbing ultra-violet light (~280 nm) and emitting blue fluorescence (280-350 nm).<sup>59, 76</sup> Other fluorescent sources can be enzyme cofactors. Enzyme cofactor NAD(P)H is highly fluorescent with absorption and emission maxima at 340 and 460 nm; Flavins absorb ~450 nm and emit green fluorescence, ~525 nm.<sup>35, 59</sup> All the intrinsic fluorophores either uniformly distribute or concentrate in some cellular compartments, creating uniform and non-uniform background. Uniform autofluorescence lowers the fluorescence imaging contrast, and non-uniform one shows false-positive signals. Since the emission of autofluorescence is mainly less than 600 nm,<sup>35</sup> utilizing red FPs is an alternative way to avoid most background.<sup>114, 153</sup> However, protoporphyrin IX emits red fluorescence (~635 nm), and some biological systems may contain different autofluorescent sources with red emission according to the Melikyan Laboratory. In addition, if scientists can only choose red FPs, this will greatly limit the choices of FPs and the spectral real estate for multi-color imaging.

To differentiate autofluorescence and FP emission, one may be able to utilize the different emission spectra between autofluorescence and FPs by spectrally unmixing the two populations. However, this approach needs to understand autofluorescence spectrum for unmixing calculation. Recently, multiple fluorescence techniques have been developed for avoiding autofluorescence, including OLID and OPIOM.<sup>38, 40-42</sup> These two methods,

mentioned in chapter 3 and 5, can successfully separate PS-FPs targeted structures from background. However, OLID correlates fluorescence signals at each pixel to an internal reference signal from a background-free bead. This calculation may be skewed if the background-free signals are contaminated by autofluorescence. In addition, the OLID calculation is nonlinear, so the recovered images often show the brightest signals, and final recovered intensities are not representative of the real protein concentration. OPIOM can selectively image PS-FPs without an internal reference, but it suffers from long PS-FP dark state lifetimes, which are limited from the cis-trans isomerization and protein conformational changes. Therefore, I introduce a secondary laser to optically control the photophysical dark states of PS-FPs for better imaging quality compared to OLID and better time resolution compared to OPIOM.

Following the development of autofluorescence suppression, selective imaging based on time scales of photophysical dark states can broaden the limited FPs choices because of emission spectra overlap. Spectral overlap with long emission tail of FPs complicates the filter choice and limits multi-color imaging. Therefore, introducing additional axis to FPs discrimination would be a significant advance for multi-particle imaging.

### **1.6.2 Detection of Weak Protein-Protein Interactions (PPIs)**

In addition to visualizing structure or specific proteins, scientists identify and characterize intracellular protein-protein interactions (PPIs) through fluorescence microscopy and spectroscopy. Different from existing tools, including co-immunoprecipitation, chemical cross-linking, and two-hybrid systems, fluorescence techniques (e.g. FRAP, FCS/FCCS, FRET) measure weaker PPIs with better spatial precision and real-time measurement. However, all fluorescence techniques suffer from

convolution of binding and diffusing as well as overwhelming unbound fluorophores of weak PPIs, which lower the signal contrast of binding complex thereby limiting the detection of PPIs from current techniques (Figure 1.8). In addition, FRAP requires careful control experiments to acquire correct information of PPIs, and the phototoxicity concern in the photobleaching step. FCS is stringent about concentration range for detection, and convolution between diffusion, photobleaching and PPIs can be problematic, which will be mentioned in appendix. Although bound molecules emit acceptor not donor fluorescence in FRET, emission bleed-through from the donor to acceptor channel contributes small amount of false-positive FRET signals thereby limiting the detection of weak PPIs. Also, finding FRET pairs with right distance, orientation, and not disturbing the interactions requires tremendous works. Therefore, our lab began development of binding amplified microscopy (BAM), which will be mentioned in chapter 3, for only enhancing binding molecules by utilizing photophysical dark states and expanding the detection range in regard of protein concentration, binding time, and binding constant. BAM will be a more universal way to investigate weak PPIs *in vivo*.

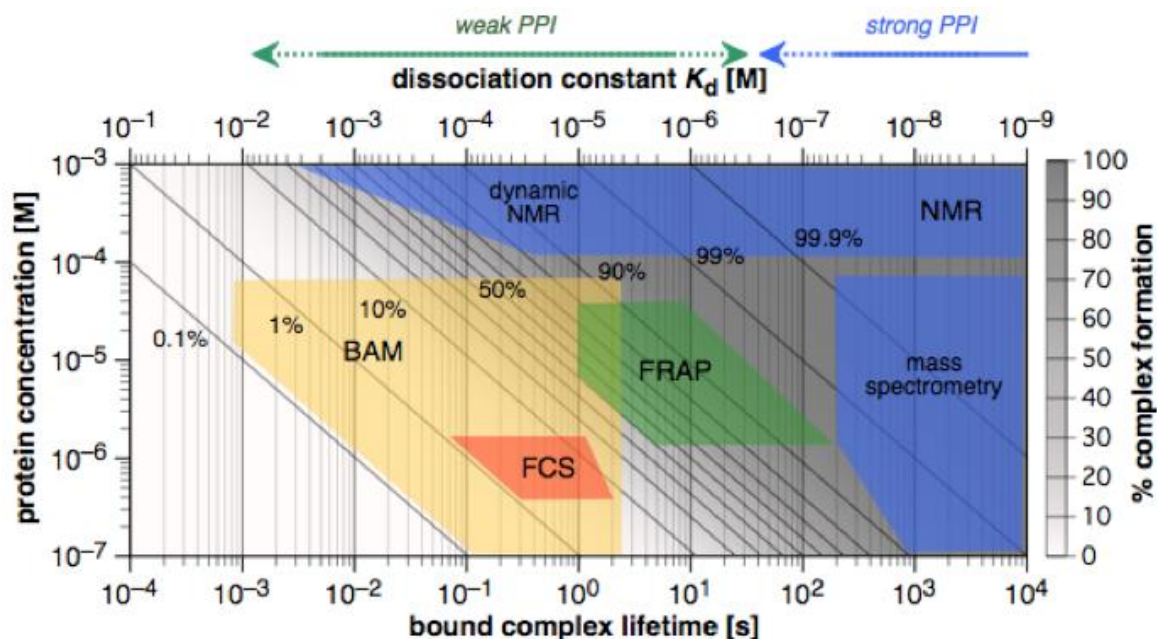


Figure 1.8 Range of PPIs and tools of study. Adapted from Fahrni.<sup>154</sup>

### 1.7 Optical Modulation

Since the major limitations of FPs include signal discrimination versus autofluorescence and other fluorescent labels, especially for low copy number proteins/complexes, advanced fluorescence techniques are required to avoid autofluorescence robustly, allowing for multiplexed imaging and BAM. Our lab has developed synchronously amplified fluorescence image recovery (SAFIRE) to externally modulate the optical modulatable dark states of dyes with a secondary laser. External modulation of a secondary laser with longer wavelength than fluorescence only recovers the modulatable fluorophores without nonmodulatable same-emission-wavelength backgrounds (Figure 1.9). Starting from silver nanoclusters<sup>43</sup> and organic dyes,<sup>44</sup> we have demonstrated some modulatable FPs<sup>48-49</sup> for enhancing the contrast of imaging in high background environments up to 20-fold signal-to-background improvement. SAFIRE controls the optically accessible dark state population by dynamically regenerating the original ground state of the emissive manifold faster than it would normally recover from

the long-lived dark state. This approach can be used for selective image recovery, both as autofluorescence suppression and as an additional parameter for multiplexed imaging of multiple fluorophores or immobilized molecules, which will be explained in detail in chapter 3.

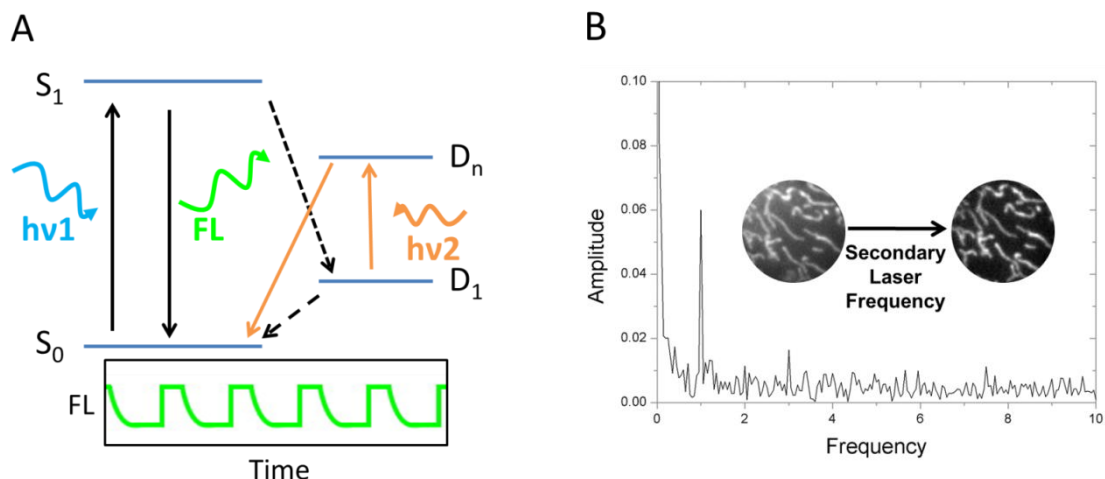


Figure 1.9 Synchronously amplified fluorescence image recovery (SAFIRE). (A) Basic overview of SAFIRE. After the illumination of primary laser ( $h\nu_1$ ), some fluorophores fluoresce, while some others cross into the intermediate dark states. The molecules in the dark states will slowly thermally recover back to the ground state, while SAFIRE facilitates ground state recovery with secondary illumination ( $h\nu_2$ ) and then increases fluorophore brightness. Modulating the secondary laser intensity at a specific frequency, the fluorescence time trace will respond at the same modulation frequency, and can be selectively recovered. (B) Since the secondary laser is longer wavelength than fluorescence, the Fourier transform of fluorescence time trace from modulated secondary laser (1Hz) excludes modulatable signals from non-modulatable signals. After the fast Fourier transform (FFT), the modulated fluorescence is separated from non-modulatable autofluorescence, greatly improving signal-to-background ratio of the image.

SAFIRE recovers the fluorescence out of optically modulatable dark states, and the fluorescence recovery depends on dark state lifetime and the frequency of secondary laser modulation. After the modulation of secondary laser, the fluorescence response contains two components (Figure 1.10A): (1) The time lag between laser excitation and fluorophore emission, which is called phase ( $\phi$ ) difference. (2) The amplitude differences between primary laser ( $1^{\text{st}}$ ) and primary plus secondary lasers ( $1^{\text{st}}+2^{\text{nd}}$ ), which the ratio (two lasers: one laser) is called enhancement. Fluorescence recovery by  $2^{\text{nd}}$  laser excitation is delayed

by finite dark state lifetime, and the enhancement is proportional to the population of optically modulated dark state. If the 2<sup>nd</sup> laser modulation is slower than the dark state lifetime, fluorescence response can follow the modulation with minimal phase difference and maximal enhancement. When the modulation goes faster than the dark state lifetime, the phase difference will be larger but smaller enhancement since the dark state cannot follow the modulation speed (Figure 1.10B).

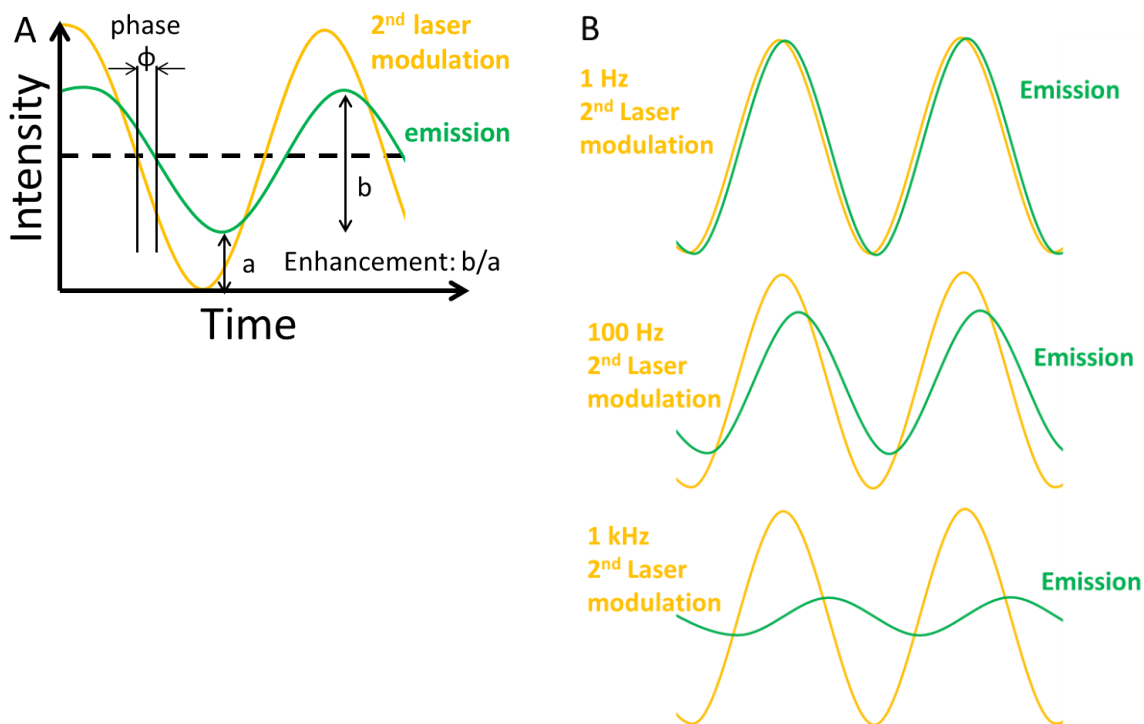


Figure 1.10 Frequency response from 2<sup>nd</sup> laser modulation. (A) Definition of the phase difference ( $\phi$ ) and enhancement. (B) Fluorescence response (green) of  $\sim$ 1-ms dark state lifetime in response to 2<sup>nd</sup> laser modulation (yellow).

In this thesis, I will begin with SAFIRE on optically modulated FPs and an adjusted version of SAFIRE for PS-FPs. After analyzing the population and lifetime of the dark state

of rsFastLime, I further utilized SAFIRE for autofluorescence suppression, discriminating diffusing and immobilized molecules, and possible applications to super-resolution microscopy. Based from SAFIRE techniques, multiple biological applications will be presented in the following chapters.

## CHAPTER 2 EXPERIMENTAL METHODS

### 2.1 Sample Preparation

#### 2.1.1 Organic Dyes

In this thesis, organic fluorophores are largely utilized for aligning optics and as photophysical controls. Alignment of each laser requires a dye that absorbs at that wavelength. Fluorescein is used for blue lasers (451, 488 nm); Texas Red is used for the 594 nm laser; Cy5 is used for the 633 nm laser. Each dye is dissolved in either deionized water or buffer. Typical concentrations for alignment are  $\sim 1 \mu\text{M}$  ( $\sim 50\text{k}$  photons per second with weaker laser intensity ( $\sim 10 \text{ W/cm}^2$ )), and the concentration for FCS is less than  $50 \text{ nM}$  to have less than 30 molecules ( $\sim 10\text{k}$  photons per second with stronger laser intensity ( $100\text{-}1000 \text{ W/cm}^2$ )) in the laser focus.

#### 2.1.2 Fluorescent Proteins & Biological Samples

The Fahrni laboratory has designed, expressed, purified and provided multiple FPs and PS-FPs samples, including purified proteins as well as fixed and live 3T3-NIH cells with various fluorescently labeled structures. Most proteins were either fused with mitochondria for visualization or untargeted as diffusing background. The Fahrni lab fixed cells with 3% paraformaldehyde in PBS and then mounted them onto glass slides. Live cells were prepared in Fahrni laboratory and then taken back for imaging experiments on a heated stage (Bioptics).<sup>50, 112</sup>

The Melikyan laboratory provided the CV1 cell line with both CD4 receptors and CXCR4 co-receptors cultured in Dulbecco's modified eagle medium (DMEM) supplemented with 10% fetal bovine serum (FBS) and 100U penicillin-streptomycin.<sup>84</sup>

Virus-like-particles (VLPs, pseudovirus)<sup>6, 84</sup> are labeled with rsFastLime fused to Vpr which associates with the viral core. Pure VLPs or fixed VLPs with cells were provided. Pure VLPs are stored at -20 °C. Fixed cell samples are stored at 4 °C. The fixation protocol also uses 3% paraformaldehyde, and imaging buffer is 20 mM HEPES at pH 7.4 with 2% serum. Live cell imaging is performed at Emory on a wide-field microscope (Personal DeltaVision, Applied Precision, GE).

For protein-protein interaction experiments, Chenghao Ge from the Zhu laboratory prepares lipid bilayers (99.9% 1,2-dioleoyl-sn-glycero-3-phosphocholine (DOPC) and 0.1% 1,2-dioleoyl-sn-glycero-3-phosphoethanolamine-N-(cap biotinyl) (sodium salt) (DPPE-biotin)) by extrusion method,<sup>155</sup> pMHC-Cy5 (RQF-T) labeled proteins and 1E6 T cells with CD3 fused with TFP.<sup>156</sup>

## **2.2 Fluorescence Microscopy: Single-Point Detection**

Experiments were performed on an inverted microscope (Olympus IX-71, IX-70) placed on an optical table. Excitation sources are continuous lasers from temperature controlled fiber-coupled diode lasers (ThorLabs) or a line-tunable Ar<sup>+</sup> laser (Coherent). When experiments require two lasers, the two laser beams are overlapped on the optical table by combining both light sources with a dichroic mirror (Semrock or Chroma) before entering the microscope. To modulate the laser intensity, laser diode driving current is sinusoidally modulated with a function generator or chopped by an electro-optic modulator (EOM, ConOptics). After the light enters into a microscope, a 60x, 100x oil or 60x water objective (Olympus) is used for the experiments in this thesis. Samples are placed on either a coverslip (Fisher Scientific, Fisherfinest™ Premium Cover Glasses, 12-548B), 35 mm glass bottom dish (MatTek), or a 96-well imaging plate with 0.2 mm

glass. With an appropriate emission filter (Semrock or Chroma), fluorescence signals are collected through a 50- $\mu\text{m}$  or 100- $\mu\text{m}$  multimode fiber (Oz or ThorLabs) as a pinhole by a photon-counting avalanche photodiode (APD, PerkinElmer or Excelitas) coupled to a photon counting board (either Becker & Hickl SPC-630 or National Instruments BNC-2121, Figure 2.1).

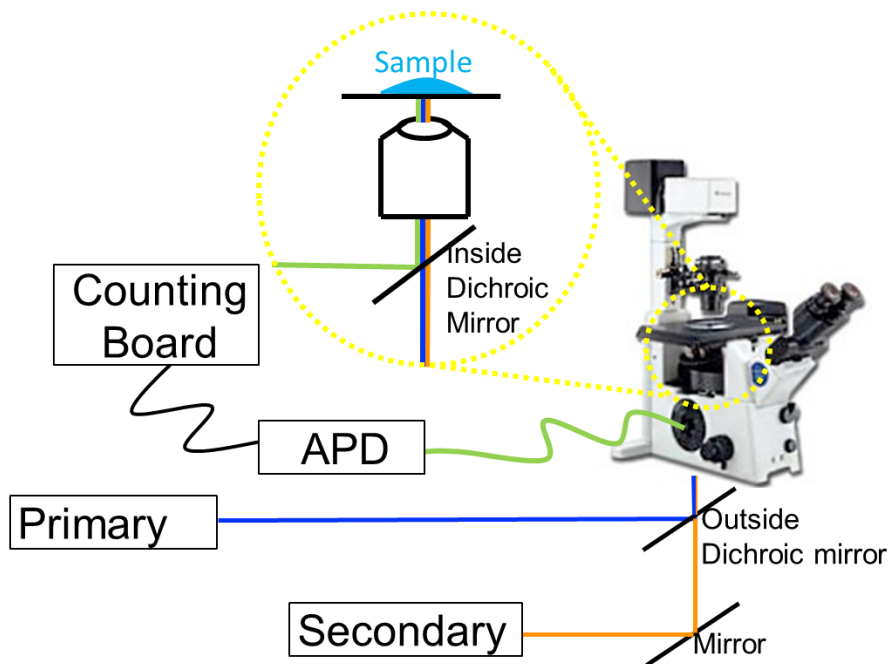


Figure 2.1 Basic experimental setup for two-laser illumination and single-point detection.

### 2.2.1 Light Source

Current continuous laser light sources in the Dickson laboratory range from 400 nm to 1400 nm, including line-tunable  $\text{Ar}^+$  lasers (Coherent), temperature controlled fiber-coupled diode lasers (ThorLabs), Ti:Sapphire lasers (Mira, Coherent) with a frequency-doubled optical parametric oscillator (OPO), 561 nm solid-state laser (Coherent, Compass), 542 nm He-Ne laser (Research Electro-Optics, Inc.), 594 or 633 nm He-Ne lasers (JDS Uniphase and Melles-Griot). Before turning on a laser, cooling systems for high power lasers ( $\text{Ar}^+$  and Ti:Sapphire lasers) are necessary, and no

reflective accessories are allowed in a laser room, including rings, watches, or necklaces. Laser alignment begins with adequate attenuation (reflective or absorptive neutral density filters, ThorLabs), to reach  $\sim 10 \mu\text{W}$ . External collimation of excitation laser light is necessary for most light sources, as they have non-zero divergence, and the state of laser polarization may be changed if needed.

### **2.2.2 Optics**

Most mirrors, lenses, polarizers, holders, and mounts are from ThorLabs. Proper cleaning of optics with methanol and lens paper is necessary. Correct optics depend on the wavelength of the laser for two main categories, visible and near-IR. For different experiments, the diameter of the laser beam usually ranges from 1-3 millimeters, and the laser beam is usually aligned parallel to an optical table for easier alignment modification. Neutral density filters (ND filters) are required for adjusting the laser intensity to visible but not dangerous ranges (around 1-10  $\mu\text{W}$ ) while also being able to adjust intensities for experimental needs once the laser is aligned. Near-IR laser alignment requires an IR viewer or IR paper for visualizing the IR laser beam.

### **2.2.3 Microscopes & Objectives**

The power limit into high magnification objectives are typically several mW. These power thresholds must not be exceeded if the laser is being focused inside the objective as with epi-illumination or total internal reflection. For collimated light into the objective, the higher end of this range should be fine without burning the internal optics and adhesives. Objectives used in this thesis are a 60x water or oil, or 100x oil objective (Olympus) with numerical aperture (NA) ranging from 1.2 to 1.4, on either an Olympus IX 70 or IX 71. The main difference between these two microscopes is the length of

side-port adapter – IX 71 requires a longer side-port adaptor than does the IX 70, due to the longer physical width of the IX-70 microscope body.

#### **2.2.4 Detectors & Photon Counting Boards**

After the fluorescence is directed into side-port collected by a 50- $\mu\text{m}$  or 100- $\mu\text{m}$  multimode fiber (Oz or ThorLabs), an APD converts photons into electronic signals for detection. While APDs output  $\sim 2$  V electronic signals (transistor–transistor logic, TTL pulses), a photon counting board (SPC-630, Becker & Hickl) takes -50 mV to -1 V as input to the constant fraction discriminator, CFD. An inverter with attenuation (PicoQuant GmbH, input 2V, output -300 mV) is used for converting TTL pulses from  $\sim 2$  V into  $\sim -300$  mV, while BNC-2121 (National Instruments) have been designed for receiving signals at  $\sim 2$  V, without an inverter/attenuator. Generally, the upper count rate for photon counting boards (SPC-630 and BNC-2121) are around 200 thousands per second to avoid saturation. Count rates exceeding this limit require attenuation or special settings.

For the SPC-630 (Becker & Hickl), the synchronization frequency is usually set from 8-10 MHz by a function generator or pulse laser controller. Generally, the input photon count rate needs to be less than 0.01-0.1 photon per signal period to avoid pile-up effect and maintain signal linearity. Count rates higher than this range may require a reversed setup (details in SPC-630 manual). CFD, TAC, and ADC count rates should be similar, or the settings of threshold need to be changed. The program controlling the BNC-2121 was written by Jung-Cheng Hsiang in LabVIEW or in Visual C. Connection of the channels is detailed in the instructions of the program. Details of specific experiments in this thesis are described in the following sections.

## **2.3 Fluorescence Microscopy: Wide-Field Detection**

In addition to the single-point detection, I have utilized and developed new wide-field fluorescence microscopy techniques. Standard microscopy configurations used include epi-fluorescence microscopy, total internal reflection microscopy (TIRF), and spinning disk confocal microscopy (SDCM). An electron-multiplying charge-coupled device (EMCCD, Andor iXon) is connected to a trinocular head or side-port of a microscope for detecting a larger area ( $20 \times 20 \mu\text{m}^2$ ) than an area when using a tightly focused laser spot ( $0.2 \times 0.2 \mu\text{m}^2$ ).

### **2.3.1 EMCCD**

EMCCD cameras offer multiple channels for simultaneous detection in a larger field. Although the camera time resolution (milliseconds) is much slower than that of the APD (picoseconds), typical biological interactions or behaviors are readily characterized on the millisecond timescale. The sacrifice of fast time resolution in exchange of significantly larger detection area is preferable for observing larger areas or volumes. The CCD detector converts photons into electronic signals at each of the  $512 \times 512$  pixels, and weak signals are amplified by electron multiplication (EM). The EM successfully overcomes the read noise introduced by the output amplifier and offers imaging rates in excess of 50 frames per second for a full frame ( $512 \times 512$  pixels). Therefore, EMCCD is applicable to widefield imaging, autofluorescence suppression by SAFIRe, SAFIRe-OPIOM, and image FCS/FCCS.

## 2.4 Optical Alignments for Each Microscope

### 2.4.1 Single-Modulation & Dual-Modulation SAFIRE (SM- & DM-SAFIRE)

Similar to Figure 2.1, single-modulation SAFIRE (SM-SAFIRE) or dual-modulation SAFIRE (DM-SAFIRE), details mentioned in chapter 3, requires only an additional mechanical shutter (Stanford Research Systems), EOM (ConOptics), or the diode controller of ThorLabs that allows amplitude modulation. The main differences of these three systems are summarized in Table 2.1.

Table 2.1 Differences between intensity modulation methods. a: The modulation waveform of EOM depends on drivers. A digital driver only allows square wave; an analog one can do square or sine wave. b: The max/min ratio depends on the laser beam size and collimation. A collimated laser with around 1 mm diameter shows higher ratio. c: The ratio of diode controller depends on the current (mA) range for each diode laser and the intensity needed in each experiment.

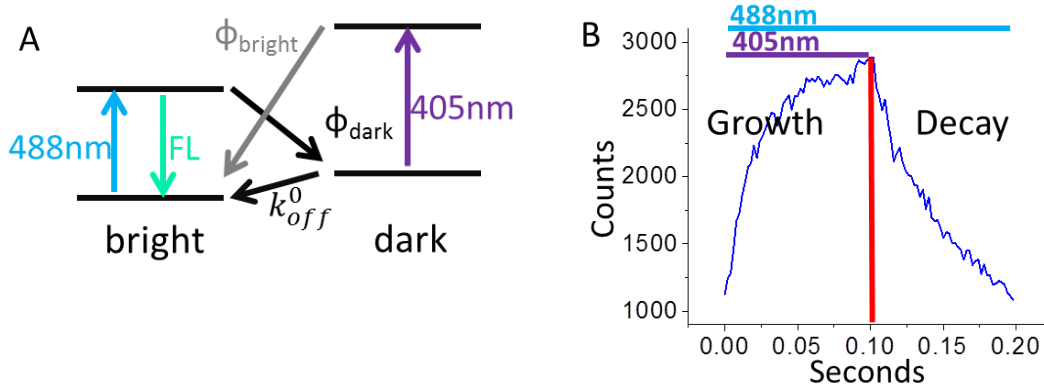
	<b>Time Resolution</b>	<b>Laser Modulation Waveform</b>	<b>Max/Min Intensity Ratio</b>
<b>Shutter</b>	~100 Hz	Square	$\infty$ (Totally Blocked)
<b>EOM</b>	~10 MHz	Square or Sine <sup>a</sup>	50-500 <sup>b</sup>
<b>Diode Controller</b>	150 kHz	Sine	50-100 <sup>c</sup>

Usage of the EOM also requires additional attention for the wavelength of light source, visible or near-IR laser. An incorrect crystal will generate poor performance. When it comes to optical alignment, the available space on an optical table also need to be considered since EOM takes more space than other equipment.

#### 2.4.1.1 Measurement of Dark State Lifetimes

For calculating  $k_{on}$  and  $k_{off}$  of rsFastLime (Figure 2.2), continuous wave 488-nm primary excitation and square wave-modulated (5 Hz) 405-nm secondary excitation was used on rsFastLime fixed cell samples. The exponential increase and decay of the

fluorescence intensity can be used to calculate the rate into the dark state ( $k_{on}$ ) and the 405 nm laser induced rate out of the dark state ( $k_{off}$ ), as well as thermally recovered ( $k_{off}^0$ ) decay constant (Figure 2.2), details mentioned in chapter 3.



$$\text{Growth: } k_{on} + k_{off} = I_{488} \sigma_{488} \Phi_{dark} \frac{1}{h\nu} + k_{off}^0 + I_{405} \sigma_{405} \Phi_{bright} \frac{1}{h\nu}$$

$$\text{Decay: } k_{on} + k_{off}^0 = I_{488} \sigma_{488} \Phi_{dark} \frac{1}{h\nu} + k_{off}^0$$

Figure 2.2 Photophysics of rsFastLime. (A) Schematic of rsFastLime photophysical states. (B) Fluorescence data for continuous-wave 488 nm laser and square-wave 405 nm laser. The fitting of growth and decay concludes the photophysical parameters  $k_{on}$ ,  $k_{off}$ , and  $k_{off}^0$ .

## 2.4.2 Epi-Fluorescence Microscope

Similar to Figure 2.1, the differences are expanded laser beam before a microscope (using 100-300 mm lens depending on the desired spot size) and a camera replacing an APD (Figure 2.3). A camera on a trinocular head is not suggested since additional mirrors in a trinocular head decrease photon collection efficiency relative to the side port. Defocusing of the collimated laser beam (1-4 mm diameter) is typically performed with a 100-300 mm focal length lens right before the beam enters the microscope. Shorter focal length lenses generate larger illumination area. For cell imaging, the illumination area is ~100 pixels in diameter (27  $\mu\text{m}$  wide, with 60x objective and a 16- $\mu\text{m}$  camera), and the

acquisition time varies from 2-200 ms, depending on the imaging area and fluorescence brightness in individual experiment.

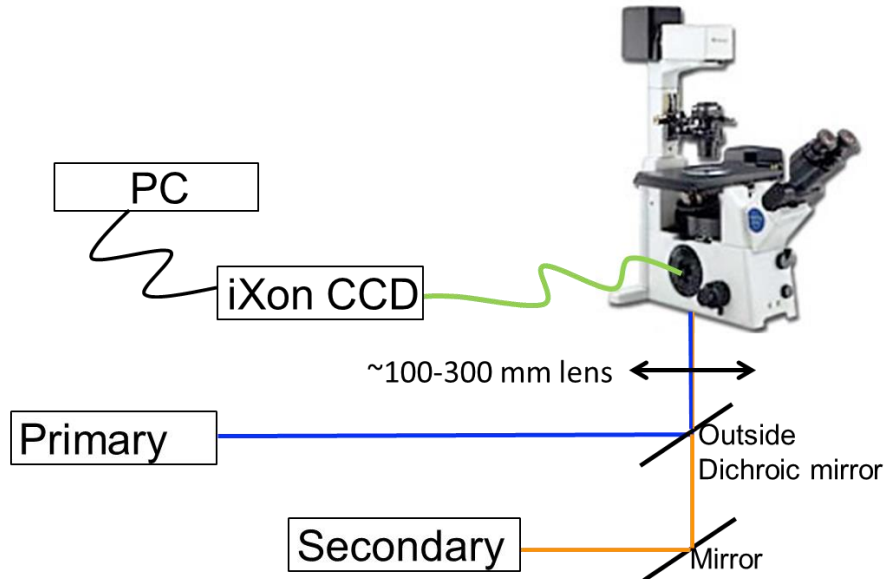


Figure 2.3 Setup for an epi-fluorescence microscope.

### 2.4.3 Spinning-Disk Confocal Microscope

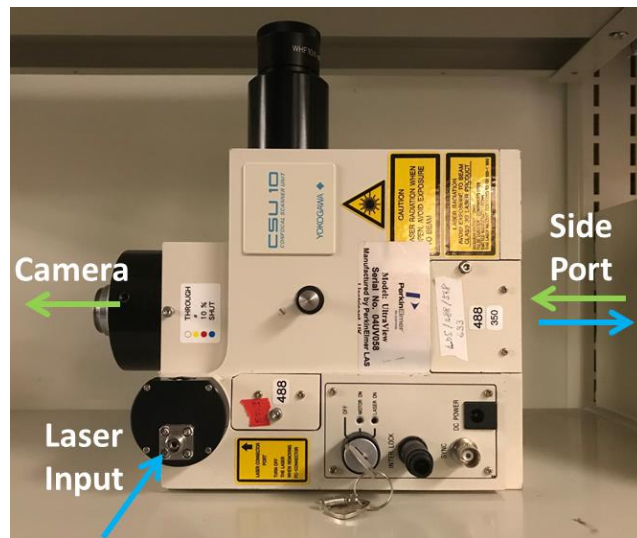


Figure 2.4 Spinning disk confocal unit, CSU 10, YOKOGAWA.

Spinning disk confocal unit, CSU 10, is usually placed on a microscope side-port. The laser used for excitation is fiber coupled, and the fiber is attached to the laser input

labeled in Figure 2.4. By using multiple micro-lenses, the CSU 10 can collect entire image sequences up to 360 frames per second. Similar to epi-fluorescence microscopy, the spinning disk confocal microscope illuminates the entire field of view, so the illumination intensity is less than  $100 \text{ W/cm}^2$ . This intensity limit is more suitable for modulating PS-FPs with shorter wavelength 2<sup>nd</sup> laser than FPs with longer wavelength 2<sup>nd</sup> laser than the wavelength of fluorescence, which requires intensity  $> 1 \text{ kW/cm}^2$ . Therefore, spinning disk confocal can only apply to DM-SAFIRE, designed for PS-FPs. In DM-SAFIRE experiments, I used 90-Hz camera frame rate for data acquisition for matching the spinning disk speed and modulation frequency (primary laser, 9 Hz; secondary laser, 2 Hz). Since the CSU 10 is a fixed speed spinning disk unit, the camera acquisition time should be  $n \cdot 1/360$  second for synchronization.<sup>157</sup> This limitation may affect some applications of SAFIRE discussed in chapter 4.

#### **2.4.4 Total Internal Reflection Fluorescence Microscope (TIRFM)**

To improve the signal-to-noise ratio for protein-protein interactions between supported bilayers and the cell surface, total internal reflection utilizes evanescent waves to illuminate only close to glass surface ( $\sim 200 \text{ nm}$ ). In the setup (Figure 2.5), I put a defocusing lens in front of the microscope. To find the back focal plane, I move the defocusing lens or change it until the laser after the objective is approximately collimated. After mounting the right lens at the right position, I will turn knob of the second to last mirror for changing the laser position to the side of the objective. After achieving TIRF, I can observe the reflective laser spot out from the objective and utilize TIRF-FCS for determining the penetration depth of evanescent wave,<sup>158-159</sup> which is generally 100-200

nm from FCS fittings. Higher NA objectives provide wider angle ranges for TIRF and easier alignment, so I use NA 1.45 oil objective (60x) for TIRF.

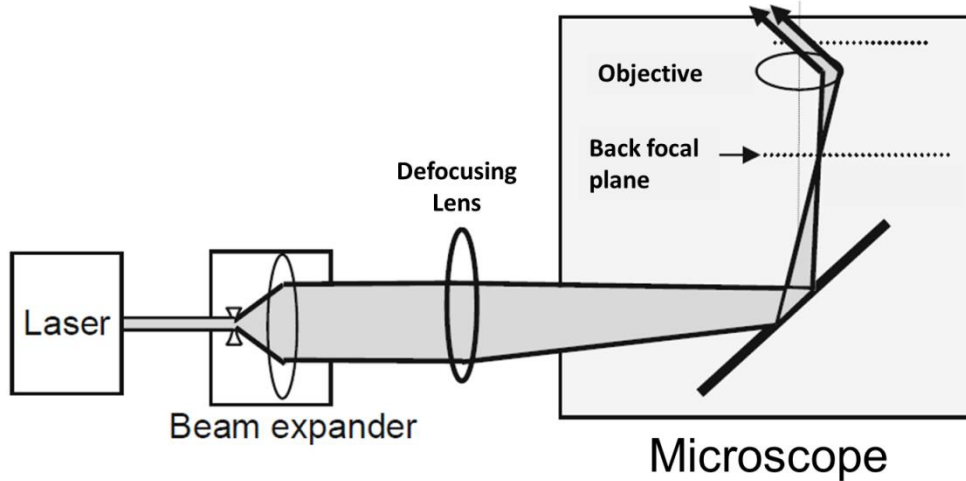


Figure 2.5 TIRFM setup.<sup>160</sup> Most of the back focal plane is inside an objective. Since the excitation laser is focused inside the objective, laser power should not exceed several mW. Adapted from Axelrod.<sup>160</sup>

#### 2.4.5 Live Cell Imaging

After the sample preparation mentioned in previous sections, I put the 35mm dish with living cells on a heated stage (Bioptechs Stable “Z” Specimen Warmer) to maintain a constant temperature of 37 °C. Without maintaining CO<sub>2</sub> and humidity supply, live cell experiments often last less than 2 hours with a heated stage. When cells are observed, NIH-3T3 mouse fibroblasts should be flat and widespread, and T cells should be circular without visible large cellular compartments under a light microscope. If mitochondria are targeted with FPs, mito-FPs should be worm-like, not punctate.

## 2.4.6 Fluorescence Correlation Spectroscopy & Fluorescence Cross-Correlation Spectroscopy (FCS, FCCS)

Fluorophore blinking or movement can be characterized by fluorescence correlation spectroscopy (FCS).<sup>132, 135, 143</sup> The correlation of fluorescence fluctuation provides the timescale of triplet states ( $\mu\text{s}$ ), diffusing time (solution 100  $\mu\text{s}$ -1 ms, bilayers  $\sim$ 100 ms), and binding events. Since the fluorescence fluctuation generates contrast in correlation curves, the contrast of signals decreases with increasing fluorophore concentrations. Typically one data acquisition volume can only contain 1-100 molecules, which are around 1-100 nM in diffraction-limited laser focus. In addition to the constraints in concentration, FCS requires fluorophores to be bright for monitoring each event. Usual photons per fluorophore per second are above 100, which typically require more than 100  $\text{W}/\text{cm}^2$  for laser excitation.

In this thesis, FCS often serves as a control experiment for confirming if the alignment is good. After aligning the side-port to the position of laser excitation by maximizing the fluorescence count rate, I record about one million photons which are from 5-20k photons per second (total time around 1 minute) for FCS correlation with the Becker & Hickl board. The output files (spc files) are correlated by a customized program (Teechart, Jung-Cheng Hsiang), and the correlation curve is fit based on a three dimensional model of FCS with triplet states.<sup>132, 135</sup> With known diffusion constants of standard organic dyes, I can calculate the diameter of a laser focus from the diffusion time extracted from FCS fitting. This control experiment not only confirms the laser focal spot size, but also the photons per molecule per second, which should be around 1k photons under 1  $\text{kW}/\text{cm}^2$ .

In order to capture binding events, fluorescence from two proteins, each labeled with different color dyes is monitored by separate detectors. While these two proteins are bound, the two fluctuation curves will share the same time trace thereby creating signals in the cross-correlation curves. Fluorescence cross-correlation spectroscopy (FCCS) monitors protein-protein interactions (PPIs), mentioned in chapter 1, by the degree of cross-correlation. Since FCCS requires two-color fluorescence time traces, I used two APDs for recording data (Figure 2.6).

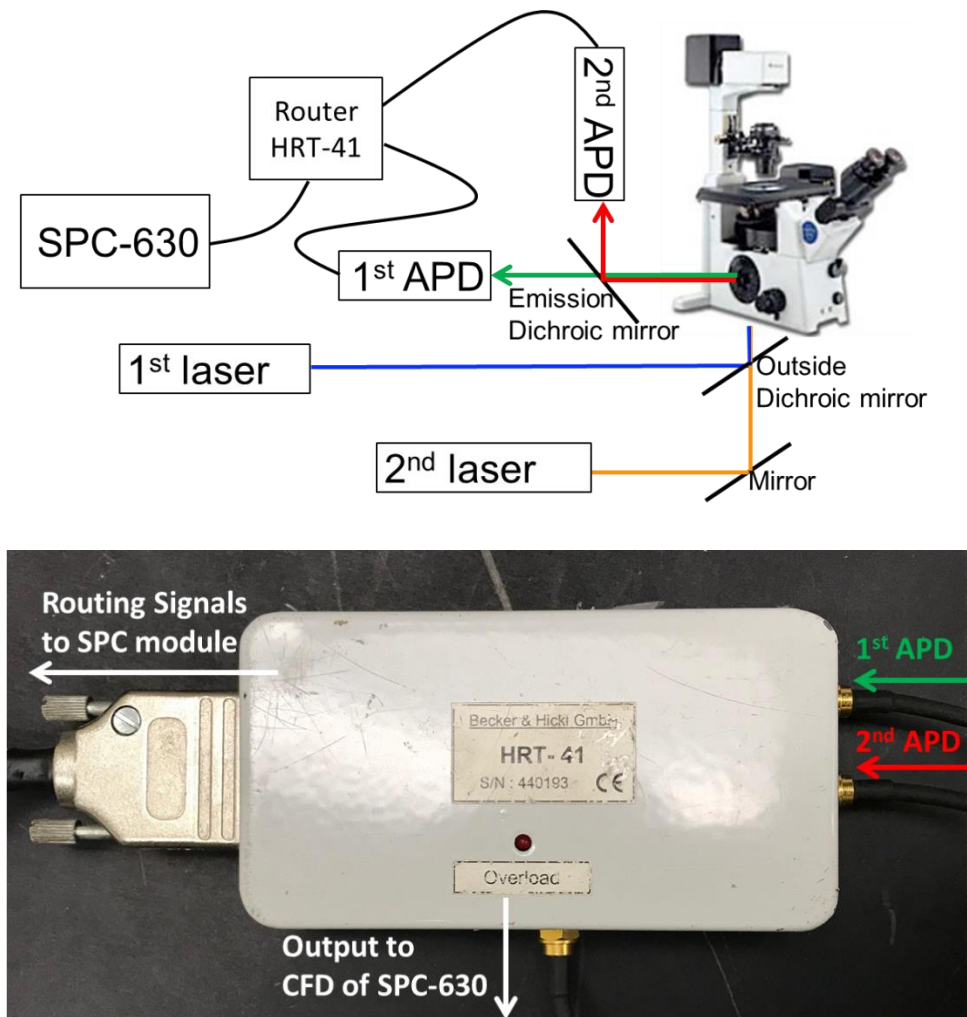


Figure 2.6 Setup for FCCS experiment. (Top) Alignment for FCCS single-point detection. (Bottom) Image of HRT-41 and how to connect two APDs and SPC-630.

To avoid the mixing signals of two APDs (crosstalk), I need to ensure that both detector signals have the same voltage and signal widths. In addition, the router is designed for PMT signals same as SPC-630, so the inverter and attenuator for APD are necessary in both channels. In this chapter, after the inverter and attenuator, two APDs showing ~400 mV and ~20 ns output, gave no crosstalk in the FCCS data acquisition. After the data acquisition, spc traces are cross-correlated by a customized program (Teechart, Jung-Cheng Hsiang), and cross-correlation curves are fitted in OriginLab.

#### **2.4.7 Image-Based Fluorescence Correlation Spectroscopy & Fluorescence Cross-Correlation Spectroscopy**

The sampling size of single-point detection is limited, so camera-based FCS and FCCS can monitor much larger areas at the expense of decreased time resolution. This approach is suitable for studying the slower dynamics (1 s-10 s) explored in this thesis.<sup>27,</sup>  
<sup>89</sup> Not only useful for visualizing dynamics in larger areas, cell images in bright field or epi-fluorescence can be simultaneously observed, making experiments easier to collect the interaction signals between specific peptide segments on major histocompatibility complex (pMHC) and T cell receptor (TCR), mentioned in appendix. To illuminate lipid bilayers, epi-fluorescence or TIRF yields similar results; TIRF is necessary for pMHC-bilayers and TCR on T cells since some free diffusing TFP would be background under wide-field illumination. For image-FCCS, I setup wide-field 633 nm laser illumination for imaging pMHC-Cy5 on bilayers and TIRF 451 nm laser illumination for imaging TFP attached to TCR complex. To collect both colors simultaneously, I align an emission splitting system (DC2 Photometrics, borrowed from the Zhu laboratory) to separate emission of Cy5 from TFP. Connecting two iXon EMCCDs (Model DV-887 and

DU-897D) (Figure 2.7), I match images of two camera by multi-emission beads (360/430 nm, 505/515 nm, 560/580 nm and 660/680 nm 0.2  $\mu\text{m}$  TetraSpeck™ microspheres, ThermoFisher) and also utilize a function generator to synchronously initiate the acquisition of the two cameras. The higher quantum efficiency camera (DU-897D) is used for the TFP channel.

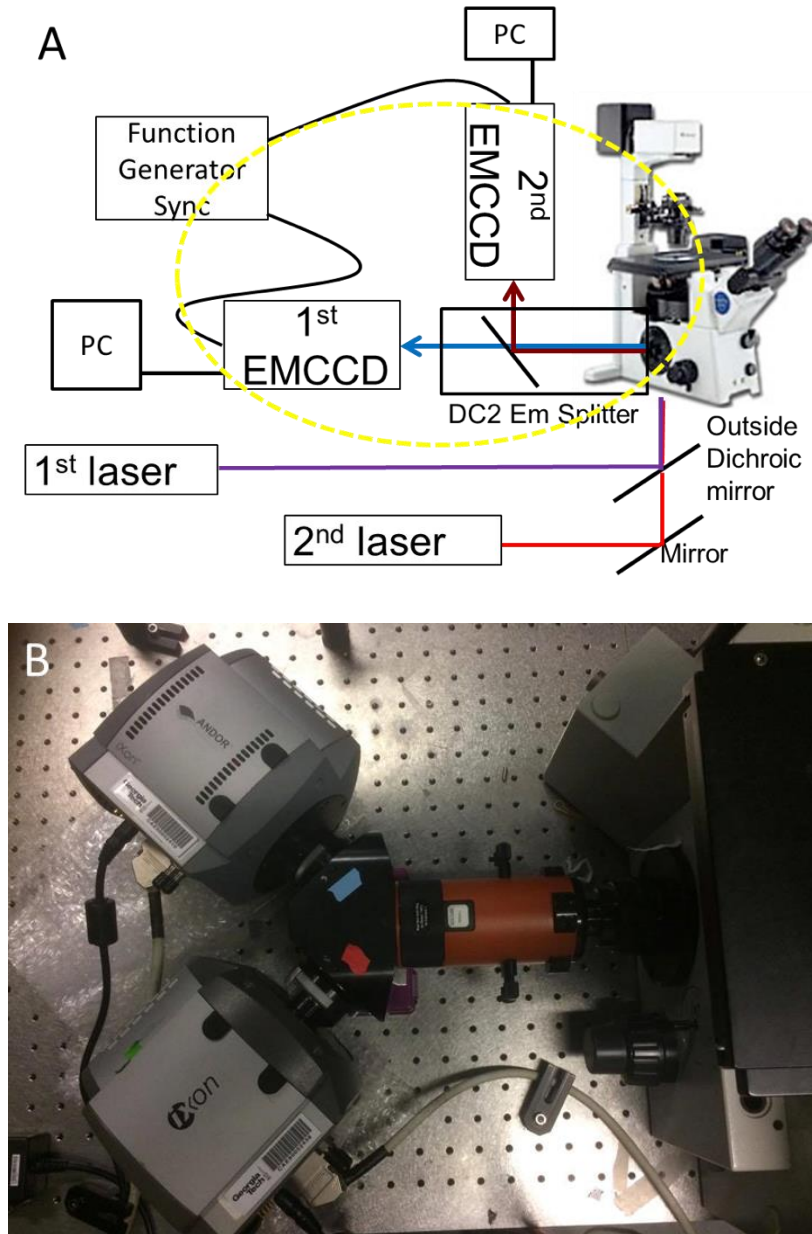


Figure 2.7 Setup for image-FCCS. (A) Optics alignment for image FCCS. The yellow circle is shown in photo (B).

After data acquisition, I use a developed program, ImFCS,<sup>149, 161</sup> (Figure 2.8) from the Wohland Laboratory<sup>5, 149-150, 161-162</sup> for analyzing image FCS/FCCS data. After the calculation of the point-spread-function of each pixel,<sup>150, 162</sup> I correlate or cross-correlate the frames within the entire image sequence. The acquisition area and time are 21\*21pixels, 2 ms for 50k frames, so the total imaging time is 100 seconds. Since the

acquisition time is more than a minute, photobleaching is usually observed. Individual photobleaching is mostly one-step reaction thereby assuming single-exponential.<sup>163</sup> Multiple bleaching events require multi-exponential fitting, but two exponential fitting is usually enough.<sup>163-164</sup> In order to correct the photobleaching, two-exponential correction was used in this experiment.<sup>163</sup>

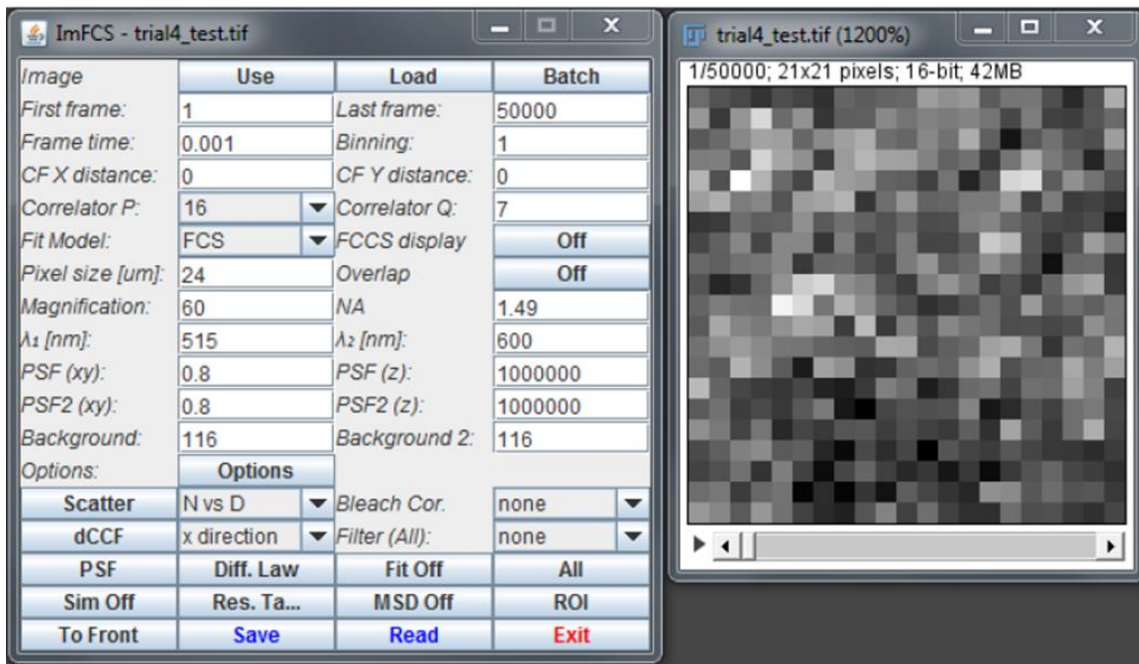


Figure 2.8 ImFCS<sup>149, 161</sup> in ImageJ/FIJI for image-FCS and FCCS experiments.

## 2.4.8 OPIOM-SAFIRe

Similar to wide-field illumination, two lasers are overlapped in the microscope for rsFastLime imaging. However, out-of-phase imaging after optical modulation (OPIOM) calculates the phase differences between fluorescence with dark states and excitation source. Similar to previous research, the excitation waveform is tracked by fluorescein since its fluorescence without obvious dark states immediately responds to the excitation.<sup>42</sup> However, the experimental result of fluorescein showed a long-lived dark state (~seconds) which requires additional correction.<sup>51</sup> In order to initiate the sine-wave

laser modulation the same everytime, I used a function generator to synchronize an EOM (controlled by ConOptics, 25A) for modulation and a CCD camera (DU-897D) to acquire data. Each modulation cycle was 10 timepoints per cycle and 10 cycles for one data point. For example, the acquisition time for 1 Hz modulation would be 10 Hz on camera, and total time is 10 s. By comparing fluorescein and rsFastLime, I can acquire out-of-phase signals by analyzing both time traces with MATLAB.<sup>51</sup>

## **2.5 Commercial Microscopes**

The control panels of commercial microscopes are similar, including Zeiss 710, Zeiss 780, PerkinElmer UltraVIEW VoX, and the GE Personal DeltaVision imaging system. Some constraints are described as follows. First, all the imaging systems can only change the setting of individual channels without continuous modulation of laser intensity. Therefore, commercial microscopes can only achieve square waves. Second, the data acquisition and laser illumination are tied altogether. Separation of each time scale is not available in the current systems. Third, laser intensity of each system is very different. Typically the laser power of commercial microscopes is 10-100 mW. In this case, single-point laser scanning confocal microscopes can easily achieve  $> 1 \text{ kW/cm}^2$ , while the maximum intensity of wide-field and spinning-disk confocal microscopes is  $\sim 100 \text{ W/cm}^2$ . Major differences of laser intensity from various microscopes should be considered for fluorophore and experimental design.

## CHAPTER 3 AUTOFLUORESCENCE SUPPRESSION AND SELECTIVE IMAGING

### 3.1 Introduction

The high biocompatibility and specificity of fluorescent proteins (FPs) allow for visualizing and understanding biological processes in living cells, tissues, and whole organisms. However, their detectability is often limited by moderate brightness and high autofluorescent background, either deteriorating the imaging contrast or producing false-positive signals.<sup>35, 165-167</sup> To avoid this problem, background reduction can be achieved by using red fluorescent proteins to minimize autofluorescence<sup>153</sup> or, more recently, by optically controlling emission intensity with photoswitchable or modulatable fluorophores.<sup>38-42, 49, 168-172</sup>

Minimizing the autofluorescent background by using red fluorescent proteins reduces the capability of multi-color imaging.<sup>114, 153</sup> Other possible solutions are lock-in detection, including frequency lock-in detection with nanoparticles developed by the Li Laboratory<sup>168-172</sup> or optical lock-in detection (OLID) developed by the Marriott Laboratory.<sup>38-41</sup> The imaging techniques optically control dark states of photoswitchable nanoparticles or photoswitchable fluorescent proteins (PS-FPs) for separating emission signals from autofluorescence. Since this thesis focus on *in vivo* imaging, PS-FPs are more ideal candidate than nanoparticles. After the introduction of OLID, this chapter provides the comparison between OLID and synchronously amplified fluorescence image recovery (SAFIRE) as well as further applications from SAFIRE.

### 3.1.1 Optical Lock-in Detection (OLID)

Since the observation of blinking behavior in FPs,<sup>61</sup> scientists have created several reversible PS-FPs<sup>99-100</sup> with optically controllable bright and dark states. Similar to the optically controllable nanoparticles,<sup>168-172</sup> the Marriott Laboratory optically controlled PS-FPs to avoid autofluorescence for better signal-to-background ratio. They imaged Dronpa with 488-nm laser excitation while turning it off and activated Dronpa with two-photon illumination (780 nm). This unique on-off mechanism only occurs in Dronpa, so correlation to a reference point helps to suppress non-modulatable autofluorescent background. The OLID formula is

$$\text{OLID value} = \sum_t \frac{(I(x,y,t) - \mu_I)(R(t) - \mu_R)}{\sigma_I \sigma_R}, \quad \text{Equation 3.1}$$

where  $I(x,y,t)$  is the detected fluorescence intensity at pixel  $(x,y)$  at time  $t$ ;  $R(t)$  is the reference point at time  $t$ .  $\mu_I$  and  $\mu_R$  are the mean values, while  $\sigma_I$  and  $\sigma_R$  are the standard deviation values of the fluorescence intensity at pixel  $(x,y)$  and reference point, respectively.<sup>38</sup>

One OLID image was taken for two on-off cycles, and each cycle was recorded five confocal images. The data showed up to 20-fold signal-to-background improvement (Figure 3.1).<sup>38, 40</sup> However, OLID has two disadvantages: (1) The value of correlation formula is not linear to concentration of Donpa. (2) Reference point should be autofluorescence-free, or the OLID value will be deteriorated. Therefore, SAFIRE provides a more robust and quantitative way for autofluorescence suppression as well as more applicable to wide-field imaging and selective imaging since SAFIRE does not require reference point and the magnitude of fast Fourier transform (FFT) is linear to the concentration of modulatable fluorophores.<sup>173</sup> Also, in the following sections I will

demonstrate dark state lifetime of PS-FPs as an additional parameter for discriminating diffusing vs. immobilized PS-FPs.

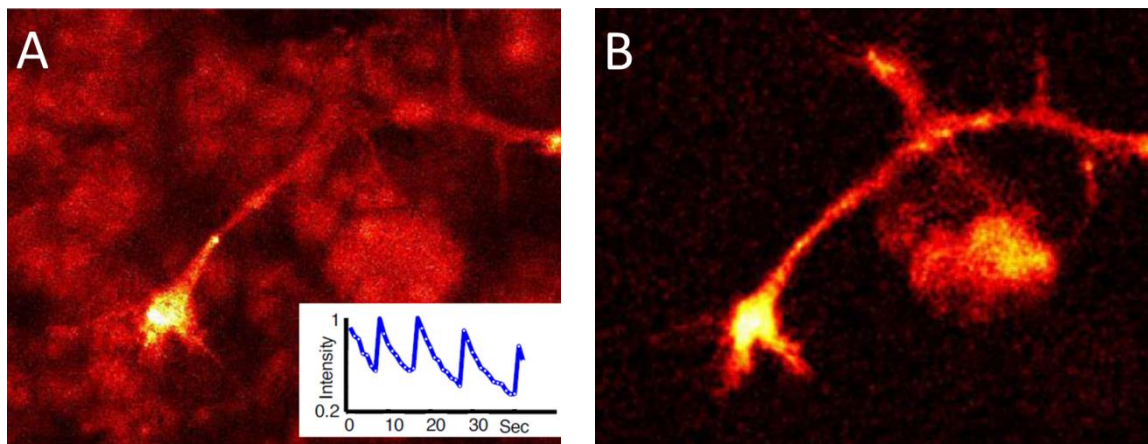


Figure 3.1 OLID image of Dronpa in *Xenopus* embryo. (A) Fluorescence image of Dronpa-actin within a motor neuron in a live *Xenopus* embryo. The inset shows the internal reference waveform from optically switching of Dronpa-actin. (B) Correlation image of Dronpa-actin from fluorescence image (A) with largely suppressed background. Adapted from Marriott.<sup>38</sup>

## 3.2 Autofluorescence Suppression

### 3.2.1 Single-Modulation SAFIRE (SM-SAFIRE)

To circumvent these limitations, our lab has developed SAFIRE, mentioned in section 1.7, which encodes external modulation waveforms only on the desired fluorophore signals.<sup>43-44, 173</sup> SAFIRE, therefore, eliminates the need for internal reference dyes and enables faster demodulated signal recovery. SAFIRE takes advantage of specific organic dyes,<sup>44, 46-47, 173</sup> inorganic emitters,<sup>43, 45, 173</sup> and FPs<sup>48-49, 173</sup> with optically accessible dark states that can be modulated through a dual-laser excitation scheme. While the primary laser excites all fluorescent molecules indiscriminately, a *longer* wavelength secondary laser regenerates fluorescence signals from the SAFIRE-enabled fluorophores by selectively depopulating their transient dark states. Only the fluorescence of interest follows the secondary laser at a specific frequency, while no background

fluorescence is induced by the *longer* wavelength secondary laser. After the Fourier transformation (FT), the intensity at the secondary laser modulation frequency recovers the fluorescence signals only from the FPs without non-modulatable autofluorescent background. Enhancement is the ratio of enhanced fluorescence amplitude with vs. without the secondary laser, which is a normalized to total primary-induced fluorescence and, therefore, independent of FPs concentration. This single-modulation SAFIRE (SM-SAFIRE) improves >5-fold signal-to-background contrast with modulatable modBFP-H148K by drastically reducing autofluorescence (Figure 3.2).<sup>49</sup>

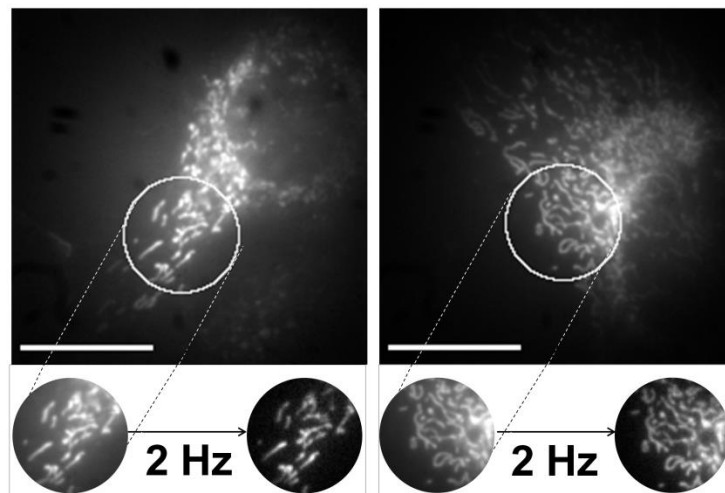


Figure 3.2 Demodulation of modBFP/H148K-mito in live cells. Demodulation at 2 Hz directly yields images with an average (left) 7-fold and (right) 3-fold improvement of signal to autofluorescent background. Intensity modulated, secondary laser (514 nm) illumination is performed only within the white circle. Scale bar is 20  $\mu$ m.

### 3.2.2 Dual-Modulation SAFIRE (DM-SAFIRE)

In addition to FPs, optically modulatable dark states of PS-FPs have been widely studied since the discovery of asFP595<sup>98</sup> and Dronpa.<sup>99</sup> The dark state of Dronpa was demonstrated as the trans chromophore by x-ray crystallography,<sup>103</sup> while the bright state is in the cis form. This long-lived dark state can be recovered by a secondary laser with wavelength *shorter* than that of the fluorescence back to the bright emissive manifold,

while optical controllable FPs are typically recovered by *longer* wavelength secondary illumination. Therefore, the recovery of the dark state by shorter wavelength secondary laser can induce autofluorescent background. Previously, OLID has manipulated the optically controllable dark state of Dronpa to suppress autofluorescence. However, the idea of correlation to a background-free internal reference may fail because of the autofluorescence accompanied from short wavelength excitation of Dronpa.

SM-SAFIRe from section 3.2.1 provides another way for autofluorescence suppression. The *longer* wavelength secondary laser recovers the fluorescence of optically modulatable FPs without inducing background. Similar to lock-in detection, fluorescence time traces of FP signals follow the modulated secondary laser intensity. Images with improved signal-to-background ratio are recovered through demodulation at the secondary laser frequency. Because PS-FP dark states are recovered by secondary illumination with shorter wavelength than that of the recovered fluorescence, secondary co-illumination induces additional background. Modifying single modulation SAFIRe (SM-SAFIRe) into dual modulation SAFIRe (DM-SAFIRe) avoids autofluorescence. Dronpa-V157G, rsFastLime, is single-mutation of Dronpa with a shorter dark state lifetime due to reduced hindrance of isomerization by V157G mutation. For rsFastLime, both primary laser (488 nm) and secondary laser (405 nm) excite the bright and dark states of PS-FPs, respectively. The autofluorescent background collected at 515 nm increases from both primary and secondary lasers. Modulation of primary laser at frequency  $x$  Hz and secondary laser at frequency  $y$  Hz for DM-SAFIRe causes PS-FPs to exhibit not only the signal at  $x$  and  $y$  Hz but also  $x+y$  and  $x-y$  Hz (side-band signals) from the dependency of both excitation (derivation at the end of this chapter). In contrast,

autofluorescent background only reacts with either the primary or secondary laser independently – no  $x+y$  or  $x-y$  Hz signals appear in frequency spectrum (Figure 3.3).

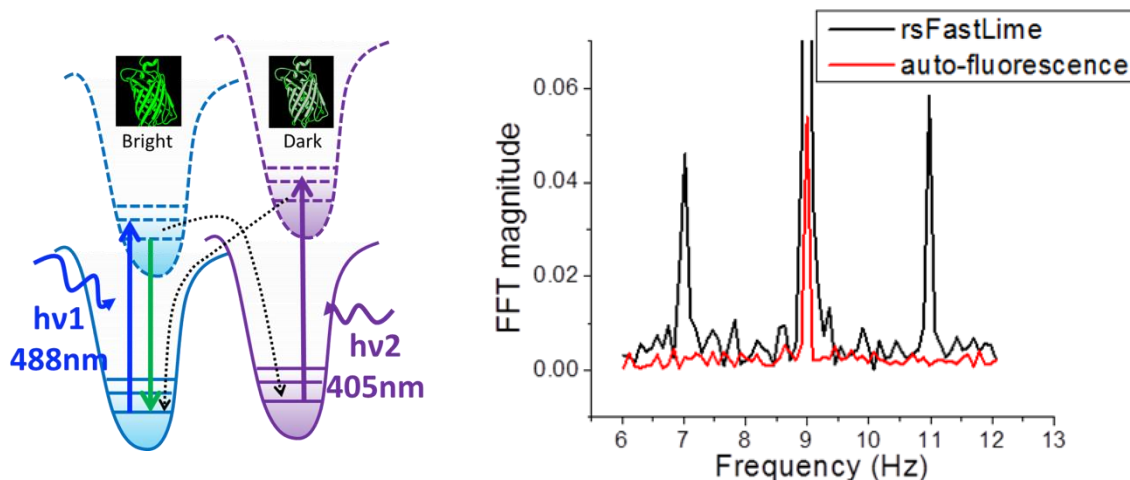


Figure 3.3 Bright and dark states of PS-FPs with dual modulation SAFIRE (DM-SAFIRE). (Left) Optical control of PS-FPs. Both 488 nm laser and 405 nm laser excite the bright and dark states of rsFastLime (Dronpa/V157G), respectively. (Right) Dual modulation enables background-free detection of rsFastLime. rsFastLime interacts dependently with both 405 and 488 nm lasers, while the autofluorescence is excited independently by each laser. The fast Fourier transform (FFT) shows that only rsFastLime presents side-band signals (9-2 and 9+2 Hz) when 488 nm is modulated at 9 Hz and 405 nm at 2 Hz.

After the demonstration of background-free signals on DM-SAFIRE, I employed both OLID and DM-SAFIRE with dual high-energy lasers using rsFastLime for autofluorescence suppression. In the OLID configuration, the 488 nm laser was not modulated and the 405 nm laser only illuminated the sample for 50 ms of each 1-second cycle, with the same acquisition rate and total imaging time (~5 s) as DM-SAFIRE. Although autofluorescent background is induced upon secondary laser illumination, OLID suppresses some autofluorescence from the correlation to internal background-free reference point. In contrast, only rsFastLime signals are shown at the sum and difference (side-bands) of the primary and secondary modulation frequencies of DM-SAFIRE

(derivation at the end of this chapter), completely excluding autofluorescent background from these sideband signals.<sup>50, 112</sup>

In live cell experiments, adherent NIH 3T3 mouse fibroblast cells are co-transfected with untargeted-EGFP and mitochondria-rsFastLime. Upon modulating 488 nm and 405 nm lasers at different frequencies (dual modulation, DM), I reconstructed the SAFIRE images from an image sequence by plotting the amplitude at each sum or difference of the two modulation frequencies. Secondary-only single modulation (SM) SAFIRE images were also recovered at the 405 nm laser modulation frequency. Both single and dual-laser modulation reveal the mitochondria devoid of EGFP background, but single-laser modulation shows higher autofluorescent background compared to DM (Figure 3.4A).

Compared to SAFIRE, OLID utilizes a slightly different excitation scheme involving cross-correlation of each pixel with a background-free reference signal that must be identified within each sample. To facilitate image recovery, OLID analysis was recently automated by using the brightest feature within an image sequence as the internal reference.<sup>40</sup> OLID reconstruction multiplies the contrast of each pixel intensity trajectory by that of the reference pixel trajectory; each is then normalized by its individual standard deviation of intensity values. OLID scales nonlinearly with the number of fluorophores at each position in the image thereby distorting the true contrast among emissive species. Further, in high background environments or if the position of the reference signal is not well-defined, OLID automation can select the wrong reference point, which drastically reduces imaging contrast (Figure 3.4B, OLID-1). Unlike OLID, SM- and DM-SAFIRE are linear with modulated fluorophore concentration and represent true fluorophore amounts without the introduction or selection of background-free internal reference.

As only the modulatable fluorophore responds, extracting the signals at the sum and differences of the primary and secondary modulation frequencies robustly recovers higher contrast images without manually selecting any internal reference points. In addition to imaging on a spinning disk confocal microscope (Figure 3.4), DM-SAFIRe demonstrates greater contrast improvement in wide-field imaging than does OLID (Figure 3.5). The potential of DM-SAFIRe for both confocal and wide-field microscopes allows for easier adaptation to various commercial microscopes, which will be mentioned in chapter 4.

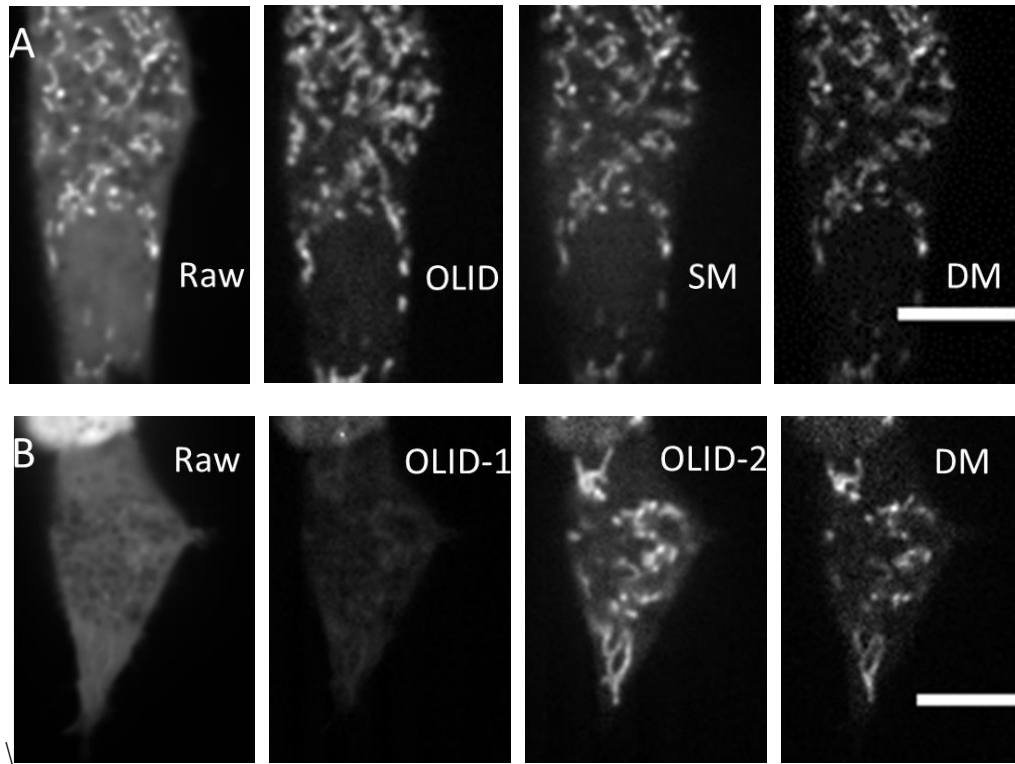


Figure 3.4 Comparison of single- and dual-modulation SAFIRE (SM, DM) vs. OLID in live NIH-3T3 cells co-expressing untargeted EGFP and mitochondria-targeted rsFastLime on a spinning disk confocal microscope. (A) (From left to right) Raw Image, Signal/Background~1.4; OLID, S/B~6; Demodulated image at 405nm frequency (SM-SAFIRE), S/B~5; Demodulation at the side-band frequencies (DM-SAFIRE), S/B~9. (B) Signal/background (S/B) comparison in the presence of bright EGFP background. (From left to right) Raw live cell image as in (A), S/B~1; OLID with automatic selection of brightest feature for reference waveform, S/B~1.6; OLID with manual selection of reference point, S/N~5; Demodulation image upon DM-SAFIRE, S/B~9. OLID with correct reference point and SM-SAFIRE give similar contrast improvements, while DM-SAFIRE show a further 2-fold improvement. Scale bars: 10  $\mu$ m.

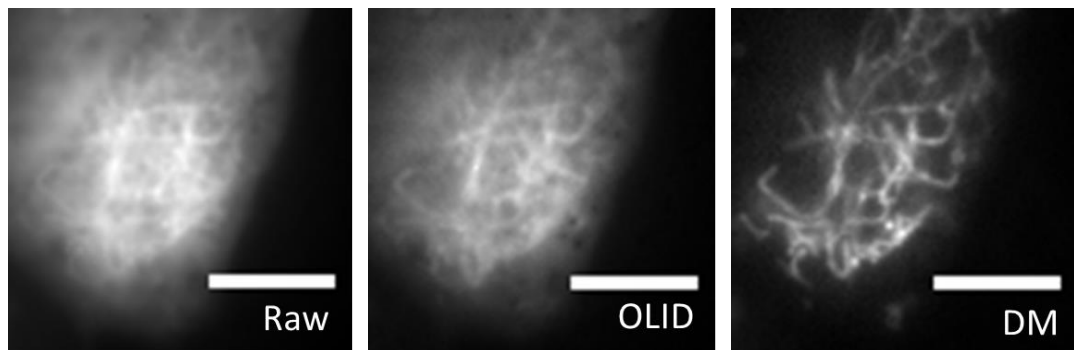


Figure 3.5 DM-SAFIRE improves the imaging contrast of NIH-3T3 cells co-expressing untargeted EGFP and mitochondria-targeted rsFastLime on a widefield microscope. (Left) Raw fluorescence image. (Middle) OLID. (Right) Demodulation image at the sum and difference of primary and secondary modulation frequencies (DM-SAFIRE). Scale bars: 10  $\mu$ m.

Similar to SAFIRE, OLID utilizes 2<sup>nd</sup> laser (405 nm) to regenerate the fluorescence of PS-FPs, and the only difference is correlation of images. Correlation requires reference waveform, but SAFIRE does not. In this case, OLID images can still be analyzed by Fourier transform of intensity of each pixel vs. time, regardless if imaging is done with 50% duty cycle in SM-SAFIRE/DM-SAFIRE or with much smaller duty cycle (<5%) in OLID. Current setup of OLID image is 50-ms 405 nm illumination per 1 second, similar to 5% duty cycle of 405 nm modulation. Applying our FT reconstruction methods (1 Hz demodulation) to OLID data yields SM-OLID (Figure 3.6) and significantly improves on standard OLID analysis signal contrast, while simultaneously providing a signal reconstruction that is linear in fluorophore brightness at each pixel. Signal improvement and linearity advantages would be achieved through SAFIRE-like Fourier analysis of both SAFIRE-acquired and OLID-type data.

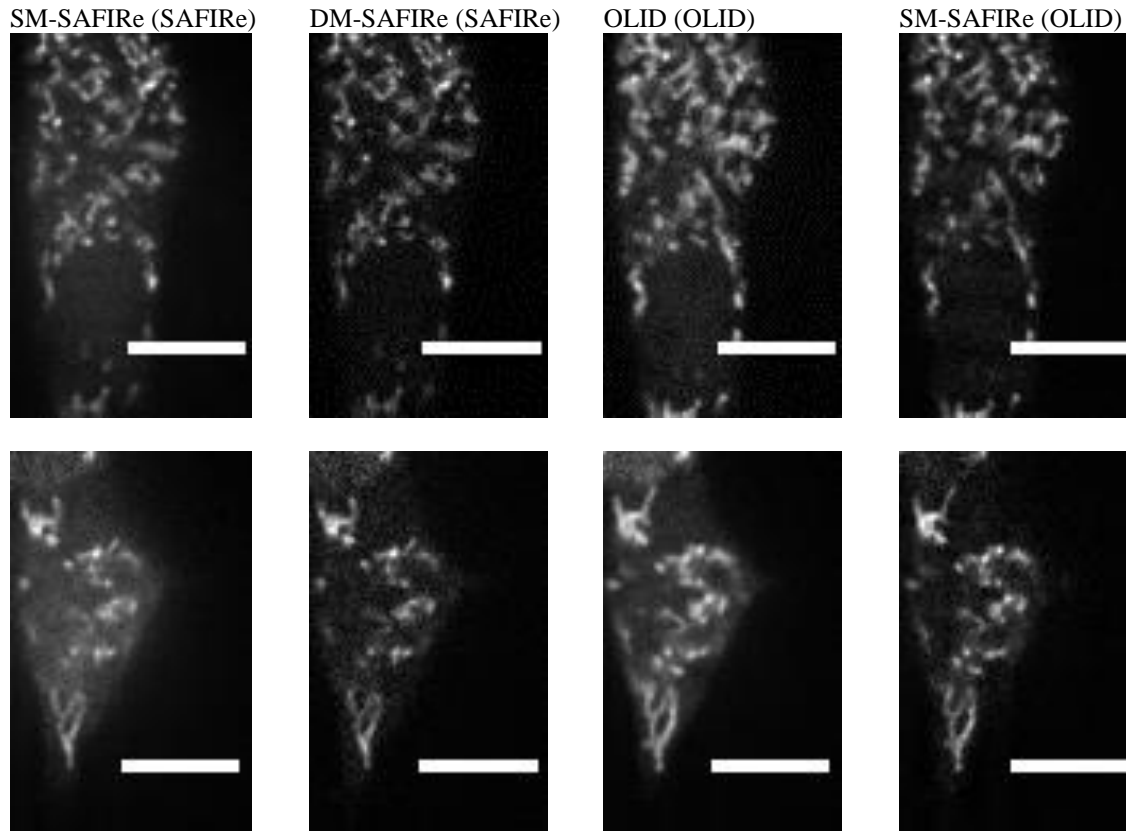


Figure 3.6 Comparison between SAFIRE and OLID in live NIH-3T3 cells co-transfected with untargeted EGFP and mitochondria-targeted rsFastLime. (From left to right) SM-SAFIRE Fourier analysis (SAFIRE setup), DM-SAFIRE Fourier analysis (SAFIRE setup), OLID analysis (OLID setup), and SM-SAFIRE Fourier analysis (OLID setup). SAFIRE modulation utilizes 50% duty cycle, while OLID utilizes 50 ms per 1 s of 405nm laser exposure (5% duty cycle). Thus, both OLID and SM-SAFIRE (SAFIRE) contain auto-fluorescence background from high-energy laser excitation, while OLID data acquisition generates less auto-fluorescence than does SM-SAFIRE because of shorter bursts of 405nm laser exposure. In contrast, DM-SAFIRE is background free. In general, Fourier analysis of the OLID data, however, shows better image contrast than possible with OLID analysis, and approaches similar imaging contrast generated by DM-SAFIRE, just without the further applications to selective image multiple proteins based on dark state lifetimes or diffusional transit rate, mentioned in following sections. Scale bars: 10  $\mu\text{m}$ .

### 3.3 Selective Imaging

Expanding from the discrimination of FPs with or without optically controllable dark states in previous sections, I quantified the lifetime of FPs and utilized it as an additional parameter for selective imaging. In this section, I selectively enhanced the rsFastLime signals with longer residence time within the laser focus and proposed a

spectral unmixing calculation based on the differences of dark state lifetimes. The utilization of dark state lifetime creates another dimension for discriminating FPs in addition to emission window, while preserving the ability to suppress all background fluorophore signals that do not have optically reversible dark states.

### 3.3.1 Characterizing the Dark State Lifetime of rsFastLime

A single mutation from Dronpa, rsFastLime (Dronpa-V157G) was created to have a shorter dark state lifetime which results from V157G mutation, drastically reducing the barrier for cis-trans isomerization in Dronpa. To fully utilize rsFastLime, I characterized  $k_{\text{on}}$  and  $k_{\text{off}}$  from the exponential fits of the fluorescence decays, which are the rates into ( $k_{\text{on}}$ ) and out of ( $k_{\text{off}}$ ) the dark state (Figure 3.7). Coupled with the known absorption cross section ( $\sigma_{488}$ ) for the bright state, the slopes of the decay and growth rates vs. primary excitation intensity (Fig. 3.5C) yielded a dark state quantum yield (from the bright to dark states) of  $\Phi_{\text{dark}} = 0.0035$ , while the intercept of growth rate vs. secondary excitation intensity (Fig. 3.5D) gives  $\sigma_{405} * \Phi_{\text{bright}} = 1.6 \times 10^{-18} \text{ cm}^2$ .  $\sigma_{405}$  is absorption cross section for the dark state, and  $\Phi_{\text{bright}}$  ( $\Phi_{\text{rev}}$ ) is the quantum yield from the dark to bright states. Thus, while still offering bright emission, the dark state quantum ( $\Phi_{\text{dark}}$ ) yield of rsFastLime is ~10 times larger than in Dronpa,<sup>174</sup> yielding faster photoswitching. Although the dark states of rsFastLime are much longer-lived than non-photoswitchable FPs, the forward and reverse photoisomerization rates can be accelerated by the primary and secondary laser illumination. The optically controllable dark states serve as an additional parameter for selective imaging. In the following sections, the dark state lifetimes allow for the discrimination of diffusing vs. immobilized molecules and spectral unmixing.

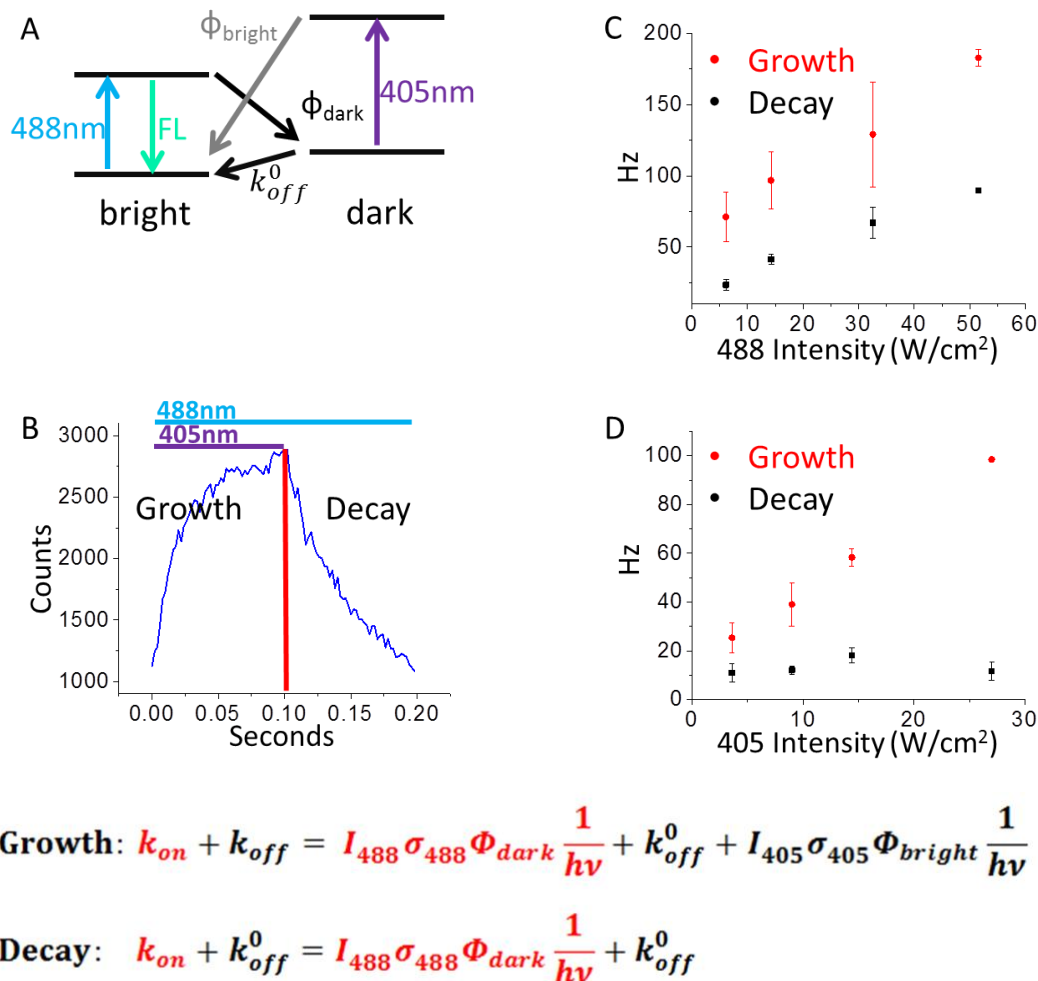


Figure 3.7 Photophysics of rsFastLime (Dronpa-V157G). (A) Schematic of transitions between the bright and the dark states with  $\sim 518$  nm fluorescence from 488nm excitation. Excitation at 405 nm depopulates the dark state and regenerates the bright manifold. (B) Continuous 488 nm and modulated 405 nm excitations yield fluorescence time traces showing exponential growth and decay. The growth is a function of 488 nm induced  $k_{\text{on}}$  ( $I_{488} \sigma_{488} \Phi_{\text{dark}} h^{-1} \nu_{488}^{-1}$ ), the thermal relaxation rate ( $k_{\text{off}}^0$ ), and the 405 nm induced dark state depopulation rate ( $I_{405} \sigma_{405} \Phi_{\text{bright}} h^{-1} \nu_{405}^{-1}$ ), while the decay is a similar function without the 405 nm induced rate. (C) Plotting the growth and decay rates vs the intensity at 488 nm yield the corresponding rate constants into (slope) and out of (intercept) the dark state. The 405 nm intensity is  $14.4 \text{ W}/\text{cm}^2$ . (D) The intercepts of (C) from various 405 nm laser intensities are linear in both growth and decay plots.

### 3.3.2 Diffusing vs. Immobilized rsFastLime

The ability to tune the modulation frequency of SAFIRE relative to  $k_{\text{on}}$  and  $k_{\text{off}}$  rates in PS-FPs (e.g. rsFastLime) affords new tools for protein discrimination, unavailable to other signal recovery schemes. The demodulated amplitude of SAFIRE depends on

photophysical parameters of rsFastLime. If the modulation frequency is faster than the dark state lifetime,

$$\tau_{\text{dark}} = k_{\text{dark}}^{-1} = (k_{\text{on}} + k_{\text{off}})^{-1},$$

the SAFIRE amplitude will be smaller because the full steady state populations cannot be established within any one modulation cycle. Similarly, fast diffusing rsFastLime is too transient to establish steady-state rsFastLime dark state population. Under the low 488 nm ( $< 10 \text{ W/cm}^2$ ) and 405 nm ( $\sim 4 \text{ W/cm}^2$ ) intensities, the timescale for the rsFastLime dark state is significantly longer than the diffusional transit time through a focused laser spot. Thus, diffusing molecules do not reside sufficiently long within the focal volume to generate either SM-SAFIRE or DM-SAFIRE signals (Figure 3.8). While SM-SAFIRE generates autofluorescent background from high-energy secondary excitation, DM-SAFIRE shows neither autofluorescent background nor signals of diffusing rsFastLime molecules. The estimated diffusion time for proteins is  $\sim 10$  ms (laser spot radius:  $0.67 \mu\text{m}$ ), which is significantly shorter than the dark state lifetime ( $\sim 33$  ms at  $7 \text{ W/cm}^2$  488 nm and  $3 \text{ W/cm}^2$  405 nm, Figure 3.6). Hence, the diffusion time dependent SAFIRE signals allows for distinguishing immobilized vs. diffusing rsFastLime while simultaneously suppressing non-modulatable background. In this case, the FT amplitude includes modulatable ratio as well as concentration of rsFastLime, which depends on protein expression level. Therefore, DM-SAFIRE side-band signals are divided by the FT amplitude at the primary laser (488 nm) modulation frequency for normalization, so the ratio (enhancement) of modulatable molecules to all 488-nm-induced fluorescence is comparable across live cells in DM-SAFIRE.

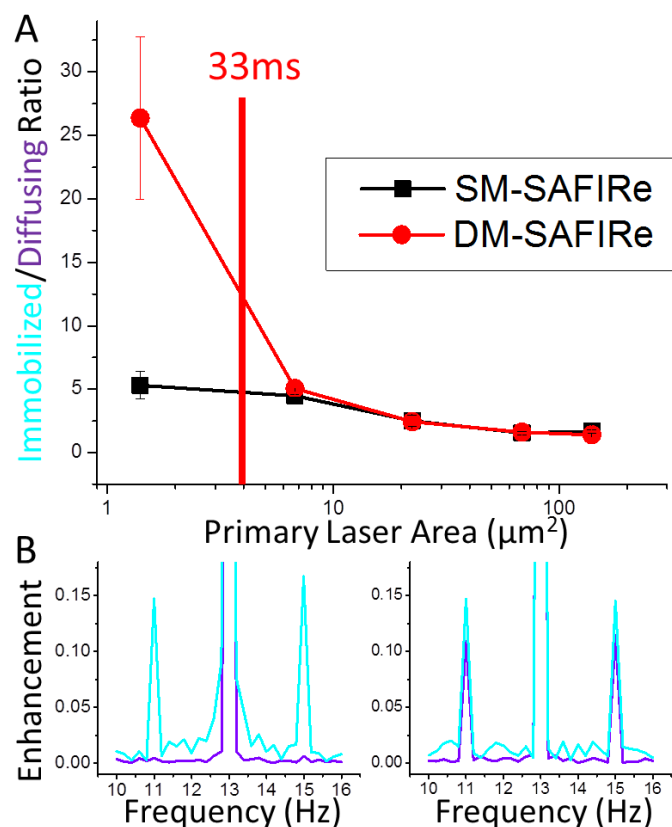


Figure 3.8 Contrast between immobilized mito-rsFastLime vs. diffusing untargeted-rsFastLime with varying excitation area. (A) Increasing laser spot size increases the diffusion time of untargeted-rsFastLime, allowing diffusing rsFastLime to be modulated (488 nm at 7 W/cm<sup>2</sup> and 405 nm at 3 W/cm<sup>2</sup>). Thus, the ratio of immobilized to diffusing molecules approaches unity in dual-modulation (DM) and single-modulation (SM). Because of autofluorescent background, the ratio in SM (~5) is much smaller than that achieved with DM (~25) in small excitation area. The major change is when the diffusional transit time of untargeted-rsFastLime increases beyond the 33 ms photophysical timescale. (B) Left: The DM-SAFIRE enhancement of immobilized (blue) and diffusing (purple) rsFastLime within the 1.4-μm<sup>2</sup> excitation area. Right: The same DM-SAFIRE enhancement within a 140-μm<sup>2</sup> excitation area. All FT signals were normalized by the amplitude at the 488 nm modulation frequency (13 Hz) for concentration-independent comparison.

The ratio of enhancement from localized mito-rsFastLime vs. that from freely diffusing rsFastLime reaches unity in large excitation volumes, when diffusion rates are slow relative to photophysical rates. This idea allows for the different modulation responses of bound and unbound molecules for selective visualization of immobilized rsFastLime, with potentially >25-fold selectivity over diffusing, but otherwise identical rsFastLime. After the demonstration between SAFIRE enhancement and spot size,

mitochondria-localized rsFastLime is selectively imaged over untargeted rsFastLime in live cells, co-expressing two forms of the same PS-FP (Figure 3.9). With few- $\mu\text{m}$  spot diameters, dual modulation readily increased the signal of molecules residing longer within the laser focal volume. This signal enhancement from longer residence time may have potential to enhance signals of binding molecules but ignore unbound diffusing molecules. While overwhelming unbound signals in FCS, FRAP, and FRET are the problem for the detection of weak PPIs, demonstration of >25-fold signal differences between immobilized vs. diffusing proteins in DM-SAFIRE provides a potential way to improve the detection limit of PPIs *in vivo*.

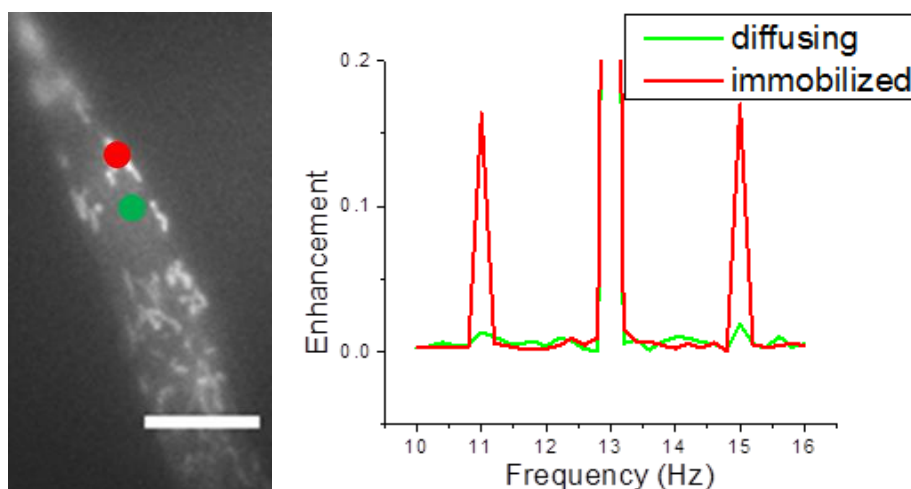


Figure 3.9 Diffusing vs. immobilized rsFastLime in cells co-expressing mito-rsFastLime and untargeted-rsFastLime. The ratio of sideband enhancement between the immobilized and diffusing molecules is  $\sim 10$ . 488 nm is  $8.8 \text{ W/cm}^2$  modulated at 13 Hz, and 405 nm is  $2.4 \text{ W/cm}^2$  modulated at 2 Hz. Scale bar:  $10 \mu\text{m}$ .

### 3.3.3 Spectral Unmixing

In addition to different residence times for otherwise identical fluorophores, individual photophysical dark state lifetimes from different fluorophores create an additional dimension for discriminating FPs, while retaining the original autofluorescence

suppression ability. For example, Dronpa-V157G (rsFastLime) and Dronpa-M159T (Dronpa2) have inseparable emission spectra, but have significantly different dark state lifetimes (Figure 3.10A). The different responses of enhancement vs. time allow for discrimination of the molecules based on dark state lifetimes (from sub- $\mu$ s to minutes),<sup>45-46, 48-50, 100, 175</sup> which is much broader than emission spectra (400-700 nm) or fluorescence lifetimes (1-20 ns) from general fluorophores applied to biological imaging.<sup>176</sup> After acquiring data of enhancement vs. modulation frequency (a modulation spectrum), the enhancements (X and Y) from individual purified FPs can be utilized as reference points. In mixed FPs, the enhancement (Z) at certain frequency p Hz and q Hz is a mixture (concentration A and B) of the enhancements,

$$Z_{p \text{ Hz}} = A * X_{p \text{ Hz}} + B * Y_{p \text{ Hz}}$$

$$Z_{q \text{ Hz}} = A * X_{q \text{ Hz}} + B * Y_{q \text{ Hz}}.$$

After solving these equations, the contributions of concentration A and B will be separated. Based on Monte Carlo simulation, two FPs with 3-fold differences in  $k_{\text{on}}$  ( $1/\tau_{\text{on}}$ ) can be unmixed by the calculation (Figure 3.10B). Following the same idea, rsFastLime and Dronpa2 are candidates for spectral unmixing; also, Baijie Peng in our group has initiated a mutation study of EYFP to create multiple FPs with indistinguishable emission spectra but different dark state lifetimes in collaboration with the Fahrni group. Photophysical characteristics of FPs can not only suppress non-modulatable background but also expand dye selection spectra and multicolor imaging capacity.

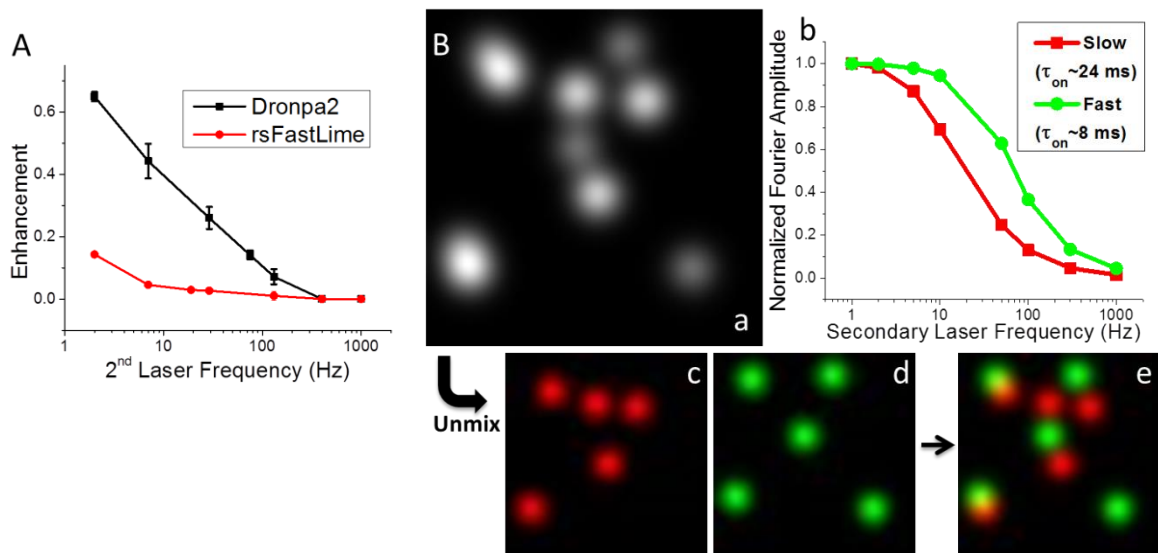


Figure 3.10 Spectral unmixing based on modulation spectra. (A) Same-color Dronpa2 and rsFastLime show significant different enhancement vs. modulation frequency based on different dark state lifetimes. (B) Monte Carlo simulation of modulation spectral unmixing to separate identically emitting fluorophores by different frequency responses. a) Total image of two sets of spatially overlap fluorescent signals. Entire image is modulated by secondary laser at 10Hz and 100Hz. b) Modulation spectra of molecules with fast ( $\tau_{on} \sim 8$  ms, green) and slow ( $\tau_{on} \sim 24$  ms, red) photophysical parameters (both  $\tau_{off} \sim 8$  ms). c) Slow and d) Fast molecule positions recovered from spectral unmixing by utilizing Fourier amplitudes from 10Hz and 100Hz at each pixel and the modulation spectra in b. e) composite image showing recovered fast (green) and slow (red) molecule positions.

### 3.4 Conclusion

The utilization of photophysical dark states creates another dimension for advancing fluorescence microscopy. Here, PS-FPs with well-characterized dark states demonstrate autofluorescence suppression and selective imaging, including the enhancement of immobilized molecules and spectral unmixing. SAFIRE techniques show linear imaging contrast improvement with external laser modulation on both confocal and wide-field microscopes, while OLID requires internal background-free reference points for nonlinear image recovery, only possible on confocal microscopes. By matching the photophysical parameters, the long-lived dark state of rsFastLime shows modulation signals only from immobilized or slowly diffusing rsFastLime. This application offers

great potential for discriminating fluorophores of interest from otherwise identical FPs yet overwhelming background in live cell imaging, while simultaneously creating new potentials for studying weak PPIs within live cells. In addition to comparing to diffusion time, the photophysical parameters serve as another axis for multiplexed imaging. The simulation demonstrates the frequency response of different FPs can be utilized for spectral unmixing, while preserving the ability to suppress autofluorescence and improve overall imaging sensitivity and contrast.

**Supporting Information: Photophysical Response of FPs and PS-FPs with  
SM-SAFIRE and DM-SAFIRE**

Upon long-wavelength 2<sup>nd</sup> illumination, the fraction of fluorescent molecules residing in the dark state is optically pumped back to the emissive manifold without the generation of autofluorescence. The modulation frequency of fluorescence intensity is the same as 2<sup>nd</sup> laser frequency since the ground state fraction is modulated by external modulation of 2<sup>nd</sup> laser intensity. Recovering signal that is shifted to this modulation frequency significantly improves fluorophore visibility *in vitro* and *in vivo* by excluding non-modulatable autofluorescence. However, PS-FPs require short-wavelength 2<sup>nd</sup> laser to recover the dark states. Thus, modulating only the 2<sup>nd</sup> excitation at 405 nm will generate additional autofluorescence in the >500 nm detection channel. As PS-FPs modulation requires absorption of both 1<sup>st</sup> and 2<sup>nd</sup> lasers to modify the ground state (emissive) population, simultaneous modulation of primary and secondary lasers should isolate signals from PS-FPs at the sum ( $\nu_p + \nu_s$ ) and difference ( $\nu_p - \nu_s$ ) of primary and secondary laser modulation frequencies. The total fluorescence intensity,  $I_F$ , is

$$I_F(t) = N_{tot} I_{prim}(t) \sigma \Phi_F f_{GS}(t)$$

in which  $I_{\text{prim}}(t)$  is the primary laser excitation intensity,  $N_{\text{tot}}$  is the total number of molecules being excited,  $\sigma$  is the absorption cross section,  $\Phi_{\text{F}}$  is the fluorescence quantum yield, and  $f_{\text{GS}}(t)$  is the time dependent fraction of molecules in the ground state. For SM-SAFIRE,  $I_{\text{prim}}(t)$  is constant, while the secondary laser modulates  $f_{\text{GS}}(t)$ . The steady-state ground state population is given by the rate out of the dark state,  $k_{\text{off}}$ , divided by the sum of rates into ( $k_{\text{on}}$ ) and out of ( $k_{\text{off}}$ ) the dark state. Modulating the secondary laser intensity, such that

$$I_{\text{sec}}(t) = \frac{I_{\text{sec}}^{\text{max}}}{(1+A)} \left(1 + A \cos(2\pi\nu_{\text{mod}}^{\text{sec}} t)\right)$$

giving the secondary laser-induced modulated ground state fraction:

$$f_{\text{GS}}(t) = \frac{k_{\text{off}}}{k_{\text{on}} + k_{\text{off}}} = \frac{k_{\text{off}}^0 + \frac{I_{\text{sec}}^{\text{max}} \sigma_{\text{off}} \Phi_{\text{bright}} \lambda}{hc(1+A)} \left(1 + A \cos(2\pi\nu_{\text{mod}}^{\text{sec}} t)\right)}{I_{\text{prim}} \sigma \Phi_{\text{dark}} \frac{\lambda}{hc} + k_{\text{off}}^0 + \frac{I_{\text{sec}}^{\text{max}} \sigma_{\text{off}} \Phi_{\text{bright}} \lambda}{hc(1+A)} \left(1 + A \cos(2\pi\nu_{\text{mod}}^{\text{sec}} t)\right)}$$

When the rate into the dark state is much faster than that out of the dark state, we can remove the cosinusoidal term from the denominator, giving:

$$\begin{aligned} f_{\text{GS}}(t) &\approx \frac{k_{\text{off}}^0 + \frac{I_{\text{sec}}^{\text{max}} \sigma_{\text{off}} \Phi_{\text{bright}} \lambda}{hc(1+A)} \left(1 + A \cos(2\pi\nu_{\text{mod}}^{\text{sec}} t)\right)}{I_{\text{prim}} \sigma \Phi_{\text{dark}} \frac{\lambda}{hc} + k_{\text{off}}^0} \\ &= \frac{k_{\text{off}}^0}{k_{\text{on}} + k_{\text{off}}^0} + \frac{I_{\text{sec}}^{\text{max}} \sigma_{\text{off}} \Phi_{\text{bright}} \lambda}{(k_{\text{on}} + k_{\text{off}}^0) hc(1+A)} \left(1 + A \cos(2\pi\nu_{\text{mod}}^{\text{sec}} t)\right) \end{aligned}$$

For the intensities used in imaging rsFastLime,  $k_{\text{on}}$  is  $\sim 10$ -fold faster than the secondary laser induced cosinusoidal term, satisfying the conditions giving the cosinusoidal dependence of the ground state fraction. Substituting in the modulated ground state population into the equation for SM-SAFIRE fluorescence intensity gives:

$$I_F^{SM}(t) = N_{tot} I_{prim} \sigma \Phi_F \frac{\lambda}{hc} \left( \frac{k_{off}^0}{k_{on} + k_{off}^0} + \frac{I_{sec}^{max} \sigma_{off} \Phi_{bright} \lambda}{(k_{on} + k_{off}^0) hc(1+A)} \left( 1 + ACos(2\pi\nu_{mod}^{sec} t) \right) \right)$$

Because PS-FPs such as rsFastLime operate with primary and secondary lasers which are higher energy than that of the collected fluorescence, both excitation wavelengths generate significant fluorescence in the emission channel. As only the PS-FPs emission will depend on both primary and secondary intensities, we utilize DM-SAFIRE to improve imaging contrast and recover only signals from rsFastLime. Starting with the formula of SM-SAFIRE above, the primary laser is also modulated at its own modulation frequency and modulation depth of B/(1+B). This gives the DM-SAFIRE fluorescence intensity as:

$$I_F^{DM}(t) = \frac{N_{tot} I_{prim}^{max} \sigma \Phi_F \lambda}{hc(1+B)} \left( 1 + BCos(2\pi\nu_{mod}^{prim} t) \right) \left( \frac{k_{off}^0}{k_{on} + k_{off}^0} + \frac{I_{sec}^{max} \sigma_{off} \Phi_{bright} \lambda}{(k_{on} + k_{off}^0) hc(1+A)} \left( 1 + ACos(2\pi\nu_{mod}^{sec} t) \right) \right)$$

Expanding this expression, one gets:

$$I_F^{DM}(t) = \frac{N_{tot} I_{prim}^{max} \sigma \Phi_F \lambda}{hc(1+B)} \left[ \left( \frac{k_{off}^0}{k_{on} + k_{off}^0} + \frac{I_{sec}^{max} \sigma_{off} \Phi_{bright} \lambda}{(k_{on} + k_{off}^0) hc(1+A)} \right) \left( 1 + BCos(2\pi\nu_{mod}^{prim} t) \right) + \frac{I_{sec}^{max} \sigma_{off} \Phi_{bright} \lambda A}{(k_{on} + k_{off}^0) hc(1+A)} Cos(2\pi\nu_{mod}^{sec} t) + \frac{I_{sec}^{max} \sigma_{off} \Phi_{bright} \lambda AB}{(k_{on} + k_{off}^0) hc(1+A)} Cos(2\pi\nu_{mod}^{prim} t) Cos(2\pi\nu_{mod}^{sec} t) \right]$$

Using the trigonometric identities (product-to-sum formulas):

$$Cos(2\pi\nu_{mod}^{prim} t) Cos(2\pi\nu_{mod}^{sec} t) = \frac{1}{2} \left( Cos(2\pi(\nu_{mod}^{prim} + \nu_{mod}^{sec}) t) + Cos(2\pi(\nu_{mod}^{prim} - \nu_{mod}^{sec}) t) \right)$$

One sees that frequency components at zero frequency, the primary laser modulation frequency, the secondary laser modulation frequency, and both the sum and difference of the primary and secondary modulation frequencies become observable:

$$I_F^{DM}(t) = \frac{N_{tot} I_{prim}^{max} \sigma \Phi_F \lambda}{hc(1+B)} \left[ \left( \frac{k_{off}^0}{k_{on} + k_{off}^0} + \frac{I_{sec}^{max} \sigma_{off} \Phi_{bright} \lambda}{(k_{on} + k_{off}^0) hc(1+A)} \right) (1 + B \cos(2\pi \nu_{mod}^{prim} t)) + \right. \\ \left. \frac{I_{sec}^{max} \sigma_{off} \Phi_{bright} \lambda A}{(k_{on} + k_{off}^0) hc(1+A)} \cos(2\pi \nu_{mod}^{sec} t) + \frac{I_{sec}^{max} \sigma_{off} \Phi_{bright} \lambda AB}{2(k_{on} + k_{off}^0) hc(1+A)} \left( \cos(2\pi(\nu_{mod}^{prim} + \nu_{mod}^{sec}) t) + \cos(2\pi(\nu_{mod}^{prim} - \nu_{mod}^{sec}) t) \right) \right]$$

Importantly, 405-nm excited signal and background appear at the secondary modulation frequency, 488nm excited signal and background appear at the primary modulation frequency, unmodulated signals appear at zero frequency, but only molecules with fluorescence affected by both primary and secondary lasers will appear at the sum and difference of the two modulation frequencies. This gives pure rsFastLime signals at the sum and difference frequencies without being obscured by unmodulatable background. However, signals at sum and difference frequencies are only the partial response of PS-FPs, so the enhancement from DM-SAFIRE is not the same as SM-SAFIRE.

The above derivation assumes that the system responds at sufficiently low modulation frequency. At higher frequencies, the modulation depth decreases, as the molecules cannot respond sufficiently fast to fully establish steady-state populations, similar to SM-SAFIRE. Furthermore, when  $k_{on}$  is comparable to  $k_{off}$ , the sinusoidal dependence of the ground state population gets somewhat distorted. The primary frequency components still correspond to the same frequencies derived above for both

SM-SAFIRE and DM-SAFIRE, making these methods applicable to any modulation frequency and relative intensities.

## CHAPTER 4 SAFIRE ON COMMERCIAL MICROSCOPES

After the invention of confocal microscopy and the advances in devices including light sources and detectors, commercial confocal microscopy has become a standard method for fluorescence imaging in biology. From basic research to diagnostics, routine utilization of confocal microscopy allows the visualization of fluorophore-targeted organelles, immunostaining of specific proteins, or particle tracking. However, the advancement of fluorescence microscopy always starts from customized microscopes in a specialized laboratory. Labor-intensive, complicated theory and optical alignment hinder the wide utilization of most advanced microscopes by general biological groups; the transition from customized microscopes to commercial microscopes usually takes several years after the publication of new techniques (discussion in *Frontiers in Imaging Science*, Janelia Farm 2017). For example, the first stimulated emission depletion (STED) experiment was published in 2000,<sup>75</sup> but the first commercially available STED microscope was available in 2007.<sup>177</sup> In addition, one commercial microscope is too expensive to be replaced whenever a newer model is developed. Therefore, even if more advanced microscopies are available, most biologists still utilize older microscopy techniques.

Because of the long lag time before commercial availability and high cost of commercial microscopy, adaptation of SAFIRE to currently available commercial microscopes without additional cost will positively impact a wide array of biological studies. In this chapter, autofluorescence suppression from SAFIRE is the key feature applied to commercial microscopes, including a confocal laser scanning microscope (CLSM, Zeiss), a spinning disk confocal microscope (SDCM, PerkinElmer), and a

wide-field microscope (GE). This demonstration of autofluorescence suppression on commercial microscopes has enabled the Melikyan Laboratory to study the cell entry of HIV-1 viruses by tracking fluorescent proteins (FPs) labeled virus-like particles (VLPs).

#### **4.1 Introduction**

Visualizing FP-targeted molecules in biological samples serves as a standard procedure for research or diagnostics. However, fluorescent species other than FPs in complex biological environment often overlap with FP fluorescence, obscuring signals of interest. This plagues the imaging quality of fluorescence microscopy, either lowering signal-to-background contrast or even generating false-positive fluorescent signals. For example, many cellular metabolites exhibit blue and green fluorescence, including flavins and NAD(P)H.<sup>35, 165</sup> Using red FPs can avoid blue and green autofluorescence, but it limits the choices for multi-color imaging and some cell lines still show obvious red autofluorescence (discussion with Greg Melikyan in Emory). Therefore, removal of autofluorescence is a significant issue in fluorescence microscopy.

Several fluorescence methods address autofluorescence avoidance. Because the combination of autofluorescence species shows broad emission spectra compared to narrow fluorescence spectrum of FPs, multiple fluorescence wavelength collection channels are utilized for spectrally unmixing to remove background signals based on known FP and autofluorescence spectra.<sup>167</sup> However, this method requires that scientists understand the autofluorescent spectrum of tested samples, which can be difficult for tissue slices with unknown autofluorescence from animals or patients. Another challenge results from the different chemical reagents used for cell fixation, as some chemicals may induce more autofluorescence, while some chemicals may reduce brightness of FPs.<sup>165</sup>

Also, the optimization of fixation process cannot solve the autofluorescence in live cell or tissue imaging. Some other methods require pretreatment including autofluorescence photobleaching<sup>166</sup> or different ways to collect data, e.g. fluorescence collection at longer lifetime (~10 ns) after pulsed laser excitation.<sup>165</sup> The pretreatment may damage the sample and be time-consuming, and FPs are short lifetime within 10 ns similar to autofluorescence.

More robust and easier ways to rapidly remove autofluorescence are necessary for both fixed sample observation and live cell imaging. According to chapter 3, SAFIRE successfully utilizes the optically controllable dark states of FPs and PS-FPs for autofluorescence suppression and selective imaging on customized microscopes. By controlling the secondary laser intensity, I can select background-free signals from modulatable FPs or PS-FPs and then extract >5-fold signal-to-background improved images in a few seconds. This simple modulation scheme without internal reference is readily adapted to currently available commercial microscopes, including laser scanning confocal, spinning disk confocal, light-sheet, and wide-field microscopes.

Human immunodeficiency virus (HIV) is one of world's most significant public health challenges, with an estimated 18.2 million people were receiving HIV treatment in mid-2016. The first step of HIV infection begins from the entry of virus, binding and then fusing to the host human immune CD4 cells.<sup>6, 178</sup> HIV initiates the binding from its envelope protein (gp120) to CD4 and a cellular co-receptor, followed by the conformation change of another envelope protein, gp41. The conformation change from envelope proteins activates the membrane fusion and then opens the membrane fusion pore for delivery of the viral contents into the host cells. Among the multiple steps,

scientists are not sure where the viral entry occurs, whether cell surface or intracellular compartments.<sup>179</sup> Recent research from the Melikyan Laboratory utilized single virion fluorescence tracking to demonstrate that complete HIV-1 fusion happens in endosomes.<sup>6,</sup>  
<sup>84</sup> This endocytic HIV-1 entry mechanism can protect the virus entry from inhibitors, which target intermediate conformation of envelope proteins, and may enhance infection efficiency because the entry is closer to the nucleus – the ultimate target of HIV. Accordingly, the design of HIV entry inhibitors should consider the ability to permeate the cell membrane.

Since the complete virus exists inside live cells, autofluorescence from metabolites and cellular compartments is problematic for visualizing the virus particles. Cells become thicker closer to nucleus; more uniform autofluorescent background lowers the imaging contrast, and more non-uniform autofluorescence creates false-positive signals. Therefore, autofluorescence removal techniques are required to track true virus particles intracellularly. To meet the requirement, image acquisition in less than one second is required to capture the dynamics of moving virus, and imaging longer than one hour is needed for complete tracking of full HIV-1 virus entry. SAFIRE has demonstrated up to 20-fold improvement on customized microscopes but we have not optimized the time resolution for one demodulation image and minimized the modulation cycles on commercial microscopes. In this chapter, I will adapt SAFIRE to commercial microscopes, test the photophysical limitations, and demonstrate autofluorescence suppression with virus imaging in fixed/live cells.

## 4.2 SAFIRE on Currently Available Commercial Microscopes

### 4.2.1 Demonstration of SAFIRE with Modulatable FPs on Commercial Microscopes

From previous research, FPs and PS-FPs can be modulated and show >5-fold imaging contrast improvement with autofluorescence suppression, and the main differences between FPs and PS-FPs are dark state lifetimes. The dark state lifetimes of modulatable FPs are short (~1 ms), excited by a secondary laser with longer wavelength than the fluorescence. The currently known modulatable FPs<sup>48-49, 112</sup> require ~kW/cm<sup>2</sup> laser intensity for the primary laser to generate detectable dark state population and for a secondary laser to pump the dark molecules back to emissive manifold. Though modulatable FPs are modulated by secondary lasers without inducing autofluorescent background, the required intensity (kW/cm<sup>2</sup>) is only available for commercial microscopes with a single laser point, e.g. a confocal laser scanning microscope (CLSM). In contrast, the dark state lifetime of PS-FPs are longer (longer than 1 second) than FPs and excited by a secondary laser with shorter wavelength than the fluorescence. The long dark state lifetime allows for larger dark state population to accumulate, so 100-fold weaker intensity for primary and secondary lasers (~10 W/cm<sup>2</sup>) can be used for PS-FPs. Though high energy secondary laser induces autofluorescent background, much weaker intensity of illumination sources is suitable for most commercial microscopes.

Short-lived dark states of FPs require strong (kW/cm<sup>2</sup>) illumination for generating detectable enhancement. I have tested SAFIRE on a CLSM (Zeiss 780) and a SDCM (PerkinElmer UltraVIEW VoX), and only the CLSM regenerates detectable modulatable fluorescence under high intensity secondary laser illumination (>1 kW/cm<sup>2</sup>), while the maximum illumination intensity of the SDCM (~20 W/cm<sup>2</sup>) cannot modulate observable

signals. In addition, since the dark state lifetime of FPs is around one millisecond, the dwell time of one pixel for laser scanning should be long for accumulating enough dark state population. Commonly, CLSM scans a sample with one microsecond dwell time at each pixel thereby imaging entire view (512\*512 pixels) in one second. However, if each pixel is several microseconds, no obvious demodulated signals appear from mVenus, which exhibits ms-lived dark states<sup>112</sup> (Table 4.1) (Figure 4.1A). After tuning the dwell time to closer to one millisecond, mVenus shows a more obvious demodulation image (Figure 4.1B). When dwell time for each pixel is around one millisecond, the Zeiss system only allows a small area illumination (25  $\mu\text{m}$ \*25  $\mu\text{m}$ ) and requires several seconds for one image, greatly limiting the observation area and time resolution. This limitation precludes applications for investigation of biological interactions in millisecond range and observation of multiple cells. The dark state lifetimes from all modulatable FPs are around milliseconds<sup>48-49, 112</sup> (Table 4.1), so the FPs are not optimal tools for live cell SAFIRE-imaging on commercial microscopes.

Table 4.1 Summary of optically modulatable FPs and PS-FPs. Characteristic frequency ( $\nu_c$ ) means the frequency when enhancement drops to 50% of its maximum value. The primary (1<sup>st</sup>) and secondary (2<sup>nd</sup>) laser intensity for enhancement and characteristic frequency is: modBFP/H148K (1<sup>st</sup>: 560 W/cm<sup>2</sup>; 2<sup>nd</sup>: 36 kW/cm<sup>2</sup>), greens and yellows (1<sup>st</sup>: 1.9 kW/cm<sup>2</sup>; 2<sup>nd</sup>: 25 kW/cm<sup>2</sup>), red (1<sup>st</sup>: 13 kW/cm<sup>2</sup>; 2<sup>nd</sup>: 100 kW/cm<sup>2</sup>), PS-FPs (1<sup>st</sup>: 50 W/cm<sup>2</sup>; 2<sup>nd</sup>: 4 W/cm<sup>2</sup>).<sup>48-50, 112</sup>

Fluorescent Proteins (FPs)	$\lambda_{\text{EX}}/\lambda_{\text{EM}}$ (nm)	Primary (nm)	Secondary (nm)	Enhancement (%)	$\nu_c$ (Hz)
modBFP/H148K	390/455	405	514	15	37
AcGFP	480/505	476	561	8	760
EGFP	488/507	476	561	Non-mod	
EYFP	514/527	476	594	12	800
Venus	515/528	476	594	16	816
dsRed-m	556/586	561	700	27	3000
Photoswitchable Fluorescent Proteins (PS-FPs)	$\lambda_{\text{EX}}/\lambda_{\text{EM}}$ (nm)	Primary (nm)	Secondary (nm)	Enhancement (%)	$\nu_c$ (Hz)
rsFastLime	496/518	488	405	>100	<10
Dronpa2	489/515	488	405	>100	~100

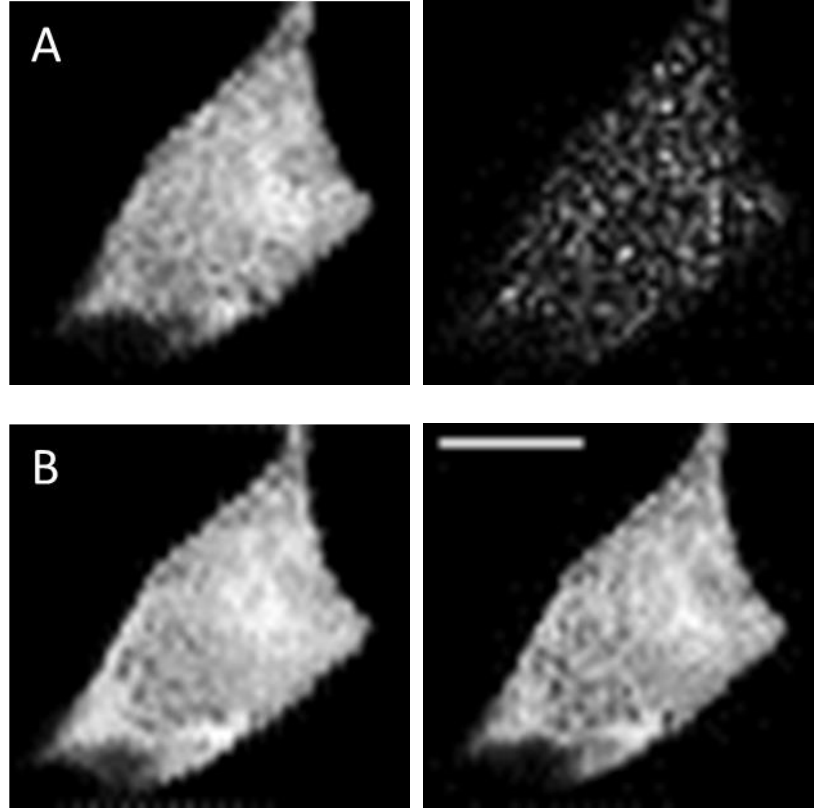


Figure 4.1 SAFIRE on fixed cells expressing untargeted-mVenus with CLSM (Zeiss). (A) Dwell time of laser scanning for one pixel is 8.44  $\mu\text{s}$  showing no demodulated signals. Left: Fluorescence. Right: Demodulation image. (B) Dwell time of laser scanning for one pixel is 270  $\mu\text{s}$  showing demodulated signals. Left: Fluorescence. Right: Demodulation image. Scale bar: 10  $\mu\text{m}$ .

#### 4.2.2 Demonstration of SAFIRE with PS-FPs on Commercial Microscopes

PS-FPs are modulatable under mild illumination intensity ( $\sim 10 \text{ W/cm}^2$ ) for both primary and secondary lasers mentioned in chapter 3, but the high energy secondary laser not only recovers the fluorescence of PS-FPs but also induces autofluorescent background. Alternatively, the fluorescence of PS-FPs can be separated from autofluorescence by fluorescent signal differences before and after secondary laser because the recovery from the secondary laser dramatically increases the emissive manifold of PS-FPs, while autofluorescent background populations do not change. Following this idea, after the pre-illumination of 488 nm laser, the rsFastLime signals

before the 405 nm (secondary) illumination are much lower than after that (Figure 4.2A). Utilizing the fluorescence differences between channels, I successfully demodulated the images in CLSM and SDCM, allowing for faster imaging over larger areas. Therefore, PS-FPs including rsFastLime demonstrate potential for visualizing biological interactions and tracking particles without autofluorescence in live cells.

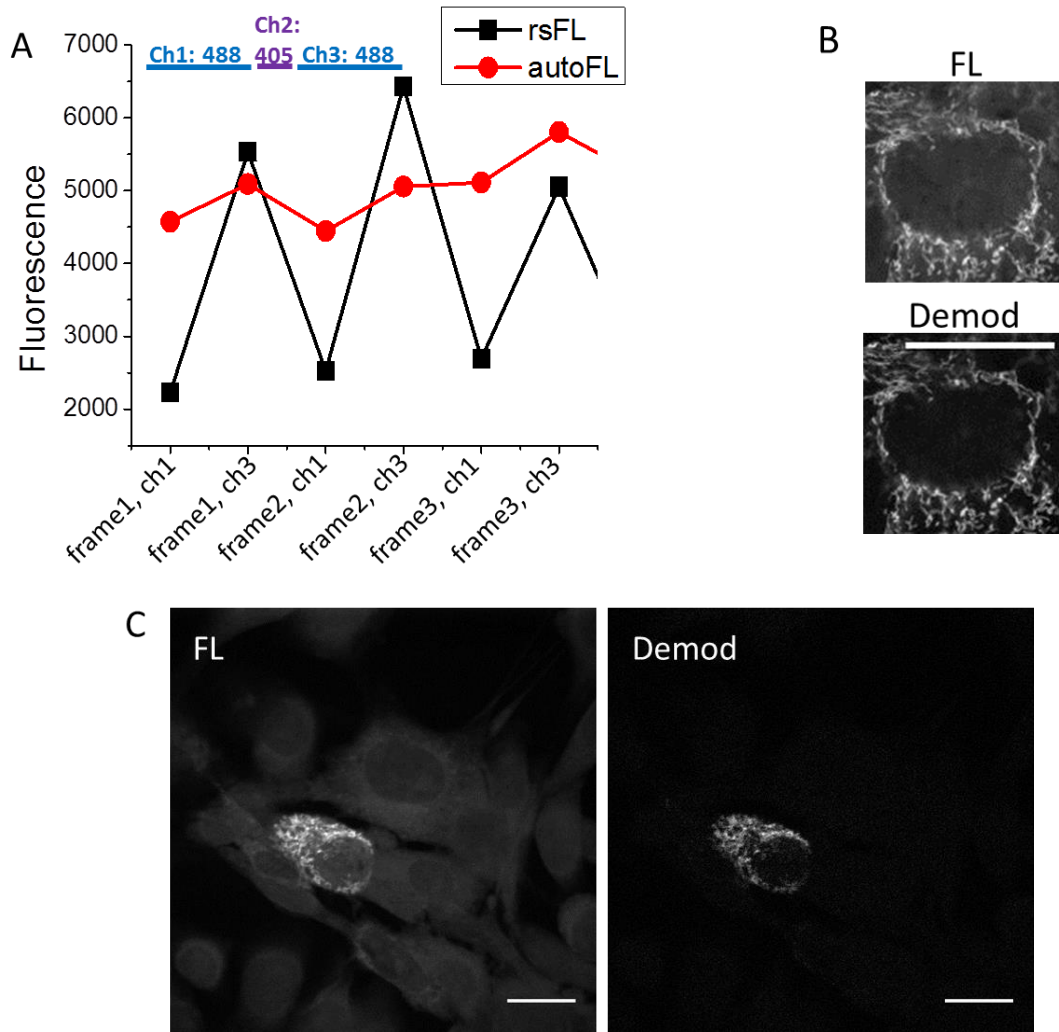


Figure 4.2 SAFIRE imaging with fixed cells expressing mitochondria-rsFastLime with confocal microscopes. (A) Within 1 frame, three channels of illumination are applied. Channel 1: 488 nm (primary); Channel 2: 405 nm (secondary); Channel 3: 488 nm (primary). After the pre-illumination of 488 nm laser, the rsFastLime (rsFL) fluorescence of ch3 after the 405 nm recovery is much larger than ch1, while autofluorescence (autoFL) in ch3 is similar to that in ch1. (B) The fluorescence image (FL) and demodulation image (Demod) from CLSM. The Demod image was from the differences between fluorescence in ch3 and ch1, while FL image is the average of all fluorescence. (C) The fluorescence image (FL) and demodulation image (Demod)

from SDCM. The Demod image was from the differences between fluorescence in ch3 and ch1, while FL image is the average of all fluorescence. Scale bar: 20  $\mu\text{m}$ .

### 4.3 Visualization of Virus Particles on Commercial Microscopes

The demonstration of autofluorescence suppression initiated collaboration with the Melikyan Laboratory at Emory to observe the entry of HIV-1 into CD4 cells. Because of the obvious uniform and non-uniform background in the cell lines, virus-like-particles (VLPs) were not trackable and are confused with false-positive autofluorescent signals. After expressing rsFastLime in VLPs, the rsFastLime-VLPs are separated from virus-like autofluorescence by SAFIRE on a SDCM (PerkinElmer UltraVIEW VoX) (Figure 4.3). Long observation time (around one hour) and improved time resolution (less than 500 ms each frame) are also required for the investigation of HIV-1 virus entry in live cells. Fewer photoswitching cycles of rsFastLime for one demodulation image benefit time resolution and more observation cycles because the total switching cycles are limited. Balancing between signal-to-background ratio, time resolution, and total observation time, I currently utilize four channels (ch1: 488 nm, ch2: 405 nm, ch3: 488 nm, ch4: 488 nm) to demodulate nonlinearly (Figure 4.4A),

$$\text{nonlinear demodulation} = \frac{(ch3 - ch1)(ch3 - ch4)}{ch3}.$$

The nonlinear demodulation image only requires one photoswitching cycle of rsFastLime in less than 500 ms to achieve enough signal-to-background ratio (Figure 4.4B), while EGFP-VLPs do not show demodulated signals (Figure 4.5). However, noise may generate similar waveform to rsFastLime thereby contributing random bright spot in demodulation images (Figure 4.5B), which can be removed by additional image processing or more modulation cycles for one demodulation frame.

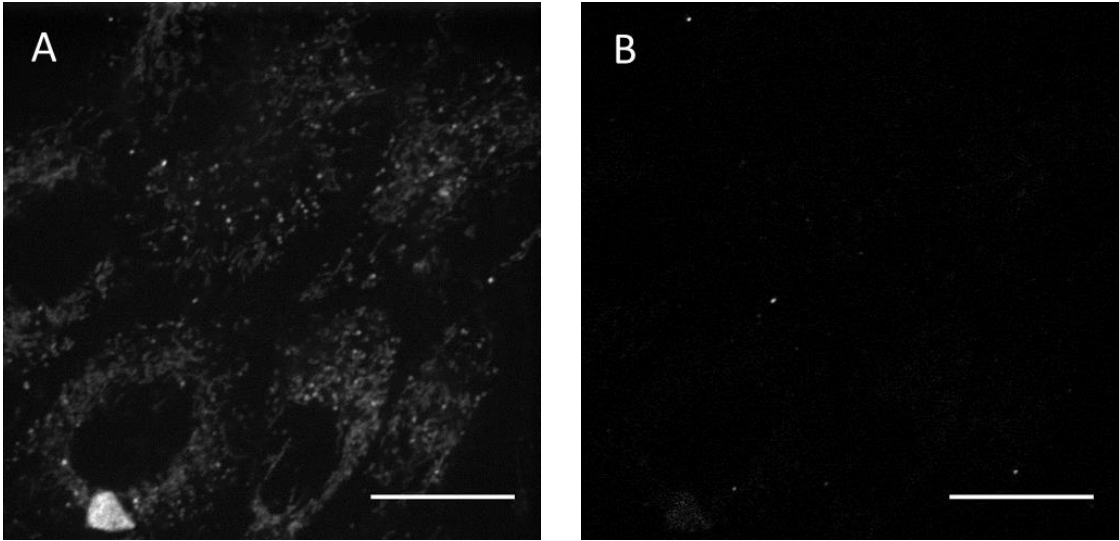


Figure 4.3 Demodulation of rsFastLime-VLPs from abundant autofluorescence in CV-1 cell line with a SDCM. (A) Fluorescence image. (B) Demodulation image. Scale bar: 20  $\mu\text{m}$ .

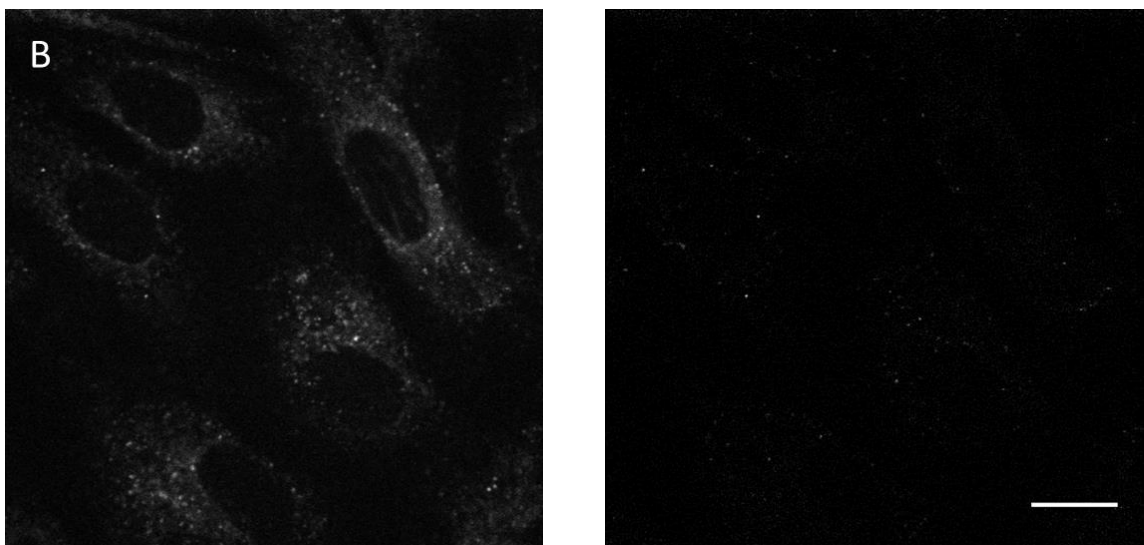
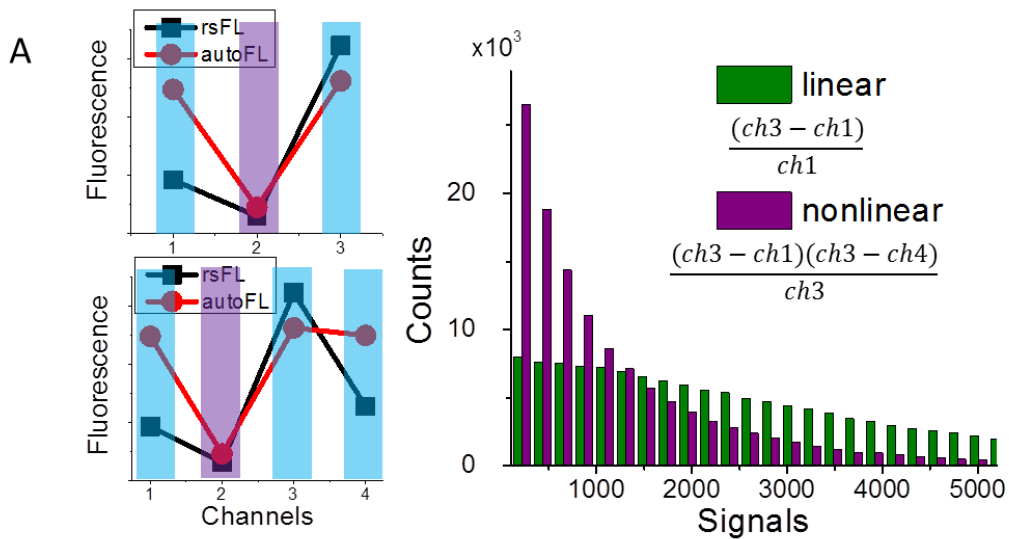


Figure 4.4 Nonlinear demodulation of rsFastLime-VLPs from CV-1 cell line with SDCM. (A) Differences between linear (ch1: 488 nm, ch2: 405 nm, ch3: 488 nm), and nonlinear (ch1: 488 nm, ch2: 405 nm, ch3: 488 nm, ch4: 488 nm) demodulations. Differences between 488nm-excited signals before (ch1) and after (ch3) 405 nm recovery generates linear demodulation, while nonlinear demodulation utilizes additional ch4 for calculation. The nonlinear processing successfully narrows the population of background signals compared to linear processing. (B) One photoswitching cycle of rsFastLime successfully demodulates VLP signals out of autofluorescence. Left: Fluorescence image. Right: Demodulation image. Scale bar: 20  $\mu\text{m}$ .

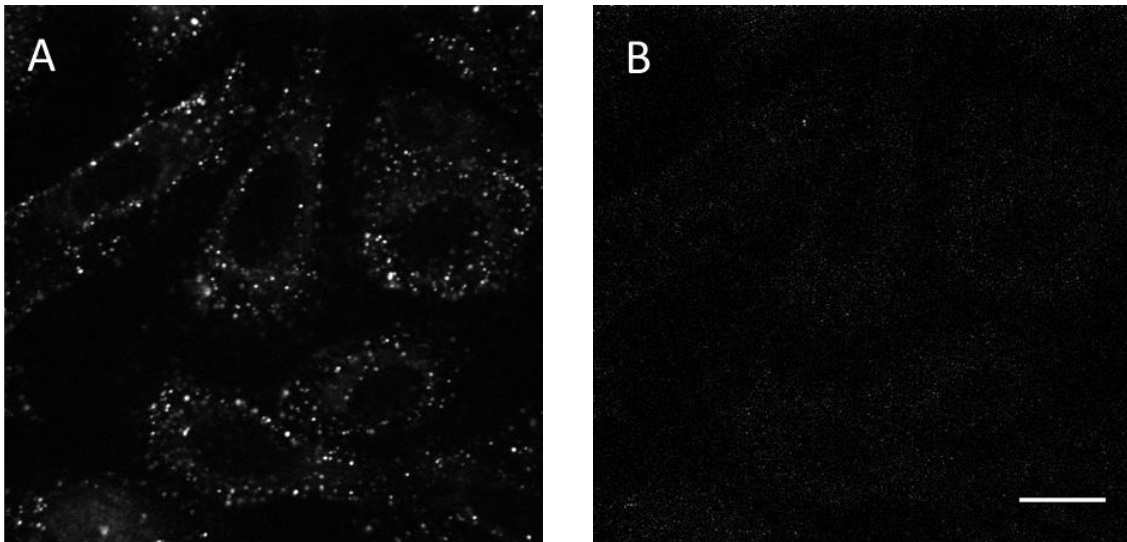


Figure 4.5 No demodulated signals from EGFP-VLPs with nonlinear demodulation calculation with SDCM. (A) Fluorescence image. (B) Demodulation image. The only bright spot on the demodulated image is from the fluctuation of noise in the background, not from EGFP-VLPs.

After the demonstration of autofluorescence suppression on a spinning disk confocal, our collaborators are able to visualize rsFastLime-VLPs without confounding background with a wide-field microscope (GE Personal DeltaVision imaging system). Though the center of the cells are thicker and often include more cellular compartments accompanied by autofluorescence, the ultimate target of virus--nucleus is in this region. From live cell imaging, VLPs in both peripheral and central regions of cells are observed after demodulation (Figure 4.6). Currently, the investigation of HIV-1 entry with SAFIRE on commercial microscopes is still an ongoing project.

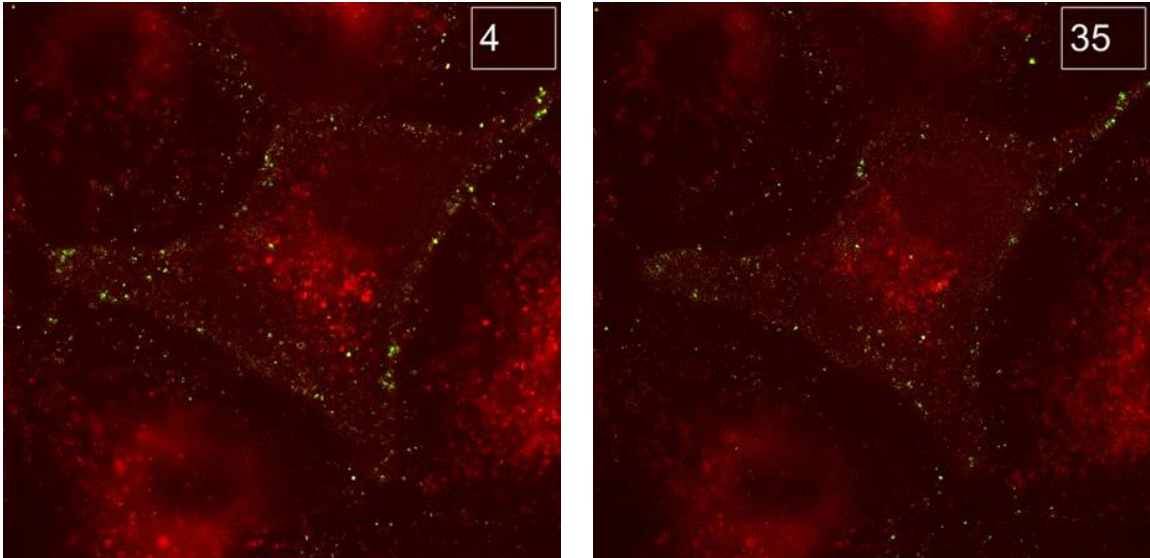


Figure 4.6 The combination of fluorescence (red) and demodulation (green) images on live cell imaging with a wide-field microscope. rsFastLime-VLPs can be observed in both central and peripheral area of CV-1 cell line even with abundant autofluorescence. Left: Video at frame 4. Right: Video at frame 35. The data acquisition time of each demodulation was around 500 ms, and each frame was taken at every 6 seconds.

#### 4.4 Conclusion

Autofluorescence is a long-existing problem without a fast and robust solution. Currently, scientists might spectrally unmix the images by assuming broader emission of autofluorescence than FPs signals, or sample pre-photobleaching can be applied for background removal. However, autofluorescence may be from unknown molecules, and the sample time-consuming pre-treatment can damage the sample. Since this problem is universal for most biological groups, a robust solution is necessary and should be applicable to all the imaging microscopes.

SAFIRE has demonstrated the ability for autofluorescence suppression on confocal and wide-field microscopes without internal reference point in a few seconds, so the adaptation from customized microscopes to commercial microscopes will be more applicable to other research groups. In this chapter, I have demonstrated SAFIRE on CLSM (Zeiss 780), SDCM (PerkinElmer UltraVIEW VoX), and a widefield microscope

(GE Personal DeltaVision imaging system). Also, fixation of NIH-3T3 cells and fixed, live CV-1 cell lines demonstrate successful autofluorescence suppression. All microscopes and biological samples with rsFastLime show significant autofluorescence suppression. In addition to the primary demonstration, improved time resolution of demodulation images are shown in collaboration with a virology group, investigating the mechanism of HIV-1 entry into CD4 cells.

## CHAPTER 5 OPIOM-SAFIRE

### 5.1 Introduction

The optically accessible dark states serve as another parameter for superresolution microscopy, autofluorescence suppression, and selective imaging that is orthogonal to emission wavelength and fluorescence lifetime. SAFIRE utilizes a secondary laser to pump dark state population of FPs or PS-FPs back to the ground state (emissive manifold). By facilitating the regeneration of emissive manifold, a secondary laser recovers the fluorescence, and the amount of fluorescence recovery can be calculated as enhancement, which is the ratio of fluorescence with a secondary laser versus without it. The intensity of secondary laser can also be externally modulated, and the fluorescence will display the same modulation frequency as the secondary laser, which is mentioned in chapter 3 as single-modulation SAFIRE (SM-SAFIRE).

Two types of information can be generated by intensity modulation of a secondary laser. First, phase ( $\phi$ ) differences between excitation and emission waveforms as a result of finite dark state lifetime. Second, amplitude at the highest vs. that at the lowest point, equivalent to enhancement when the secondary modulation is 100%, is proportional to the population of optically modulatable dark state (Figure 5.1).<sup>59</sup>

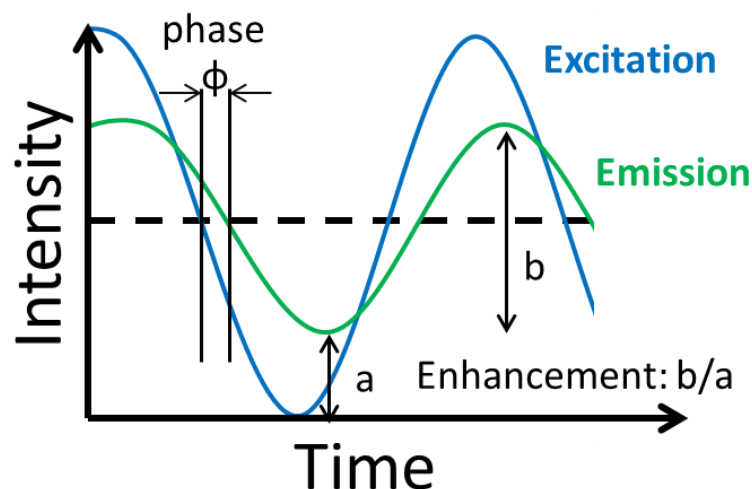


Figure 5.1 Modulation of laser excitation generates information of phase ( $\phi$ ), from finite dark state lifetime, and enhancement, proportional to the population of optically modulatable dark state.<sup>59</sup>

In previous chapters, enhancement from SAFIRE is utilized for discriminating between the fluorescence with optically controllable dark states and the fluorescence without them. This was demonstrated by autofluorescence suppression as well as potential for selective imaging and for improving the detection limit of protein-protein interactions by enhancing binding signals. Similarly, phase information in addition to enhancement can also be utilized for autofluorescence suppression. In 2015, the Jullien Laboratory developed out-of-phase imaging after optical modulation (OPIOM)<sup>42</sup> for autofluorescence suppression and selective imaging based on the lifetime of photophysical dark states.

The modulated laser in frequency-domain lifetime measurement increases the excited state population, and modulated secondary laser in SM-SAFIRE regenerates the ground state (emissive manifold) population back from dark state. However, modulated primary laser in OPIOM not only generates fluorescence signals but also increase the dark state population (Figure 5.2), enhancing the nonlinearity and creating anomalous

phase advance in of fluorescence response. This anomalous phase advance was first observed in flavin adenine dinucleotide (FAD),<sup>180</sup> a fluorophore with a  $\mu$ s-range dark state, modulated by a sinusoidal primary laser.

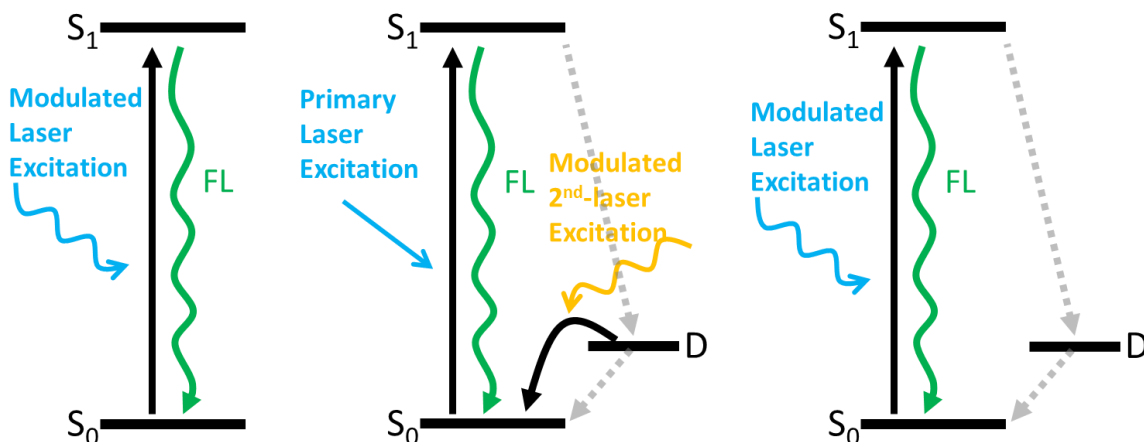


Figure 5.2. Different ways for generating phase difference ( $\phi$ ). (Left) Frequency-domain lifetime measurements. The modulated laser excites the ground state ( $S_0$ ), and then fluorescence (FL) emits from excited state ( $S_1$ ) with finite lifetime. (Middle) SM-SAFIRE. The modulated secondary ( $2^{\text{nd}}$ ) laser regenerates the ground state population from the dark state to enhance the fluorescence. (Right) OPIOM. The modulated primary laser not only generates fluorescence but also creates dark state population. Since modulated lasers in frequency-domain lifetime measurements and SM-SAFIRE increase fluorescence signals, while the modulated laser in OPIOM not only generates fluorescence but also increases dark state population, the fluorescence waveform in OPIOM is different from frequency-domain lifetime measurements and SM-SAFIRE.

Accumulation of dark state population from a modulated laser creates nonlinearity of fluorescence response, which was observed as anomalous phase advance.<sup>180</sup> This “advance” arises from the continuous, slow flow of population from the dark to bright manifold of states at a rate that is slower than the modulation frequency. This slow and nonlinear response to sinusoidal excitation of the ground state distorts the fluorescence response from the modulation waveform, with the rise in fluorescence being more rapid than the fall (Figure 5.3) because of the accumulation of dark state population.<sup>180-182</sup> As the entire fluorescence response is directly modulated with the primary excitation laser modulation waveform, the out of phase component is very small unless a large dark state

fraction is achievable. Thus, only long-lived PS-FPs have been utilized for imaging contrast, with the amplitude of out-of-phase signals being related to the dark state lifetime.<sup>42</sup> While SAFIRE can also be applied to modulate fluorophores with short-lived dark states, OPIOM, OLID (optical lock-in detection) and SAFIRE can all utilize slow photophysics to discriminate PS-FPs signals from similarly emitting non-photoswitchable fluorophores.

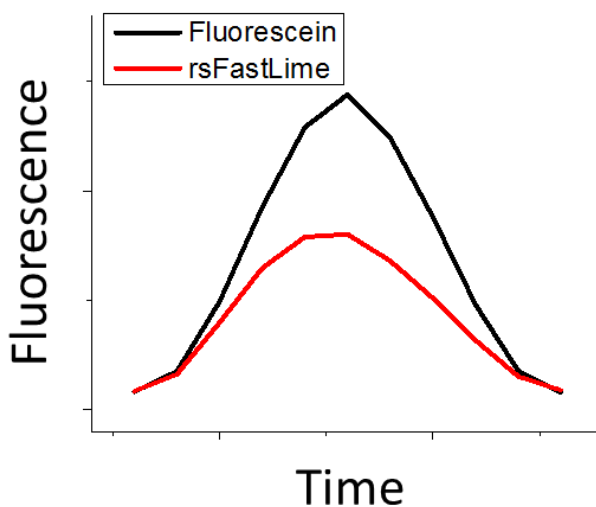


Figure 5.3 Fluorescence time trace of fluorescein and rsFastLime with sinusoidal primary laser modulation. Fluorescein with no obvious dark state follows the primary laser intensity, while rsFastLime shows an apparent “phase advance” from hysteresis of the dark state.

Nonlinearity of fluorescence response from dark state population creates anomalous phase advance, so out-of-phase fluorescence signals depend on time scale of dark state relaxation. If the modulation is too slow, the dark state decays back to the bright manifold before the modulation cycle completes; if it is too fast, the molecules cannot reestablish steady-state dark and bright populations within each modulation period. Thus, modulating too slowly minimizes the out-of-phase component, while modulating too rapidly decreases enhancement. Maximum out-of-phase signals are at the primary modulation frequency that is comparable to dark state relaxation time. Therefore, OPIOM can selective image

multiple PS-FPs with different dark state lifetimes, which is similar to the selective imaging mentioned in chapter 3. However, the long-lived dark state lifetimes of PS-FPs requires primary modulation at very slow frequency ( $< 10$  mHz), impractical to general use by biological applications. By utilizing a continuous secondary laser to rapidly generate emissive manifold of PS-FPs, I can greatly shorten the total acquisition time compared to OPIOM.

## **5.2 Improved OPIOM by Optically Controllable Dark States**

When the primary laser modulation period is comparable to the dark state relaxation time, an apparent phase advance<sup>180</sup> (Figure 5.3) is observed relative to the modulation waveform. Using only a single excitation source, OPIOM relies on producing large steady-state dark state populations which thermally relax to the ground state. Under these circumstances, modulated Dronpa-2 (Dronpa-M159T) fluorescence shows a phase shift of fluorescence relative to the modulated excitation waveform. However, the long-lived dark state lifetime of Dronpa-2 requires extremely slow (4.93 mHz,) modulation frequency for out-of-phase signals with OPIOM. SAFIRE offers the opportunity to improve on this promising scheme by employing a second laser to hasten ground state recovery and imaging rates  $\sim 1000$ -fold over the original OPIOM implementation. Thus, the combination of SAFIRE with OPIOM offers the opportunity to control the dark state lifetime for improved resolution and dynamics.

To actively control dark state lifetime, we excite fluorescence of rsFastLime immobilized within fixed cells with a sinusoidally modulated primary laser (488nm, Figure 5.4) as in OPIOM, but also co-illuminate the dark state with cw secondary excitation at 405 nm. Without co-illumination at 405 nm, even modest  $\sim 1$  W/cm<sup>2</sup> 488 nm

illumination leads to nearly all rsFastLime molecules trapped in the long-lived (~480 seconds) dark state, decreasing total fluorescence. The 405nm co-illumination more rapidly regenerates the fluorophore ground state than possible through natural decay. Modifying 405-nm secondary intensity thereby tunes the dark state lifetime, providing a mechanism by which one can shift the maximum modulation frequency for faster imaging or improved molecular discrimination.

Longer-lived dark states increase steady-state dark state populations and dark state hysteresis for larger out-of-phase signals ( $FL_{out}$ ), which are the fluorescence signals (cosine) 90 degree different from the sinusoidal excitation. This limits imaging speed as very low modulation frequencies used for OPIOM<sup>42</sup> since the modulation frequency must be comparable to the dark-state lifetime for maximum  $FL_{out}$ . If the modulation is too slow, the dark state decays before the modulation cycle completes; if it is too fast, the molecules cannot reestablish steady-state dark and bright populations within each modulation period. Thus, modulating too slowly minimizes the out-of-phase component, while modulating too rapidly decreases modulation depth. Consequently, the long-lived (>1 minute<sup>100</sup>) dark states of PS-FPs make live cell imaging with OPIOM somewhat impractical. Co-illumination of sinusoidally 488nm-excited rsFastLime with adjustable 405nm intensity, however, offers the ability to tune the dark state lifetime from minutes to milliseconds, while also controlling the magnitude of  $FL_{out}$  (Figure 5.5).

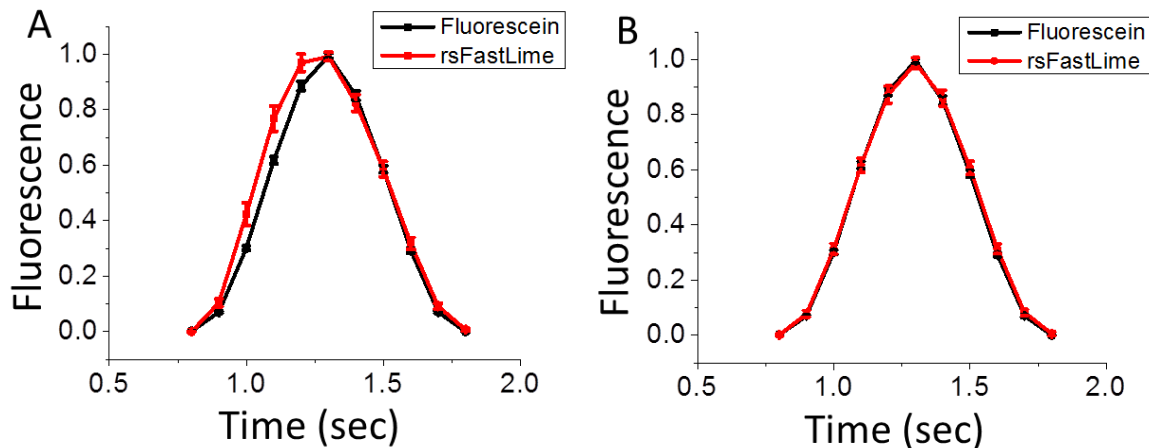


Figure 5.4 PS-FP, rsFastLime, fluorescence time traces from sinusoidally intensity-modulated 488 nm excitation. Normalized curves are plotted relative to modulated fluorescein emission collected under identical conditions. Samples were co-illuminated at 405nm with intensities of (A)  $0.25\text{W}/\text{cm}^2$  and (B)  $3\text{W}/\text{cm}^2$ . Fluorescein emission tracks the excitation waveform, while rsFastLime fluorescence appears advanced in phase. The phase advance at a given modulation frequency changes with 405nm laser intensity.

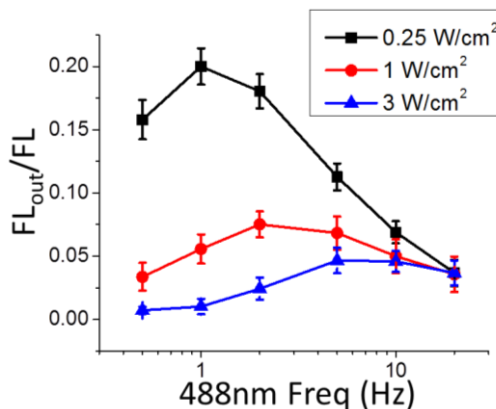


Figure 5.5 Experimental out-of-phase signals ( $FL_{out}$ ) upon varied 405nm laser intensity. (A) Out-of-phase (cosine) rsFastLime fluorescence amplitude resulting from sinusoidally modulated, 488nm ( $8\text{ W}/\text{cm}^2$  average intensity) and continuous, homogeneous 405nm laser excitation for several 405nm intensities. At increasing 405nm intensities, the out of phase maxima shift from low to high frequency.

Because the introduction of a second laser to OPIOM controls dark state lifetime, this scheme offers the potential for greatly improved signal discrimination and increased imaging rates. Since the maximum out-of-phase signal is determined by the 405 nm laser intensity, illumination of rsFastLime samples with non-uniform 405 nm intensity profiles encodes different out-of-phase responses on each CCD pixel (Figure 5.6). This provides an

additional dimension to discriminate fluorophores based on either intrinsic<sup>42, 48, 50</sup> or secondary laser (405 nm) intensity dependent dark state lifetimes. rsFastLime<sup>100, 175</sup> is an efficient PS-FPs excited at low 488 and 405 nm laser intensities ( $<100 \text{ W/cm}^2$ ) for potential uses in commercial microscopes. This approach minimizes photobleaching and phototoxicity effects, while being able to record out-of-phase signals with CCD acquisition on the sub-second time scale. Similar to SAFIRE and OLID, secondary-laser-enhanced OPIOM (SAFIRE-OPIOM) enables discrimination of spectrally overlapped fluorophores on the basis of their photophysical dark state dynamics.

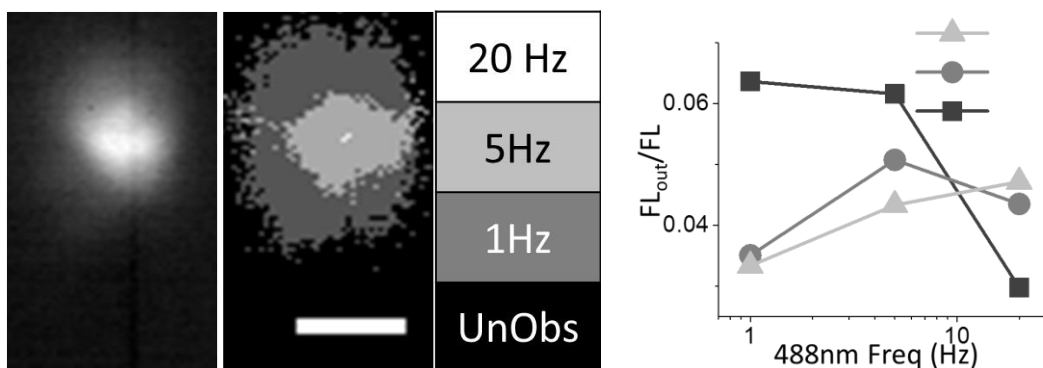


Figure 5.6 Heterogeneous 405 nm illumination creates different out-of-phase responses based on intensity profile. (Left) With weakly focused 405nm co-illumination in a much larger, spatially homogeneous wide field 488nm illumination, the out-of-phase ( $FL_{out}$ ) signal maximum increases in frequency at spatial positions exhibiting higher 405 nm secondary intensities. The raw fluorescence and out of phase maxima at each pixel are shown in the two images, with the color indicating the maximum of the out of phase signal at each pixel, while outside the 405 nm illumination spot, the fluorophores are unobservable (UnObs, black), as they are all switched into the dark state under 488 nm illumination alone. (Right) The plot shows the  $FL_{out}$  amplitude vs. 488 nm modulation frequency for rsFastLime at low (square), medium (circle) and high (triangle) 405nm intensity. 488nm intensity,  $40 \text{ W/cm}^2$ , is spatially invariant over the image. Scale bar:  $1 \mu\text{m}$ .

### 5.3 Three-State Model for SAFIRE-OPIOM

Three-state model comprises ground ( $S_0$ ), excited ( $S_1$ ), and dark states (D) of rsFastLime based on 3-by-3 matrix (Figure 5.7). From the matrix, the equations for the ground state, excited emissive state, and dark state are

$$\begin{aligned}\partial_t P(S_0(t)) &= -k_{01} [I_{488\text{nm}}, I_{405\text{nm}}] P(S_0(t)) + k_f P(S_1(t)) \\ &\quad + (k_{off} + k_{405,off} [I_{488\text{nm}}, I_{405\text{nm}}]) P(D(t)) \\ \partial_t P(S_1(t)) &= k_{01} [I_{488\text{nm}}, I_{405\text{nm}}] P(S_0(t)) - (k_f + k_D) P(S_1(t)) \\ \partial_t P(D(t)) &= k_D P(S_1(t)) - (k_{off} + k_{405,off} [I_{488\text{nm}}, I_{405\text{nm}}]) P(D(t)).\end{aligned}$$

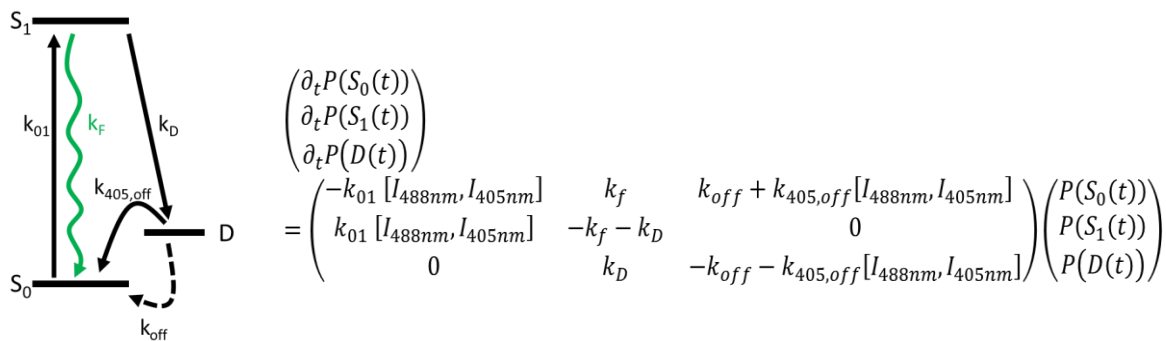


Figure 5.7 Three-state model. Left: The three-state model consists of a ground state ( $S_0$ ), an excited state ( $S_1$ ), and a dark state ( $D$ ). After the laser excitation ( $k_{01}$ ), photons in  $S_1$  fluoresce ( $k_F$ ) or turn ( $k_D$ ) into  $D$ , then thermally relaxation ( $k_{off}$ ) and laser-induced relaxation ( $k_{405,off}$ ) back to  $S_0$ . Right: Rate matrix for the three-state model.

Table 5.1 Photophysical parameters for rsFastLime.

Bright state		Dark state		Bright $\rightarrow$ Dark	
$\epsilon_{S_0}^{175}$	$33000 \text{ M}^{-1} \text{ cm}^{-1}$	$\epsilon_D^{108}$	$13000 \text{ M}^{-1} \text{ cm}^{-1}$	$k_{ISC}^{183}$	$0.5 \text{ MHz}$
$\phi_F^{175}$	$0.6$	$\phi_{Rev}^{108}$	$0.13$		
488 nm intensity (mean)	$8 \text{ W/cm}^2$	$t_{off}^{175}$	$480 \text{ s}$		

With published photophysical parameters (Table 5.1), the numerical simulation can predict the out-of-phase signals and phase differences between excitation and emission (Figure 5.8). The extinction coefficient is lower than the published value ( $46000 \text{ M}^{-1} \text{ cm}^{-1}$ )<sup>175</sup> since we performed laser illumination on fixed rsFastLime not on rsFastLime solution. The mismatch of laser and fluorophore polarizations will lower the effective intensity experienced by the molecule. Since the in-phase modulation can result from both rsFastLime and autofluorescence, while out-of-phase signals only come from

rsFastLime, the  $\tan^{-1}$  value of the in-phase/out-of-phase ratio is not perfectly modeled by the simulation (Figure 5.7 D-E). In contrast, the out-of-phase signals (Figure 5.7 A-C) nearly perfectly match the simulated results.

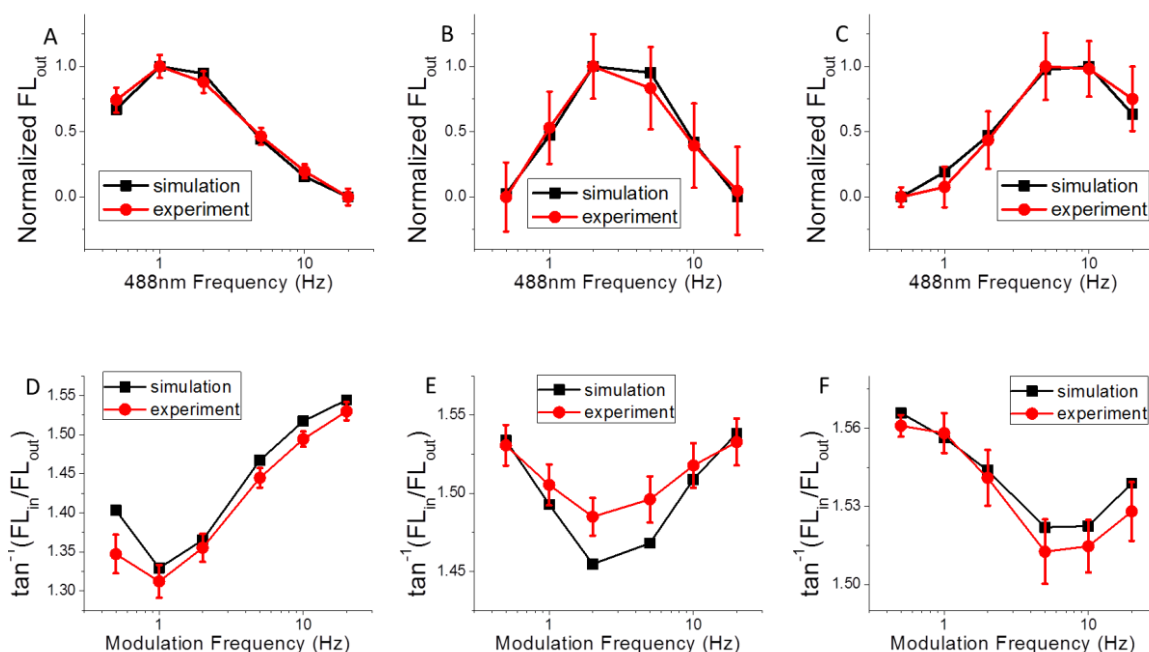


Figure 5.8 Comparison between experimental data (red) and numerical simulation (black) using a three-state model of rsFastLime. rsFastLime is co-illuminated with 8 W/cm<sup>2</sup> at 488 nm and (Left) 0.25 W/cm<sup>2</sup>, (Center) 1 W/cm<sup>2</sup>, and (Right) 3 W/cm<sup>2</sup> at 405nm. (A) (B) (C) out-of-phase signals, FL<sub>out</sub>. (D) (E) (F) phase differences between excitation and rsFastLime emission.

## 5.4 Super-Resolution Application

In contrast to the largely symmetric illumination and dark state lifetimes in Figure 5.5, co-illumination with asymmetric 405nm intensities provides an opportunity to utilize rsFastLime dark state lifetime as a probe of spatial position. The accuracy of our numerical simulations compared to our experimental results (Figures 5.8) enables us to simulate microscopy images of rsFastLime fluorescence employing a linear spatial intensity gradient at 405nm. rsFastLime molecules at slightly different spatial positions

are simulated, and final images are convolved with a point spread function using BlurLab3D.<sup>184</sup>

If a sufficiently large anisotropic spatial gradient (~6-fold intensity change over 50nm) is used, two rsFastLime molecules separated by 50 nm become readily resolved based on their different frequency-dependent out-of-phase fluorescence responses (Figure 5.9). Sub-diffraction spatial information from the 405nm intensity gradient is recoverable from observed dark state lifetimes. Thus, optical-controllable dark state lifetime offers a new dimension to resolve otherwise identical emitters, as each molecule experiences different 405nm intensities. In contrast to localization or point-spread function engineering methods, utilizing the out-of-phase signal resulting from controlling dark-state lifetimes in this SAFIRE-OPIOM approach suggests that scientists can simultaneously exclude autofluorescent background and non-modulatable emitters, while also potentially distinguishing emitters separated by less than the diffraction limit, all at moderate excitation intensities.

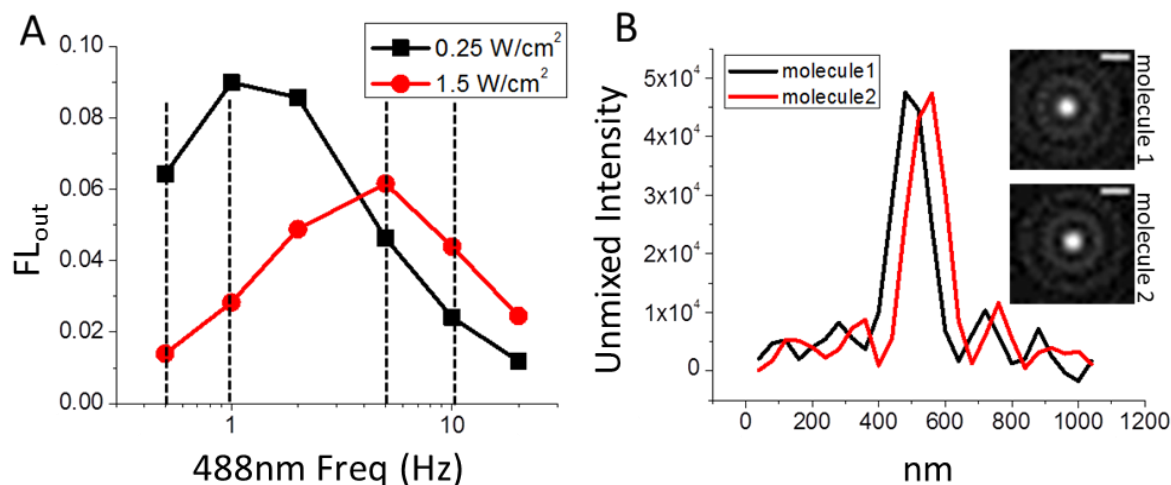


Figure 5.9 Simulated resolution of two diffraction-limited molecular emission patterns, separated by 50 nm, and illuminated at 6-fold different 405nm intensities. (A) With the recovered  $FL_{out}$  at two 405 nm intensities, we utilize spatially homogeneous 0.5Hz, 1Hz, 5Hz, and 10Hz modulated 488 nm excitation as reference values to spectrally unmix the overlap signals. (B) After point

spread function convolution and  $FL_{out}$  analysis, spectral unmixing of the modulation spectra enables recovery of the correct molecular positions, with a recovered distance of 49.2 nm. Scale bar: 250 nm.

Under dual illumination, with a spatially anisotropic secondary illumination pattern, each PS-FP exhibits modulated emission with a unique out-of-phase modulation response curve. Thus, spectral unmixing of the modulation responses improves signal discrimination as in OPIOM from out-of-phase response, while simultaneously enabling faster imaging and optical control of emitters by SAFIRE. Our accurate numerical simulations of optical response also suggest that molecules separated by less than the diffraction limit can be directly resolved by application of a spatially anisotropic 405nm intensity gradient, coupled with spectral unmixing of modulation responses. Thus, SAFIRE-OPIOM should speed imaging rates and enable dark state lifetime to be used as a new dimension for improving spatial resolution, when retaining the original signal discrimination ability of both OPIOM and SAFIRE.

## 5.5 Conclusion

Modulation of excitation light source generates enhancement of fluorophores as well as phase differences between excitation and emission. Large dark-state population of PS-FPs enables the out-of-phase signals to be detected in OPIOM for selective imaging, but the time resolution of this method is mainly limited to long-lived dark states of PS-FPs. SAFIRE-OPIOM optically accelerates dark state lifetimes with secondary illumination, and 1000-fold time resolution improvement is demonstrated on rsFastLime with low-intensity co-illuminated 405 nm laser. From several minutes to milliseconds, SAFIRE-OPIOM potentially allows live cell imaging and millisecond-scale dynamics to be probed. The matching of three-state model and experimental data provides predictive ability and possible application to super-resolution imaging. This combined

SAFIRE-OPIOM approach is likely to find wide application in high sensitivity biological imaging and can be more readily applied to studying biological interactions and dynamics with improved speed and sensitivity.

## CHAPTER 6 CONCLUSION AND OUTLOOK

Fluorescence microscopy is widely utilized in biology for visualization of targeted tissues, cells, intracellular compartments, specific genes, or low copy-number proteins. Targeted fluorescent probes allow for tracking specific molecules out of complicated cellular environment. For optimal biocompatibility and specificity, scientists developed genetically coded green fluorescent protein (GFP) labeling methods in 1990s. The genetically encoded fluorophores fuse with targets at 1-to-1 ratio, and the maturation of GFP without additional help from other enzymes can be expressed universally in all biological systems. Continuous mutation research on GFP creating a palette from blue to red benefits investigation of cellular interactions between multiple molecules. The universal multi-color FP tags enrich the capacity of fluorescent techniques for live cell imaging, molecule tracking, protein-protein interactions, and recent super resolution microscopy. However, the moderate brightness of FPs limits the signal-to-background ratio of fluorescence imaging, especially false-positive signals from non-uniform autofluorescent noise in some biological samples. In addition, multi-color imaging based on emission spectra suffers from the spectral overlap of FPs. In conclusion, development of autofluorescence suppression and multiplexed imaging would greatly benefit fluorescence microscopy.

By utilizing photophysical dark states of FPs, the Dickson Laboratory has developed synchronously amplified fluorescence image recovery (SAFIRE) for selective imaging modulatable fluorophores with dark states and eliminating same-color, non-modulatable species. Demodulation of fluorescence images on modulatable modBFP-H148K transfected cells enhances >5-fold signal-to-background imaging contrast in live cells by

suppressing autofluorescence. Following the previous research on FPs, I have been characterizing the photophysical dark states of rsFastLime, one of photoswitchable fluorescent proteins (PS-FPs). Slightly different from single modulation SAFIRE (SM-SAFIRE), dual modulation SAFIRE (DM-SAFIRE) allows for >5-fold signal-to-background imaging enhancement from the long-lived dark states of rsFastLime excited by high-energy secondary laser. After the proof-of-concept of demonstration on customized microscopes, I adapted the background-suppression fluorescence imaging to commercial laser scanning confocal (Zeiss), spinning disk confocal (PerkinElmer), and wide-field (GE) microscopes. In collaboration with the Melikyan Laboratory, this cost-effective imaging method selectively visualizes HIV-1 particles transfected with rsFastLime while removes non-modulatable false-positive autofluorescent background in demodulation images. Combination between SAFIRE and spinning disk confocal, wide-field microscopes improves the time resolution to around 0.5 second for one demodulation image, which allows for virus tracking in live cells.

In addition to the discrimination between modulatable and non-modulatable FPs, different dark state lifetimes enable for selective imaging between different modulatable FPs with same emission-wavelength, or discrimination between immobilized and diffusing yet the same FPs bases on the residence time in a laser focus. The spectral unmixing between two PS-FPs, rsFastLime and Dronpa2, with different dark state lifetimes is proposed and demonstrated by Monte Carlo simulations. In addition to unmixing between different PS-FPs, the dark state lifetime of rsFastLime is tuned to be slower than diffusion time by adjusting excitation intensity. The diffusing rsFastLime

cannot accumulate enough dark state population for demodulation, while immobilized ones show 10-fold DM-SAFIRE signals.

Laser intensity modulation generates amplitude of fluorescent response as well as phase differences between excitation and emission. Out-of-phase imaging after optical modulation (OPIOM) utilizes the phase differences generated from long-lived dark states of PS-FPs for selective imaging; however, the poor time resolution (more than one minute) is also from the intrinsic long-lived dark states. Accelerated by moderate secondary laser intensity ( $\sim 1 \text{ W/cm}^2$ ), SAFIRE-OPIOM can be observed at milliseconds on camera. Based on the accurate prediction from a simple three-state model, SAFIRE-OPIOM is able to discriminate the molecules experienced by heterogeneous secondary illumination intensity. The numerical simulation suggests 6-fold secondary intensity differences can resolve the two molecules 50 nanometers apart.

Dark states of FPs are starting to be an additional dimension for the advancement of fluorescence microscopy. In this thesis, optically controllable dark state lifetimes of PS-FPs show multiple potential for autofluorescence removal, selective imaging, and possible super resolution applications. The great potential of dark states has not been widely explored. So far, the FPs and PS-FPs are not mutated for better enhancement after secondary laser illumination, or for dark state lifetime tuning, which requires the understanding of FPs structural information of dark states. In addition, discrimination between diffusing and immobilized fluorophores has a potential for improving the detection limit of weak protein-protein interactions; the super resolution applications of SAFIRE-OPIOM need experimental design. Most importantly, understanding what

biologists need, solving critical biological problems, and communicating with biology/medicine community are significant for the advancement of imaging methods.

# **APPENDIX A STUDYING PROTEIN-PROTEIN INTERACTIONS IN THE IMMUNE SYSTEM WITH FLUORESCENCE CORRELATION SPECTROSCOPY**

## **A.1 Introduction**

Transient Protein-protein interactions (PPIs) are temporary in nature, but many of these, such as receptor-ligand interactions in signal transduction, are crucial to the regulation of myriad important cellular processes. Therefore, the thermodynamic and kinetic measurement of transient PPIs plays a critical role in unraveling the complex machinery that cells employ to detect and respond to biological changes. Unlike stable PPIs that are detectable by biochemical methods such as co-immunoprecipitation and pull-down assays, transient PPIs require a much more sensitive methodology to investigate the binding. Biophysical methods including surface plasma resonance (SPR) improve the detection limit for understanding transient PPIs. However, the measurement of surface plasmon resonance (SPR) is based on the interactions between protein A immobilized (2D) on the surface and protein B flowing in the solution (3D). This interaction model (2D-3D) is not eligible to two dimensional PPIs (2D-2D), which constrain the movement of the interacting species along a 2D plane, similar to the case in many physiological processes.

Immunity requires further investigation for understanding the human defense system against pathogen infection, cancer, or autoimmune diseases. The great amount of intracellular and intercellular signal transduction constructs the entire immune signaling

network, in which 2D-2D PPIs play a significant role in cell-cell communications. Pathogen-induced adaptive immunity is a key component. The initiation of adaptive immunity generates more specific and efficient defense, and its regulation relates to allergy, vaccine development, autoimmune diseases, and some cancers. After the invasion of pathogens, antigen presenting cells (APCs) attack the invading pathogens, digest and present specific peptide segments on major histocompatibility complex (pMHC) on the cell membrane of APCs. The initiation of adaptive immune response begins with the 2D-2D interaction of pMHC on APCs and T cell receptor (TCR) on T cells. Therefore, the precise measurement of pMHC-TCR interaction is significant for ligand discrimination, self-recognition, and signal accumulation in immune response. pMHC-TCR across different cells can be measured with 2D-2D kinetics assays such as the micropipette adhesion frequency assay and biomembrane force probe (BFP),<sup>185</sup> developed by Zhu Laboratory, to probe the affinity and off-rate of PPIs while constraining the movement of proteins along a 2D plane. Zhu Laboratory demonstrated differences between the measurement of pMHC-TCR on two opposing membranes by BFP (2D-2D) and the measurement by SPR (2D-3D), contributing a more accurate way to predict T-cell proliferation by pMHC-TCR binding strength.<sup>89</sup>

The advent of methodologies has introduced a new complexity to the problem of investigating PPIs. Results obtained with different methods do not necessarily agree with one another. For instance, the Grove Laboratory used fluorescence co-localization to show 10-fold longer binding time of pMHC-TCR than that measured by BFP and micropipette adhesion frequency assay in Zhu Laboratory.<sup>27, 89</sup> Since the importance of understanding the primary recognition events in the immune response, there is an urgent

need to develop another methodology for measuring low-abundance bound complexes relative to overwhelming unbound proteins—the primary challenge in measuring transient PPIs.

Most common fluorescence methods for PPIs include FRET, FRAP, and FCS. FRET (mentioned in Chapter 1) only generates signals while two proteins are closer than one nanometer, but finding the good FRET pair without interfering PPIs can be time-consuming. FRAP monitors the binding events from fluorophore-tagged proteins by fitting the fluorescence recovery curves after photobleaching, but the fitting model requires careful calibration of a photobleaching profile.<sup>88</sup> Fluorescence fluctuations generate FCS curves including information of diffusion and binding, calibrated by easier control experiments than FRAP. To develop a general method without finding a FRET pair and calibration of a photobleaching profile, I have been focusing on FCS and FCCS measurements.

## **A.2 Results & Discussions**

Constructing supported lipid bilayers, Chenghao from Zhu Laboratory prepared biotinylated-pMHC-Cy5 on the lipid bilayers and T cells with TCR-CD3-TFP (mentioned in chapter 2). I aligned optics and performed single-point FCS/FCCS as well as Image FCS/FCCS experiments<sup>5, 141, 149-150, 161</sup> on this system (Figure A1). Unfortunately, the Image FCS (Figure A2) and FCCS (Figure A3) data all showed no obvious changes before and after T cells flowing into the imaging chambers similar to single-point FCS/FCCS, even with obvious TCR aggregation on T cells near the surface of bilayers.

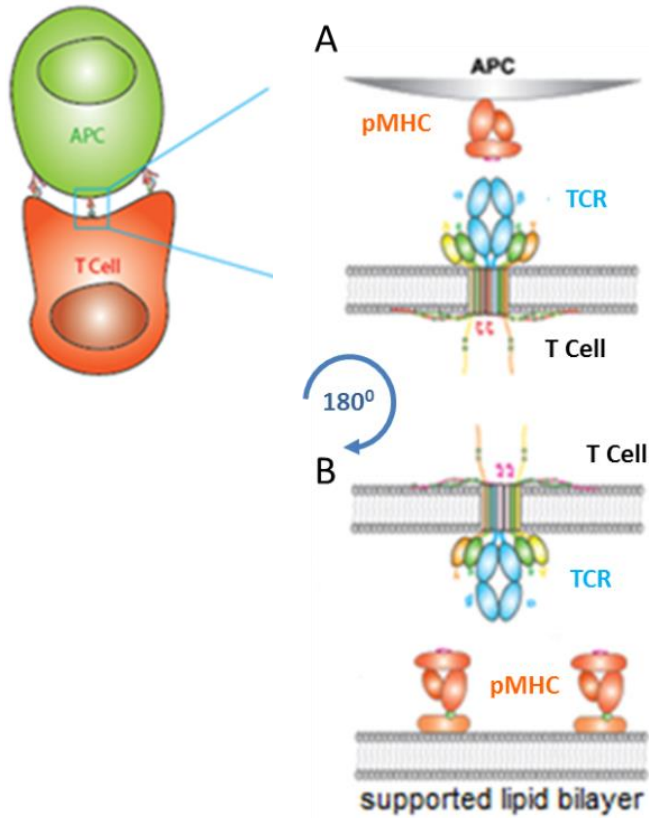


Figure A.1 T-cell response is triggered by a physical interaction with an APC (A) via pMHC binding to the TCR. (B) pMHC molecules are anchored on supported lipid bilayers to interact with TCR on T cells.

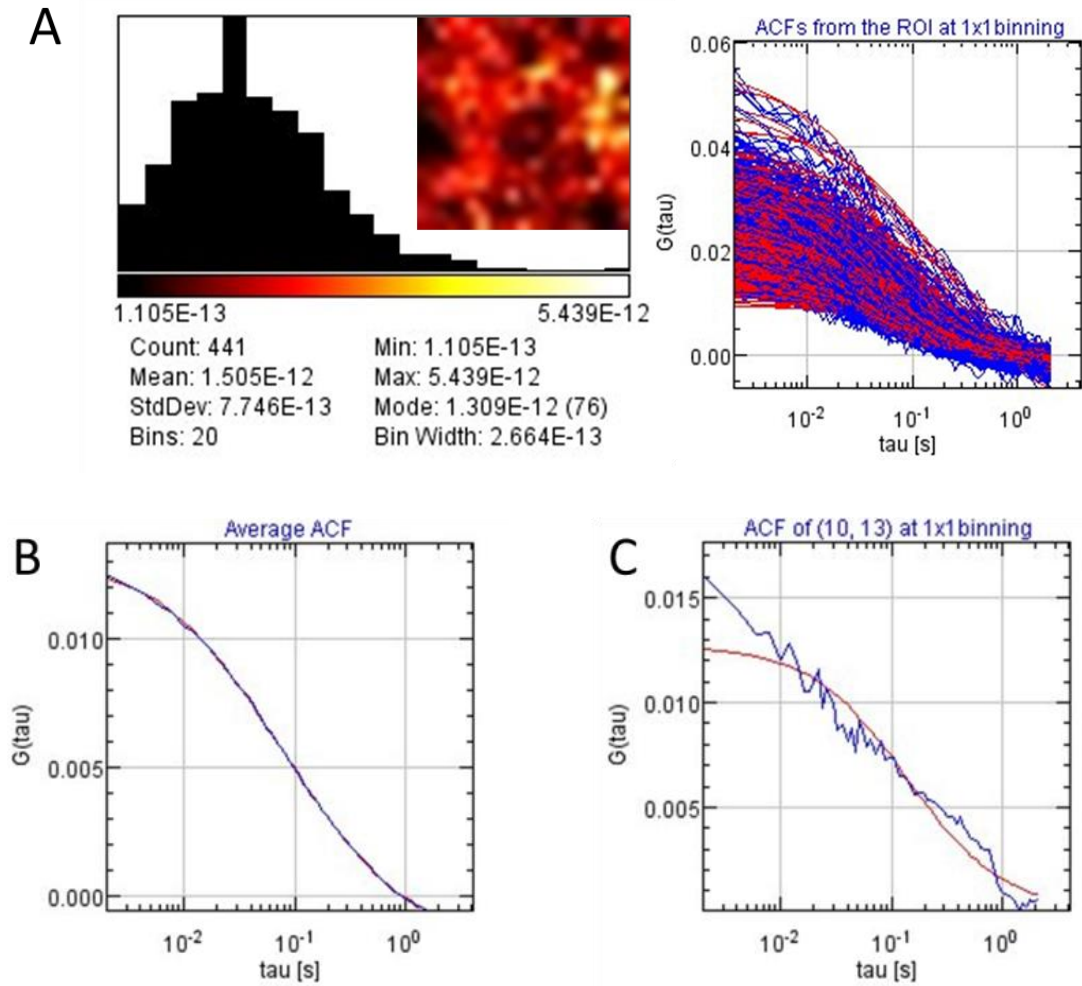


Figure A.2 Image FCS on supported lipid bilayers with pMHC-Cy5. (A) On a 21\*21 EMCCD pixel region, we acquire fluorescence time trace and calculate auto-correlation functions (ACF) with ImFCS (software developed by Wohland Laboratory, mentioned in Chapter 2),<sup>149-150, 161, 186</sup> which generates all 441 ACF curves and a histogram and map of fitted diffusion coefficients. (B) Either pMHC-Cy5 interacting with T cells or not shows similar average ACF curves. (C) Either pMHC-Cy5 interacting with T cells or not shows some (~5-10%) individual ACF curves with two populations. The fast component is ~0.01-0.1 second, and the slow one is ~0.1-1 second.

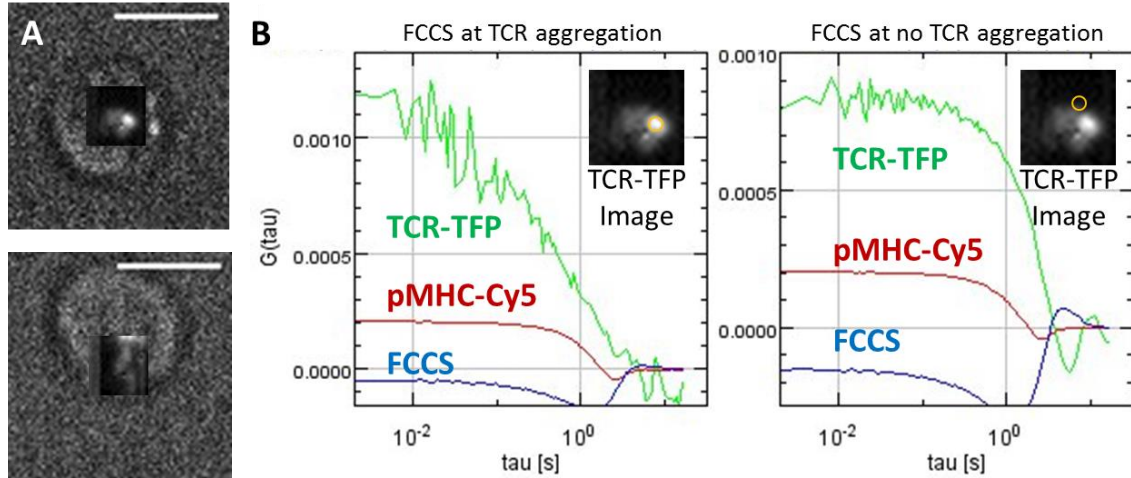


Figure A.3 Image FCCS between TCR-CD3-TFP on T cells and pMHC-Cy5 on supported lipid bilayers with total-internal-reflection 451 nm and wide-field 633 nm lasers illumination. (A) Bright-field T cell images overlap with TCR-CD3-TFP aggregation images. T cells with obvious TCR-CD3-TFP aggregation stay at the same position for over 5 minutes, while other T cells are more mobile. Scale bar: 10  $\mu\text{m}$ . (B) FCCS signals at the pixel with (left) or at the pixel without obvious TCR aggregation (right) are similar. The negative FCCS values and the dip around 1 second region are possible from the photobleaching correction.

- The reasons for undetectable binding signals can be: 1. Weak and undetectable PPIs,  
 2. Sample photobleaching.

### A.2.1 Weak PPIs: Low Binding Ratio

T cells continuously interact with different APCs and require the decision for initiation of adaptive immunity. Therefore, the binding of pMHC-TCR should not be too long and strong. pMHC-TCR binding constant from the Zhu Laboratory is around  $10^{-5} \mu\text{m}^2$ ,<sup>89</sup> which  $[\text{pMHC-TCR}]/[\text{pMHC}]_{\text{Total}}$  is less than 0.1 % when both pMHC and TCR are around 20-100 molecules per  $\mu\text{m}^2$ . The small binding ratio (<0.1 %) is undetectable since the binding events are hidden in the noise of FCCS. However, the undetectable binding events may prove the pMHC-TCR interaction is weak in contrast with FRET ( $\sim 10^{-2} \mu\text{m}^2$ )<sup>187</sup> and fluorescence co-localization experiments ( $k_{\text{off}}$  is slower than  $1 \text{ s}^{-1}$ ).<sup>27</sup>

### **A.2.2 Sample Photobleaching**

The signal-to-noise ratio of FCS and FCCS is proportional to the brightness of fluorophores,<sup>135</sup> so 100-1000 W/cm<sup>2</sup> is typical laser excitation intensity for FCS/FCCS measurement.<sup>46, 142-143</sup> However, proteins diffuse slowly ( $\sim 1 \mu\text{m}^2/\text{s}$ ) on membranes, and Image FCS/FCCS even illuminate the same fluorophore for more than 1 minute. This experimental setup will induce obvious photobleaching and require certain mathematical models for correction,<sup>163, 186</sup> including bi-exponential or polynomial models. However, barely observed binding signals may be removed from the correction of photobleaching. While no correction of photobleaching generates dominant correlation signals from photobleaching, the correction of photobleaching may eliminate cross-correlation of binding events. In addition, the photobleaching can kill the fluorophores before they bind to the binding partners from the small  $k_{\text{on}}$  ( $\sim 10^{-5} \mu\text{m}^2/\text{s}$ ).

### **A.3 Conclusion & Outlook**

Investigation of weak PPIs is essential for constructing signal transduction network in immunology for scientists to understand the regulation of self-defense. However, current fluorescent techniques still require improvement on detecting much smaller population of binding events. Unbinding/diffusing fluorophores are 1000-fold or even more than binding ones, which are too few to be detectable with current fluorescence methods. FRET is a way to isolate the binding signals based on the emission wavelength change of binding events, but it is time-consuming to find suitable FRET pairs in complex biological systems. The potential of SAFIRE by shifting the binding signals to modulated frequency can be another way to improve the detection limit of weak PPIs. Similar to chapter 3, the different residence time between binding proteins and unbinding

proteins labeled with PS-FPs can be discriminated. Utilization of dark state lifetimes in FPs suggests another way to enhance binding signals.

## REFERENCES

1. Wang, K.; Milkie, D. E.; Saxena, A.; Engerer, P.; Misgeld, T.; Bronner, M. E.; Mumm, J.; Betzig, E. Rapid Adaptive Optical Recovery of Optimal Resolution over Large Volumes. *Nat Methods* **2014**, *11*, 625-628.
2. Ji, N.; Sato, T. R.; Betzig, E. Characterization and Adaptive Optical Correction of Aberrations During in Vivo Imaging in the Mouse Cortex. *Proc. Natl. Acad. Sci. U.S.A.* **2012**, *109*, 22-27.
3. Dertinger, T.; Colyer, R.; Iyer, G.; Weiss, S.; Enderlein, J. Fast, Background-Free, 3d Super-Resolution Optical Fluctuation Imaging (Sofi). *Proc. Natl. Acad. Sci. U.S.A.* **2009**, *106*, 22287-22292.
4. Nakano, A. A Spinning-Disk Confocal Microscopy -- a Cutting-Edge Tool for Imaging of Membrane Traffic. *Cell Struct. Funct.* **2002**, *27*, 349-355.
5. Kannan, B.; Guo, L.; Sudhakaran, T.; Ahmed, S.; Maruyama, I.; Wohland, T. Spatially Resolved Total Internal Reflection Fluorescence Correlation Microscopy Using an Electron Multiplying Charge-Coupled Device Camera. *Anal. Chem.* **2007**, *79*, 4463-4470.
6. Miyauchi, K.; Kim, Y.; Latinovic, O.; Morozov, V.; Melikyan, G. B. HIV Enters Cells Via Endocytosis and Dynamin-Dependent Fusion with Endosomes. *Cell* **2009**, *137*, 433-44.
7. Low-Nam, S. T.; Lidke, K. A.; Cutler, P. J.; Roovers, R. C.; van Bergen en Henegouwen, P. M.; Wilson, B. S.; Lidke, D. S. Erbb1 Dimerization Is Promoted by Domain Co-Confinement and Stabilized by Ligand Binding. *Nature structural & molecular biology* **2011**, *18*, 1244-9.
8. Lin, W. C.; Iversen, L.; Tu, H. L.; Rhodes, C.; Christensen, S. M.; Iwig, J.; Hansen, S. D.; Huang, W. Y. C.; Groves, J. T. H-Ras Forms Dimers on Membrane Surfaces Via a Protein-Protein Interface. *Proc. Natl. Acad. Sci. U.S.A.* **2014**, *111*, 2996-3001.
9. Germain, R. N.; Robey, E. A.; Cahalan, M. D. A Decade of Imaging Cellular Motility and Interaction Dynamics in the Immune System. *Science* **2012**, *336*, 1676-81.
10. Elf, J.; Li, G. W.; Xie, X. S. Probing Transcription Factor Dynamics at the Single-Molecule Level in a Living Cell. *Science* **2007**, *316*, 1191-4.
11. Dragulescu-Andrasi, A.; Chan, C. T.; De, A.; Massoud, T. F.; Gambhir, S. S. Bioluminescence Resonance Energy Transfer (Bret) Imaging of Protein-Protein Interactions within Deep Tissues of Living Subjects. *Proc. Natl. Acad. Sci. U.S.A.* **2011**, *108*, 12060-12065.

12. Panchuk-Voloshina, N.; Haugland, R. P.; Bishop-Stewart, J.; Bhalgat, M. K.; Millard, P. J.; Mao, F.; Leung, W. Y.; Haugland, R. P. Alexa Dyes, a Series of New Fluorescent Dyes That Yield Exceptionally Bright, Photostable Conjugates. *J. Histochem. Cytochem.* **1999**, *47*, 1179-1188.
13. Yu, S. J.; Kang, M. W.; Chang, H. C.; Chen, K. M.; Yu, Y. C. Bright Fluorescent Nanodiamonds: No Photobleaching and Low Cytotoxicity. *J. Am. Chem. Soc.* **2005**, *127*, 17604-17605.
14. Umezawa, K.; Nakamura, Y.; Makino, H.; Citterio, D.; Suzuki, K. Bright, Color-Tunable Fluorescent Dyes in the Visible–near-Infrared Region. *J. Am. Chem. Soc.* **2008**, *130*, 1550-1551.
15. Grimm, J. B.; English, B. P.; Choi, H.; Muthusamy, A. K.; Mehl, B. P.; Dong, P.; Brown, T. A.; Lippincott-Schwartz, J.; Liu, Z.; Lionnet, T.; Lavis, L. D. Bright Photoactivatable Fluorophores for Single-Molecule Imaging. *Nat. Methods* **2016**, *13*, 985-988.
16. Shaner, N. C.; Lin, M. Z.; McKeown, M. R.; Steinbach, P. A.; Hazelwood, K. L.; Davidson, M. W.; Tsien, R. Y. Improving the Photostability of Bright Monomeric Orange and Red Fluorescent Proteins. *Nat Methods* **2008**, *5*, 545-51.
17. Betzig, E.; Patterson, G. H.; Sougrat, R.; Lindwasser, O. W.; Olenych, S.; Bonifacino, J. S.; Davidson, M. W.; Lippincott-Schwartz, J.; Hess, H. F. Imaging Intracellular Fluorescent Proteins at Nanometer Resolution. *Science* **2006**, *313*, 1642-1645.
18. Rust, M. J.; Bates, M.; Zhuang, X. Sub-Diffraction-Limit Imaging by Stochastic Optical Reconstruction Microscopy (Storm). *Nat. Methods* **2006**, *3*, 793-795.
19. Hell, S. W.; Wichmann, J. Breaking the Diffraction Resolution Limit by Stimulated Emission: Stimulated-Emission-Depletion Fluorescence Microscopy. *Opt. Lett.* **1994**, *19*, 780-782.
20. Hell, S. W. Far-Field Optical Nanoscopy. *Science* **2007**, *316*, 1153-1158.
21. Gustafsson, M. G. Nonlinear Structured-Illumination Microscopy: Wide-Field Fluorescence Imaging with Theoretically Unlimited Resolution. *Proc. Natl. Acad. Sci. U.S.A.* **2005**, *102*, 13081-6.
22. Kapanidis, A. N.; Lee, N. K.; Laurence, T. A.; Doose, S.; Margeat, E.; Weiss, S. Fluorescence-Aided Molecule Sorting: Analysis of Structure and Interactions by Alternating-Laser Excitation of Single Molecules. *Proc. Natl. Acad. Sci. U.S.A.* **2004**, *101*, 8936-41.
23. Sprague, B. L.; Pego, R. L.; Stavreva, D. A.; McNally, J. G. Analysis of Binding Reactions by Fluorescence Recovery after Photobleaching. *Biophys J* **2004**, *86*, 3473-95.

24. Slaughter, B. D.; Schwartz, J. W.; Li, R. Mapping Dynamic Protein Interactions in Map Kinase Signaling Using Live-Cell Fluorescence Fluctuation Spectroscopy and Imaging. *Proc Natl Acad Sci U S A* **2007**, *104*, 20320-5.
25. Yildiz, A. Single-Molecule Fluorescent Particle Tracking **2009**, 1-18.
26. Harris, T. H.; Banigan, E. J.; Christian, D. A.; Konradt, C.; Tait Wojno, E. D.; Norose, K.; Wilson, E. H.; John, B.; Weninger, W.; Luster, A. D.; Liu, A. J.; Hunter, C. A. Generalized Levy Walks and the Role of Chemokines in Migration of Effector Cd8+ T Cells. *Nature* **2012**, *486*, 545-8.
27. O'Donoghue, G. P.; Pielak, R. M.; Smoligovets, A. A.; Lin, J. J.; Groves, J. T. Direct Single Molecule Measurement of Tcr Triggering by Agonist Pmhc in Living Primary T Cells. *eLife* **2013**, *2*, e00778.
28. Jaqaman, K.; Loerke, D.; Mettlen, M.; Kuwata, H.; Grinstein, S.; Schmid, S. L.; Danuser, G. Robust Single-Particle Tracking in Live-Cell Time-Lapse Sequences. *Nat. Methods* **2008**, *5*, 695-702.
29. Bastiaens, P. I.; Jovin, T. M. Microspectroscopic Imaging Tracks the Intracellular Processing of a Signal Transduction Protein: Fluorescent-Labeled Protein Kinase C Beta I. *Proc. Natl. Acad. Sci. U.S.A.* **1996**, *93*, 8407-8412.
30. Lidke, D. S.; Nagy, P.; Heintzmann, R.; Arndt-Jovin, D. J.; Post, J. N.; Grecco, H. E.; Jares-Erijman, E. A.; Jovin, T. M. Quantum Dot Ligands Provide New Insights into Erbb/Her Receptor-Mediated Signal Transduction. *Nat. Biotechnol.* **2004**, *22*, 198-203.
31. Rambold, A. S.; Cohen, S.; Lippincott-Schwartz, J. Fatty Acid Trafficking in Starved Cells: Regulation by Lipid Droplet Lipolysis, Autophagy, and Mitochondrial Fusion Dynamics. *Dev Cell* **2015**, *32*, 678-92.
32. Tsien, R. Y. The Green Fluorescent Protein. *Annu. Rev. Biochem.* **1998**, *67*, 509-544.
33. Shaner, N. C.; Steinbach, P. A.; Tsien, R. Y. A Guide to Choosing Fluorescent Proteins. *Nat Methods* **2005**, *2*, 905-9.
34. Zimmer, M. Green Fluorescent Protein Application Structure and Related Photophysical Behavior. *Chem. Rev.* **2002**, *102*, 759-781.
35. Billinton, N.; Knight, A. W. Seeing the Wood through the Trees: A Review of Techniques for Distinguishing Green Fluorescent Protein from Endogenous Autofluorescence. *Anal. Biochem.* **2001**, *291*, 175-197.
36. Giepmans, B. N. G.; Adams, S. R.; Ellisman, M. H.; Tsien, R. Y. The Fluorescent Toolbox for Assessing Protein Location and Function. *Science* **2006**, *312*, 217-224.

37. Miyawaki, A.; Shcherbakova, D. M.; Verkhusha, V. V. Red Fluorescent Proteins: Chromophore Formation and Cellular Applications. *Curr. Opin. Struct. Biol.* **2012**, *22*, 679-688.
38. Marriott, G.; Mao, S.; Sakata, T.; Ran, J.; Jackson, D. K.; Petchprayoon, C.; Gomez, T. J.; Warp, E.; Tulyathan, O.; Aaron, H. L.; Isacoff, E. Y.; Yan, Y. Optical Lock-in Detection Imaging Microscopy for Contrast-Enhanced Imaging in Living Cells. *Proc. Natl. Acad. Sci. U.S.A.* **2008**, *105*, 17789-17794.
39. Mao, S.; Benninger, R. K.; Yan, Y.; Petchprayoon, C.; Jackson, D.; Easley, C. J.; Piston, D. W.; Marriott, G. Optical Lock-in Detection of FRET Using Synthetic and Genetically Encoded Optical Switches. *Biophys J* **2008**, *94*, 4515-24.
40. Du, G.; Marriott, G.; Yan, Y. An Improved Optical Lock-in Detection Method for Contrast-Enhanced Imaging in Living Cells. *Bioinform. Biomed. Eng. (iCBBE), 2010 4th International Conference* **2010**, 1-5.
41. Yan, Y.; Marriott, M. E.; Petchprayoon, C.; Marriott, G. Optical Switch Probes and Optical Lock-in Detection (Olid) Imaging Microscopy: High-Contrast Fluorescence Imaging within Living Systems. *Biochem J* **2011**, *433*, 411-22.
42. Querard, J.; Markus, T. Z.; Plamont, M. A.; Gauron, C.; Wang, P.; Espagne, A.; Volovitch, M.; Vriza, S.; Croquette, V.; Gautier, A.; Le Saux, T.; Jullien, L. Photoswitching Kinetics and Phase-Sensitive Detection Add Discriminative Dimensions for Selective Fluorescence Imaging. *Angew. Chem. Int. Ed.* **2015**, *54*, 2633-2637.
43. Richards, C. I.; Hsiang, J. C.; Senapati, D.; Patel, S.; Yu, J. H.; Vosch, T.; Dickson, R. M. Optically Modulated Fluorophores for Selective Fluorescence Signal Recovery. *J. Am. Chem. Soc.* **2009**, *131*, 4619-4621.
44. Richards, C. I.; Hsiang, J. C.; Dickson, R. M. Synchronously Amplified Fluorescence Image Recovery (Safire). *J. Phys. Chem. B* **2010**, *114*, 660-665.
45. Petty, J. T.; Fan, C.; Story, S. P.; Sengupta, B.; Sartin, M.; Hsiang, J. C.; Perry, J. W.; Dickson, R. M. Optically Enhanced, near-Ir, Silver Cluster Emission Altered by Single Base Changes in the DNA Template. *J. Phys. Chem. B* **2011**, *115*, 7996-8003.
46. Fan, C.; Hsiang, J. C.; Dickson, R. M. Optical Modulation and Selective Recovery of Cy5 Fluorescence. *ChemPhysChem* **2012**, *13*, 1023-1029.
47. Mahoney, D. P.; Owens, E. A.; Fan, C.; Hsiang, J. C.; Henary, M. M.; Dickson, R. M. Tailoring Cyanine Dark States for Improved Optically Modulated Fluorescence Recovery. *J Phys Chem B* **2015**, *119*, 4637-43.

48. Jablonski, A. E.; Hsiang, J. C.; Bagchi, P.; Hull, N.; Richards, C. I.; Fahrni, C. J.; Dickson, R. M. Signal Discrimination between Fluorescent Proteins in Live Cells by Long-Wavelength Optical Modulation. *J. Phys. Chem. Lett.* **2012**, *3*, 3585-3591.
49. Jablonski, A. E.; Vegh, R. B.; Hsiang, J. C.; Bommarius, B.; Chen, Y. C.; Solntsev, K. M.; Bommarius, A. S.; Tolbert, L. M.; Dickson, R. M. Optically Modulatable Blue Fluorescent Proteins. *J. Am. Chem. Soc.* **2013**, *135*, 16410-16417.
50. Chen, Y. C.; Jablonski, A. E.; Issaeva, I.; Bourassa, D.; Hsiang, J. C.; Fahrni, C. J.; Dickson, R. M. Optically Modulated Photoswitchable Fluorescent Proteins Yield Improved Biological Imaging Sensitivity. *J. Am. Chem. Soc.* **2015**, *137*, 12764-12767.
51. Chen, Y. C.; Dickson, R. M. Improved Fluorescent Protein Contrast and Discrimination by Optically Controlling Dark State Lifetimes. *J. Phys. Chem. Lett.* **2017**, *8*, 733-736.
52. Gest, H. The Discovery of Microorganisms by Robert Hooke and Antoni Van Leeuwenhoek, Fellows of the Royal Society. *Notes Rec. R. Soc. Lond.* **2004**, *58*, 187-201.
53. Ernst Abbe (Wikipedia). [https://en.wikipedia.org/wiki/Ernst\\_Abbe](https://en.wikipedia.org/wiki/Ernst_Abbe) (accessed July 26, 2017).
54. Köhler, A. Ein Neues Beleuchtungsverfahren Für Mikrographische Zwecke. *Zeitschrift für wissenschaftliche Mikroskopie und für Mikroskopische Technik* **1893**, *10*, 433-440.
55. Optical Microscope (Wikipedia). [https://en.wikipedia.org/wiki/Optical\\_microscope](https://en.wikipedia.org/wiki/Optical_microscope) (accessed July 26, 2017).
56. Sahagún, B. d. Historia General De Las Cosas De La Nueva España (1560–1564) **1560**.
57. Stokes, G. G. On the Change of Refrangibility of Light. *Phil. Trans. R. Soc. Lond.* **1852**, *142*, 463-562.
58. Valeur, B.; Berberan-Santos, M. r. N. A Brief History of Fluorescence and Phosphorescence before the Emergence of Quantum Theory. *J. Chem. Educ.* **2011**, *88*, 731-738.
59. Lakowicz, J. R. *Principles of Fluorescence Spectroscopy*. Third ed.; Springer: 2006.
60. Jabłoński, A. Efficiency of Anti-Stokes Fluorescence in Dyes. *Nature* **1933**, *131*, 839-840.

61. Dickson, R. M.; Cubitt, A. B.; Tsien, R. Y.; Moerner, W. E. On/Off Blinking and Switching Behavior of Single Molecules of Green Fluorescent Protein. *Nature* **1997**, *388*, 355-358.
62. Spring, K. R.; Davidson, M. W. Introduction to Fluorescence Microscopy. <https://www.microscopyu.com/techniques/fluorescence/introduction-to-fluorescence-microscopy> (accessed July 27, 2017).
63. Masters, B. R. The Development of Fluorescence Microscopy. *eLS* **2010**.
64. Ploem, J. S. Die Möglichkeit Der Auflichtfluoreszenzmethoden Bei Untersuchungen Von Zellen in Durchströmungskammern Und Leightonröhren. Xth Symposium D. Gesellschaft F. Histochemie 1965. *Acta Histochem. Suppl.* **1967**, *7*, 339-343.
65. Paddock, S. Confocal Laser Scanning Light Microscopy. *eLS* **2001**, 1-6.
66. Denk, W.; Strickler, J. H.; Webb, W. W. Two-Photon Laser Scanning Fluorescence Microscopy. *Science* **1990**, *248*, 73-76.
67. Gao, L.; Shao, L.; Chen, B. C.; Betzig, E. 3d Live Fluorescence Imaging of Cellular Dynamics Using Bessel Beam Plane Illumination Microscopy. *Nat Protoc* **2014**, *9*, 1083-101.
68. Toomre, D. K.; Langhorst, M. F.; Davidson, M. W. Introduction to Spinning Disk Confocal Microscopy. <http://zeiss-campus.magnet.fsu.edu/articles/spinningdisk/introduction.html> (accessed July 27, 2017).
69. Inoue, S.; Inoue, T. Direct-View High-Speed Confocal Scanner: Csu-10. *Methods Cell Biol.* **2003**, *70*.
70. Adams, M. C.; Salmon, W. C.; Gupton, S. L.; Cohan, C. S.; Wittmann, T.; Prigozhina, N.; Waterman-Storer, C. M. A High-Speed Multispectral Spinning-Disk Confocal Microscope System for Fluorescent Speckle Microscopy of Living Cells. *Methods* **2003**, *29*, 29-41.
71. Egeblad, M.; Ewald, A. J.; Askautrud, H. A.; Truitt, M. L.; Welm, B. E.; Bainbridge, E.; Peeters, G.; Krummel, M. F.; Werb, Z. Visualizing Stromal Cell Dynamics in Different Tumor Microenvironments by Spinning Disk Confocal Microscopy. *Dis. Model. Mech.* **2008**, *1*, 155-67.
72. Needleman, D. J.; Xu, Y.; Mitchison, T. J. Pin-Hole Array Correlation Imaging: Highly Parallel Fluorescence Correlation Spectroscopy. *Biophys. J.* **2009**, *96*, 5050-5059.
73. Schermelleh, L.; Heintzmann, R.; Leonhardt, H. A Guide to Super-Resolution Fluorescence Microscopy. *J. Cell Biol.* **2010**, *190*, 165-175.

74. Super-Resolved Fluorescence Microscopy, Scientific Background on the Nobel Prize in Chemistry 2014. [https://www.nobelprize.org/nobel\\_prizes/chemistry/laureates/2014/advanced-chemistryprize2014.pdf](https://www.nobelprize.org/nobel_prizes/chemistry/laureates/2014/advanced-chemistryprize2014.pdf) (accessed July 31, 2017).
75. Klar, T. A.; Jakobs, S.; Dyba, M.; Egner, A.; Hell, S. W. Fluorescence Microscopy with Diffraction Resolution Barrier Broken by Stimulated Emission. *Proc. Natl. Acad. Sci. U.S.A.* **2000**, *97*, 8206-8210.
76. Permyakov, E. A. *Luminescent Spectroscopy of Proteins*. CRC Press: 1992.
77. Rocheleau, J. V.; Head, W. S.; Piston, D. W. Quantitative Nad(P)H/Flavoprotein Autofluorescence Imaging Reveals Metabolic Mechanisms of Pancreatic Islet Pyruvate Response. *J Biol Chem* **2004**, *279*, 31780-7.
78. Baeyer, A. Uber Ein Neue Klasse Von Farbstoffen (on a New Class of Dyes). *Berichte der Deutschen chemischen Gesellschaft zu Berlin* **1871**, *4*, 555-558.
79. Lavis, L. D.; Raines, R. T. Bright Ideas for Chemical Biology. *ACS Chem. Biol.* **2008**, *3*, 142–155.
80. Resch-Genger, U.; Grabolle, M.; Cavaliere-Jaricot, S.; Nitschke, R.; Nann, T. Quantum Dots Versus Organic Dyes as Fluorescent Labels. *Nat. Methods* **2008**, *5*, 763-75.
81. The Green Fluorescent Protein: Discovery, Expression and Development. [https://www.nobelprize.org/nobel\\_prizes/chemistry/laureates/2008/advanced-chemistryprize2008.pdf](https://www.nobelprize.org/nobel_prizes/chemistry/laureates/2008/advanced-chemistryprize2008.pdf) (accessed August 1, 2017).
82. Ashdown, G. W.; Burn, G. L.; Williamson, D. J.; Pandzic, E.; Peters, R.; Holden, M.; Ewers, H.; Shao, L.; Wiseman, P. W.; Owen, D. M. Live-Cell Super-Resolution Reveals F-Actin and Plasma Membrane Dynamics at the T Cell Synapse. *Biophys J* **2017**, *112*, 1703-1713.
83. Yu, C. H.; Wu, H. J.; Kaizuka, Y.; Vale, R. D.; Groves, J. T. Altered Actin Centripetal Retrograde Flow in Physically Restricted Immunological Synapses. *PLoS One* **2010**, *5*, e11878.
84. Sood, C.; Marin, M.; Mason, C. S.; Melikyan, G. B. Visualization of Content Release from Cell Surface-Attached Single Hiv-1 Particles Carrying an Extra-Viral Fluorescent Ph-Sensor. *PLoS One* **2016**, *11*, e0148944.
85. Lippincott-Schwartz, J.; Snapp, E.; Kenworthy, A. Studying Protein Dynamics in Living Cells. *Nat. Rev. Mol. Cell Biol.* **2001**, *2*, 444-456.
86. Stoevesandt, O.; Brock, R. One-Step Analysis of Protein Complexes in Microliters of Cell Lysate Using Indirect Immunolabeling & Fluorescence Cross-Correlation Spectroscopy. *Nat. Protoc.* **2006**, *1*, 223-229.

87. Sprague, B. L.; Muller, F.; Pego, R. L.; Bungay, P. M.; Stavreva, D. A.; McNally, J. G. Analysis of Binding at a Single Spatially Localized Cluster of Binding Sites by Fluorescence Recovery after Photobleaching. *Biophys J* **2006**, *91*, 1169-91.
88. Mueller, F.; Wach, P.; McNally, J. G. Evidence for a Common Mode of Transcription Factor Interaction with Chromatin as Revealed by Improved Quantitative Fluorescence Recovery after Photobleaching. *Biophys J* **2008**, *94*, 3323-39.
89. Huang, J.; Zarnitsyna, V. I.; Liu, B.; Edwards, L. J.; Jiang, N.; Evavold, B. D.; Zhu, C. The Kinetics of Two-Dimensional Tcr and Pmhc Interactions Determine T-Cell Responsiveness. *Nature* **2010**, *464*, 932-6.
90. Benítez, J. J.; Keller, A. M.; Chen, P. Nanovesicle Trapping for Studying Weak Protein Interactions by Single-Molecule FRET **2010**, *472*, 41-60.
91. Kim, S. A.; Heinze, K. G.; Bacia, K.; Waxham, M. N.; Schwille, P. Two-Photon Cross-Correlation Analysis of Intracellular Reactions with Variable Stoichiometry. *Biophys J* **2005**, *88*, 4319-36.
92. Thews, E.; Gerken, M.; Eckert, R.; Zapfel, J.; Tietz, C.; Wrachtrup, J. Cross Talk Free Fluorescence Cross Correlation Spectroscopy in Live Cells. *Biophys J* **2005**, *89*, 2069-76.
93. Shimomura, O.; Johnson, F. H.; Saiga, Y. Extraction, Purification and Properties of Aequorin, a Bioluminescent Protein from the Luminous Hydromedusan, Aequorea. *J. Cell. Comp. Physiol.* **1962**, *59*, 223-240.
94. Chalfie, M.; Tu, Y.; Euskirchen, G.; Ward, W. W.; Prasher, D. C. Green Fluorescent Protein as a Marker for Gene Expression. *Science* **1994**, *263*, 802-805.
95. Heim, R.; Prasher, D. C.; Tsien, R. Y. Wavelength Mutations and Posttranslational Autoxidation of Green Fluorescent Protein. *Proc. Natl. Acad. Sci. U.S.A.* **1994**, *91*, 12501-12504.
96. Yang, F.; Moss, L. G.; Phillips, G. N., Jr. The Molecular Structure of Green Fluorescent Protein. *Nat. Biotechnol.* **1996**, *14*, 1246-1251.
97. Ormö, M.; Cubitt, A. B.; Kallio, K.; Gross, L. A.; Tsien, R. Y.; Remington, S. J. Crystal Structure of the Aequorea Victoria Green Fluorescent Protein. *Science* **1996**, *273*, 1392-1395.
98. Lukyanov, K. A.; Fradkov, A. F.; Gurskaya, N. G.; Matz, M. V.; Labas, Y. A.; Savitsky, A. P.; Markelov, M. L.; Zaraisky, A. G.; Zhao, X.; Fang, Y.; Tan, W.; Lukyanov, S. A. Natural Animal Coloration Can Be Determined by a Nonfluorescent Green Fluorescent Protein Homolog. *J. Biol. Chem.* **2000**, *275*, 25879-25882.

99. Ando, R.; Mizuno, H.; Miyawaki, A. Regulated Fast Nucleocytoplasmic Shuttling Observed by Reversible Protein Highlighting. *Science* **2004**, *306*, 1370-1373.
100. Stiel, A. C.; Trowitzsch, S.; Weber, G.; Andresen, M.; Eggeling, C.; Hell, S. W.; Jakobs, S.; Wahl, M. C. 1.8 a Bright-State Structure of the Reversibly Switchable Fluorescent Protein Dronpa Guides the Generation of Fast Switching Variants. *Biochem. J.* **2007**, *402*, 35-42.
101. Dedecker, P.; Mo, G. C.; Dertinger, T.; Zhang, J. Widely Accessible Method for Superresolution Fluorescence Imaging of Living Systems. *Proc. Natl. Acad. Sci. U.S.A.* **2012**, *109*, 10909-10914.
102. Hofmann, M.; Eggeling, C.; Jakobs, S.; Hell, S. W. Breaking the Diffraction Barrier in Fluorescence Microscopy at Low Light Intensities by Using Reversibly Photoswitchable Proteins. *Proc. Natl. Acad. Sci. U.S.A.* **2005**, *102*, 17565-17569.
103. Andresen, M.; Stiel, A. C.; Trowitzsch, S.; Weber, G.; Eggeling, C.; Wahl, M. C.; Hell, S. W.; Jakobs, S. Structural Basis for Reversible Photoswitching in Dronpa. *Proc. Natl. Acad. Sci. U.S.A.* **2007**, *104*, 13005-13009.
104. Heim, R.; Cubitt, A. B.; Tsien, R. Y. Improved Green Fluorescence. *Nature* **1995**, *373*, 663-664.
105. Chattoraj, M.; King, B. A.; Bublitz, G. U.; Boxer, S. G. Ultra-Fast Excited State Dynamics in Green Fluorescent Protein: Multiple States and Proton Transfer. *Proc. Natl. Acad. Sci. U.S.A.* **1996**, *93*, 8362-8367.
106. Shu, X.; Leiderman, P.; Gepshtein, R.; Smith, N. R.; Kallio, K.; Huppert, D.; Remington, S. J. An Alternative Excited-State Proton Transfer Pathway in Green Fluorescent Protein Variant S205v. *Protein Sci* **2007**, *16*, 2703-10.
107. Chudakov, D. M.; Feofanov, A. V.; Mudrik, N. N.; Lukyanov, S.; Lukyanov, K. A. Chromophore Environment Provides Clue to "Kindling Fluorescent Protein" Riddle. *J Biol Chem* **2003**, *278*, 7215-9.
108. Yadav, D.; Lacombe, F.; Dozova, N.; Rappaport, F.; Plaza, P.; Espagne, A. Real-Time Monitoring of Chromophore Isomerization and Deprotonation During the Photoactivation of the Fluorescent Protein Dronpa. *J. Phys. Chem. B* **2015**, *119*, 2404-2414.
109. Tiwari, D. K.; Arai, Y.; Yamanaka, M.; Matsuda, T.; Agetsuma, M.; Nakano, M.; Fujita, K.; Nagai, T. A Fast- and Positively Photoswitchable Fluorescent Protein for Ultralow-Laser-Power Resolft Nanoscopy. *Nat. Methods* **2015**, *12*, 515-8.
110. Brakemann, T.; Weber, G.; Andresen, M.; Groenhof, G.; Stiel, A. C.; Trowitzsch, S.; Eggeling, C.; Grubmuller, H.; Hell, S. W.; Wahl, M. C.; Jakobs, S. Molecular Basis of the Light-Driven Switching of the Photochromic Fluorescent Protein Padron. *J Biol Chem* **2010**, *285*, 14603-9.

111. Sinnecker, D.; Voigt, P.; Hellwig, N.; Schaefer, M. Reversible Photobleaching of Enhanced Green Fluorescent Proteins. *Biochemistry* **2005**, *44*, 7085–7094.
112. Jablonski, A. E. *Optically Modulated Fluorescent Proteins*. Georgia Institute of Technology, Georgia Institute of Technology, 2014.
113. Pletneva, N. V.; Pletnev, V. Z.; Lukyanov, K. A.; Gurskaya, N. G.; Goryacheva, E. A.; Martynov, V. I.; Wlodawer, A.; Dauter, Z.; Pletnev, S. Structural Evidence for a Dehydrated Intermediate in Green Fluorescent Protein Chromophore Biosynthesis. *J Biol Chem* **2010**, *285*, 15978-84.
114. Shaner, N. C.; Campbell, R. E.; Steinbach, P. A.; Giepmans, B. N.; Palmer, A. E.; Tsien, R. Y. Improved Monomeric Red, Orange and Yellow Fluorescent Proteins Derived from *Discosoma* Sp. Red Fluorescent Protein. *Nat Biotechnol* **2004**, *22*, 1567-72.
115. Mizuno, H.; Mal, T. K.; Walchli, M.; Kikuchi, A.; Fukano, T.; Ando, R.; Jeyakanthan, J.; Taka, J.; Shiro, Y.; Ikura, M.; Miyawaki, A. Light-Dependent Regulation of Structural Flexibility in a Photochromic Fluorescent Protein. *Proc Natl Acad Sci U S A* **2008**, *105*, 9227-32.
116. Acharya, A.; Bogdanov, A. M.; Grigorenko, B. L.; Bravaya, K. B.; Nemukhin, A. V.; Lukyanov, K. A.; Krylov, A. I. Photoinduced Chemistry in Fluorescent Proteins: Curse or Blessing? *Chem Rev* **2017**, *117*, 758-795.
117. Vegh, R. B.; Bravaya, K. B.; Bloch, D. A.; Bommarius, A. S.; Tolbert, L. M.; Verkhovsky, M.; Krylov, A. I.; Solntsev, K. M. Chromophore Photoreduction in Red Fluorescent Proteins Is Responsible for Bleaching and Phototoxicity. *J Phys Chem B* **2014**, *118*, 4527-34.
118. Brakemann, T.; Stiel, A. C.; Weber, G.; Andresen, M.; Testa, I.; Grotjohann, T.; Leutenegger, M.; Plessmann, U.; Urlaub, H.; Eggeling, C.; Wahl, M. C.; Hell, S. W.; Jakobs, S. A Reversibly Photoswitchable Gfp-Like Protein with Fluorescence Excitation Decoupled from Switching. *Nat Biotechnol* **2011**, *29*, 942-7.
119. Habuchi, S.; Cotlet, M.; Gensch, T.; Bednarz, T.; Haber-Pohlmeier, S.; Rozenski, J.; Dirix, G.; Michiels, J.; Vanderleyden, J.; Heberle, J.; Schryver, F. C. D.; Hofkens, J. Evidence for the Isomerization and Decarboxylation in the Photoconversion of the Red Fluorescent Protein Dsred. *J. Am. Chem. Soc.* **2005**, *127*, 8977-84.
120. Miyawaki, A.; Llopis, J.; Heim, R.; McCaffery, J. M.; Adams, J. A.; Ikura, M.; Tsien, R. Y. Fluorescent Indicators for Ca<sup>2+</sup>-Based on Green Fluorescent Proteins and Calmodulin. *Nature* **1997**, *388*, 882-887.
121. Nakai, J.; Ohkura, M.; Imoto, K. A High Signal-to-Noise Ca(2+) Probe Composed of a Single Green Fluorescent Protein. *Nat. Biotechnol.* **2001**, *19*, 137-141.

122. Qiao, W.; Mooney, M.; Bird, A. J.; Winge, D. R.; Eide, D. J. Zinc Binding to a Regulatory Zinc-Sensing Domain Monitored in Vivo by Using FRET. *Proc. Natl. Acad. Sci. U.S.A.* **2006**, *103*, 8674-8679.
123. Dittmer, P. J.; Miranda, J. G.; Gorski, J. A.; Palmer, A. E. Genetically Encoded Sensors to Elucidate Spatial Distribution of Cellular Zinc. *J. Biol. Chem.* **2009**, *284*, 16289-16297.
124. Dooley, C. T.; Dore, T. M.; Hanson, G. T.; Jackson, W. C.; Remington, S. J.; Tsien, R. Y. Imaging Dynamic Redox Changes in Mammalian Cells with Green Fluorescent Protein Indicators. *J. Biol. Chem.* **2004**, *279*, 22284-22293.
125. Germond, A.; Fujita, H.; Ichimura, T.; Watanabe, T. M. Design and Development of Genetically Encoded Fluorescent Sensors to Monitor Intracellular Chemical and Physical Parameters. *Biophys Rev* **2016**, *8*, 121-138.
126. Siegel, M. S.; Isacoff, E. Y. A Genetically Encoded Optical Probe of Membrane Voltage. *Neuron* **1997**, *19*, 735-741.
127. Guerrero, G.; Siegel, M. S.; Roska, B.; Loots, E.; Isacoff, E. Y. Tuning Flash: Redesign of the Dynamics, Voltage Range, and Color of the Genetically Encoded Optical Sensor of Membrane Potential. *Biophys. J.* **2002**, *83*, 3607-3618.
128. Axelrod, D.; Kopeel, D. E.; Elson, E.; Webb, W. W. Mobility Measurement by Analysis of Fluorescence Photobleaching Recovery Kinetics. *Biophys. J.* **1976**, *16*, 1055-1069.
129. Edidin, M. Rotational and Translational Diffusion in Membranes. *Annu. Rev. Biophys. Bioeng.* **1974**, *3*, 179-201.
130. Daddysman, M. K.; Fecko, C. J. Revisiting Point Frap to Quantitatively Characterize Anomalous Diffusion in Live Cells. *J Phys Chem B* **2013**, *117*, 1241-51.
131. Reid, G.; Hübner, M. R.; Métivier, R.; Brand, H.; Denger, S.; Manu, D.; Beaudouin, J.; Ellenberg, J.; Gannon, F. Cyclic, Proteasome-Mediated Turnover of Unliganded and Liganded Era on Responsive Promoters Is an Integral Feature of Estrogen Signaling. *Mol. Cell* **2003**, *11*, 695-707.
132. Schwille, P.; Hausteiner, E. Fluorescence Correlation Spectroscopy- an Introduction to Its Concepts and Applications. <http://www.biophysics.org/portals/1/pdfs/education/schwille.pdf> (accessed March 22, 2012).
133. Elson, E. L. Fluorescence Correlation Spectroscopy. I. Conceptual Basis and Theory. *Biopolymers* **1974**, *13*, 1-27.

134. Koppel, D. E. Statistical Accuracy in Fluorescence Correlation Spectroscopy. *Phys. Rev. A* **1974**, *10*, 1938-1945.
135. Krichevsky, O.; Bonnet, G. Fluorescence Correlation Spectroscopy: The Technique and Its Applications. *Rep. Prog. Phys.* **2002**, *65*, 251-297.
136. Briddon, S. J.; Middleton, R. J.; Yates, A. S.; George, M. W.; Kellam, B.; Hill, S. J. Application of Fluorescence Correlation Spectroscopy to the Measurement of Agonist Binding to a G-Protein Coupled Receptor at the Single Cell Level. *Faraday Discuss.* **2004**, *126*, 197.
137. Michelman-Ribeiro, A.; Mazza, D.; Rosales, T.; Stasevich, T. J.; Boukari, H.; Rishi, V.; Vinson, C.; Knutson, J. R.; McNally, J. G. Direct Measurement of Association and Dissociation Rates of DNA Binding in Live Cells by Fluorescence Correlation Spectroscopy. *Biophys J* **2009**, *97*, 337-46.
138. Elson, E. L. Fluorescence Correlation Spectroscopy: Past, Present, Future. *Biophys J* **2011**, *101*, 2855-70.
139. He, J.; Guo, S. M.; Bathe, M. Bayesian Approach to the Analysis of Fluorescence Correlation Spectroscopy Data I: Theory. *Anal Chem* **2012**, *84*, 3871-9.
140. Guo, S. M.; He, J.; Monnier, N.; Sun, G.; Wohland, T.; Bathe, M. Bayesian Approach to the Analysis of Fluorescence Correlation Spectroscopy Data II: Application to Simulated and in Vitro Data. *Anal Chem* **2012**, *84*, 3880-8.
141. Guo, S. M.; Bag, N.; Mishra, A.; Wohland, T.; Bathe, M. Bayesian Total Internal Reflection Fluorescence Correlation Spectroscopy Reveals Hiapp-Induced Plasma Membrane Domain Organization in Live Cells. *Biophys J* **2014**, *106*, 190-200.
142. Triffo, S. B.; Huang, H. H.; Smith, A. W.; Chou, E. T.; Groves, J. T. Monitoring Lipid Anchor Organization in Cell Membranes by Pie-Fccs. *J. Am. Chem. Soc.* **2012**, *134*, 10833-42.
143. Schwille, P.; Kummer, S.; Heikal, A. A.; Moerner, W. E.; Webb, W. W. Fluorescence Correlation Spectroscopy Reveals Fast Optical Excitation-Driven Intramolecular Dynamics of Yellow Fluorescent Proteins. *Proc. Natl. Acad. Sci. U.S.A.* **2000**, *97*, 151-156.
144. Schwille, P.; Meyer-Almes, F. J.; Rigler, R. Dual-Color Fluorescence Cross-Correlation Spectroscopy for Multicomponent Diffusional Analysis in Solution **1997**, *72*, 1878-1886.
145. Bacia, K.; Schwille, P. Practical Guidelines for Dual-Color Fluorescence Cross-Correlation Spectroscopy. *Nat. Protoc.* **2007**, *2*, 2842-2856.

146. Garcia-Saez, A. J.; Ries, J.; Orzaez, M.; Perez-Paya, E.; Schwille, P. Membrane Promotes Tbid Interaction with Bcl(XI). *Nature structural & molecular biology* **2009**, *16*, 1178-85.
147. Perroud, T. D.; Huang, B.; Wallace, M. I.; Zare, R. N. Photon Counting Histogram for One-Photon Excitation. *ChemPhysChem* **2003**, *4*, 1121-3.
148. Muller, J. D. Cumulant Analysis in Fluorescence Fluctuation Spectroscopy. *Biophys J* **2004**, *86*, 3981-92.
149. Sankaran, J.; Shi, X.; Ho, L. Y.; Stelzer, E. H. K.; Wohland, T. Imfcs: A Software for Imaging Fcs Data Analysis and Visualization. *Opt Express* **2010**, *18*, 25468-25481.
150. Sankaran, J.; Bag, N.; Kraut, R. S.; Wohland, T. Accuracy and Precision in Camera-Based Fluorescence Correlation Spectroscopy Measurements. *Anal. Chem.* **2013**, *85*, 3948-3954.
151. Sisan, D. R.; Arevalo, R.; Graves, C.; McAllister, R.; Urbach, J. S. Spatially Resolved Fluorescence Correlation Spectroscopy Using a Spinning Disk Confocal Microscope. *Biophys J* **2006**, *91*, 4241-52.
152. Burkhardt, M.; Schwille, P. Electron Multiplying Ccd Based Detection for Spatially Resolved Fluorescence Correlation Spectroscopy. *Opt Express* **2006**, *14*, 5013-5020.
153. Campbell, R. E.; Tour, O.; Palmer, A. E.; Steinbach, P. A.; Baird, G. S.; Zacharias, D. A.; Tsien, R. Y. A Monomeric Red Fluorescent Protein. *Proc. Natl. Acad. Sci. U.S.A.* **2002**, *99*, 7877-7782.
154. Jabłoński, A.; Hsiang, J. C.; Fahrni, C. J.; Dickson, R. M. Protein Dynamics (R01 Proposal). 2012.
155. Zhang, Y.; Ge, C.; Zhu, C.; Salaita, K. DNA-Based Digital Tension Probes Reveal Integrin Forces During Early Cell Adhesion. *Nat. Commun.* **2014**, *5*, 5167.
156. Cole, D. K.; Bulek, A. M.; Dolton, G.; Schauenberg, A. J.; Szomolay, B.; Rittase, W.; Trimby, A.; Jothikumar, P.; Fuller, A.; Skowera, A.; Rossjohn, J.; Zhu, C.; Miles, J. J.; Peakman, M.; Wooldridge, L.; Rizkallah, P. J.; Sewell, A. K. Hotspot Autoimmune T Cell Receptor Binding Underlies Pathogen and Insulin Peptide Cross-Reactivity. *J. Clin. Investig.* **2016**, *126*, 2191-204.
157. Wang, E.; Babbey, C. M.; Dunn, K. W. Performance Comparison between the High-Speed Yokogawa Spinning Disc Confocal System and Single-Point Scanning Confocal Systems. *J. Microsc.* **2005**, *218*, 148-159.
158. Thompson, N. L.; Steele, B. L. Total Internal Reflection with Fluorescence Correlation Spectroscopy. *Nat Protoc* **2007**, *2*, 878-90.

159. Thompson, N. L.; Wang, X.; Navaratnarajah, P. Total Internal Reflection with Fluorescence Correlation Spectroscopy: Applications to Substrate-Supported Planar Membranes. *J Struct Biol* **2009**, *168*, 95-106.
160. Axelrod, D. Chapter 7: Total Internal Reflection Fluorescence Microscopy. *Methods Cell Biol.* **2008**, *89*, 169-221.
161. Wohland, T. Imfcs Imagej Plugin. [http://www.dbs.nus.edu.sg/lab/BFL/imfcs\\_image\\_j\\_plugin.html](http://www.dbs.nus.edu.sg/lab/BFL/imfcs_image_j_plugin.html) (accessed Oct, 4 2015).
162. Bag, N.; Sankaran, J.; Paul, A.; Kraut, R. S.; Wohland, T. Calibration and Limits of Camera-Based Fluorescence Correlation Spectroscopy: A Supported Lipid Bilayer Study. *ChemPhysChem* **2012**, *13*, 2784-94.
163. Ries, J.; Chiantia, S.; Schwille, P. Accurate Determination of Membrane Dynamics with Line-Scan Fcs. *Biophys J* **2009**, *96*, 1999-2008.
164. Stasevich, T. J.; Mueller, F.; Michelman-Ribeiro, A.; Rosales, T.; Knutson, J. R.; McNally, J. G. Cross-Validating Frap and Fcs to Quantify the Impact of Photobleaching on in Vivo Binding Estimates. *Biophys J* **2010**, *99*, 3093-101.
165. Knight, A. W.; Billington, N. Distinguishing Gfp from Cellular Autofluorescence. *Biophotonics Int.* **2001**, *8*, 42-50.
166. Neumann, M.; Gabel, D. Simple Method for Reduction of Autofluorescence in Fluorescence Microscopy. *J. Histochem. Cytochem.* **2002**, *50*, 437-439.
167. Mansfield, J. R.; Gossage, K. W.; Hoyt, C. C.; Levenson, R. M. Autofluorescence Removal, Multiplexing, and Automated Analysis Methods for in-Vivo Fluorescence Imaging. *J. Biomed. Opt.* **2005**, *10*, 41207.
168. Zhu, L.; Zhu, M. Q.; Hurst, J. K.; Li, A. D. Q. Light-Controlled Molecular Switches Modulate Nanocrystal Fluorescence. *J. Am. Chem. Soc.* **2005**, *127*, 8968–8970.
169. Zhu, L.; Wu, W.; Zhu, M. Q.; Han, J. J.; Hurst, J. K.; Li, A. D. Q. Reversibly Photoswitchable Dual-Color Fluorescent Nanoparticles as New Tools for Live-Cell Imaging. *J. Am. Chem. Soc.* **2007**, *129*, 3524–3526.
170. Tian, Z.; Wu, W.; Wan, W.; Li, A. D. Q. Single-Chromophore-Based Photoswitchable Nanoparticles Enable Dual-Alternating-Color Fluorescence for Unambiguous Live Cell Imaging. *J. Am. Chem. Soc.* **2009**, *131*, 4245–4252.
171. Zhu, M. Q.; Zhang, G. F.; Li, C.; Aldred, M. P.; Chang, E.; Drezek, R. A.; Li, A. D. Q. Reversible Two-Photon Photoswitching and Two-Photon Imaging of Immunofunctionalized Nanoparticles Targeted to Cancer Cells. *J. Am. Chem. Soc.* **2011**, *133*, 365–372.

172. Wan, W.; Zhu, M. Q.; Tian, Z.; Li, A. D. Q. Antiphase Dual-Color Correlation in a Reactant-Product Pair Imparts Ultrasensitivity in Reaction-Linked Double-Photoswitching Fluorescence Imaging. *J. Am. Chem. Soc.* **2015**, *137*, 4312-4315.
173. Hsiang, J. C.; Jablonski, A. E.; Dickson, R. M. Optically Modulated Fluorescence Bioimaging: Visualizing Obscured Fluorophores in High Background. *Acc. Chem. Res.* **2014**, *47*, 1545-1554.
174. Habuchi, S.; Ando, R.; Dedecker, P.; Verheijen, W.; Mizuno, H.; Miyawaki, A.; Hofkens, J. Reversible Single-Molecule Photoswitching in the Gfp-Like Fluorescent Protein Dronpa. *Proc. Natl. Acad. Sci. U.S.A.* **2005**, *102*, 9511-9516.
175. Andresen, M.; Stiel, A. C.; Folling, J.; Wenzel, D.; Schonle, A.; Egner, A.; Eggeling, C.; Hell, S. W.; Jakobs, S. Photoswitchable Fluorescent Proteins Enable Monochromatic Multilabel Imaging and Dual Color Fluorescence Nanoscopy. *Nat. Biotechnol.* **2008**, *26*, 1035-1040.
176. Berezin, M. Y.; Achilefu, S. Fluorescence Lifetime Measurements and Biological Imaging. *Chem. Rev.* **2010**, *110*, 2641-2684.
177. Our History: Leica Microsystems. <https://www.leica-microsystems.com/company/our-history/> (accessed November 12, 2017).
178. Padilla-Parra, S.; Marin, M.; Kondo, N.; Melikyan, G. B. Synchronized Retrovirus Fusion in Cells Expressing Alternative Receptor Isoforms Releases the Viral Core into Distinct Sub-Cellular Compartments. *PLoS Pathog* **2012**, *8*, e1002694.
179. Wilen, C. B.; Tilton, J. C.; Doms, R. W. Hiv: Cell Binding and Entry. *Cold Spring Harb Perspect Med* **2012**, *2*, 1-13.
180. Gatzogiannis, E.; Zhu, X.; Kao, Y.-T.; Min, W. Observation of Frequency-Domain Fluorescence Anomalous Phase Advance Due to Dark-State Hysteresis. *J. Phys. Chem. Lett.* **2011**, *2*, 461-466.
181. Yonemaru, Y.; Yamanaka, M.; Smith, N. I.; Kawata, S.; Fujita, K. Saturated Excitation Microscopy with Optimized Excitation Modulation. *ChemPhysChem* **2014**, *15*, 743-749.
182. Manna, P.; Jimenez, R. Time and Frequency-Domain Measurement of Ground-State Recovery Times in Red Fluorescent Proteins. *J. Phys. Chem. B* **2015**, *119*, 4944-4954.
183. Kao, Y. T.; Zhu, X.; Min, W. Protein-Flexibility Mediated Coupling between Photoswitching Kinetics and Surrounding Viscosity of a Photochromic Fluorescent Protein. *Proc. Natl. Acad. Sci. U.S.A.* **2012**, *109*, 3220-3225.

184. Ursell, T.; Huang, K. C. Blurlab -- 3d Microscopy Simulation Package V0.9. <https://simtk.org/projects/blurlab> (accessed May 1, 2015).
185. Chen, W.; Zarnitsyna, V. I.; Sarangapani, K. K.; Huang, J.; Zhu, C. Measuring Receptor-Ligand Binding Kinetics on Cell Surfaces: From Adhesion Frequency to Thermal Fluctuation Methods. *Cell Mol Bioeng* **2008**, *1*, 276-288.
186. Machan, R.; Foo, Y. H.; Wohland, T. On the Equivalence of Fcs and Frap: Simultaneous Lipid Membrane Measurements. *Biophys. J.* **2016**, *111*, 152-161.
187. Huppa, J. B.; Axmann, M.; Mortelmaier, M. A.; Lillemeier, B. F.; Newell, E. W.; Brameshuber, M.; Klein, L. O.; Schutz, G. J.; Davis, M. M. Tcr-Peptide-Mhc Interactions in Situ Show Accelerated Kinetics and Increased Affinity. *Nature* **2010**, *463*, 963-7.